

PFC/RR-83-13

DOE/ET-51013-83
UC-20

RAY TRACING ANALYSIS OF ELECTRON CYCLOTRON RESONANCE
HEATING IN STRAIGHT STELLARATORS

Kosuke Kato

Plasma Fusion Center
Massachusetts Institute of Technology
Cambridge, MA 02139

May 1983

This work was supported by the U.S. Department of Energy Contract No. DE-AC02-78ET51013. Reproduction, translation, publication, use and disposal, in whole or in part by or for the United States government is permitted.

RAY TRACING ANALYSIS OF ELECTRON CYCLOTRON
RESONANCE HEATING IN STRAIGHT STELLARATORS

by

Kosuke Kato

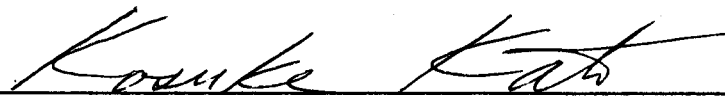
Submitted to the Department of
Nuclear Engineering in Partial
Fulfillment of the Requirements
for the Degrees of

MASTER OF SCIENCE
and
BACHELOR OF SCIENCE IN NUCLEAR ENGINEERING
at the
MASSACHUSETTS INSTITUTE OF TECHNOLOGY

June 1983

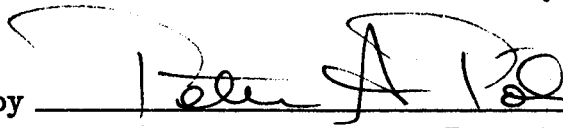
© Massachusetts Institute of Technology 1983

Signature of Author



Department of Nuclear Engineering
May 3, 1983

Certified by



Peter A. Politzer, Thesis Supervisor

Accepted by

Alan F. Henry, Chairman,
Nuclear Engineering Departmental Committee

RAY TRACING ANALYSIS OF ELECTRON CYCLOTRON RESONANCE HEATING IN STRAIGHT STELLARATORS

by

Kosuke Kato

Submitted to the Department of Nuclear Engineering
on May 6, 1983 in partial fulfillment of the
requirements for the Degrees of Master of Science and
Bachelor of Science in Nuclear Engineering

Abstract

A ray-tracing computer code is developed and implemented to simulate electron cyclotron resonance heating (ECRH) in stellarators. A straight stellarator model is developed to simulate the confinement geometry. Following a review of ECRH, a cold plasma model is used to define the dispersion relation. To calculate the wave power deposition, a finite temperature damping approximation is used. 3-D ray equations in cylindrical coordinates are derived and put into suitable forms for computation. The three computer codes, MAC, HERA, and GROUT, developed for this research, are described next. ECRH simulation is then carried out for three models including Heliotron E and Wendelstein VII A. Investigated aspects include launching position and mode scan, frequency detuning, helical effects, start-up, and toroidal effects. Results indicate: (1) an elliptical waveguide radiation pattern, with its long axis oriented half-way between the toroidal axis and the saddle point line, is more efficient than a circular one; and (2) mid-plane, high field side launch is favored for both O- and X-waves.

Thesis Supervisor: Dr. Peter A. Politzer
Title: Principal Research Scientist, Plasma Fusion Center.

Thesis Reader: Dr. Lawrence M. Lidsky
Title: Professor of Nuclear Engineering.

Acknowledgments

I would like to express my deep appreciation to my supervisor, Dr. Peter Politzer, who suggested this thesis topic, and who led me on the whole way. I also thank Prof. Lawrence Lidsky, my reader, for guidance and helpful discussions. Dr. Donald Blackfield was instrumental in starting me off on the right track with respect to ray-tracing and other numerical aspects of the research. The extensive use of the MIT and MFECC computer facilities would not have been possible if not for the patient guidance of Mr. Jean-Marie Noterdaeme. I would also like to thank Prof. James Paradis of the Writing Program for many helpful suggestions on improving the text. Finally, I would like to acknowledge and thank the support and encouragement of my parents. My salary and the project were funded by DOE Contract No. DE-ACO2-78ET-51013.

Table of Contents

Title	1
Abstract	2
Acknowledgments	3
Table of Contents	4
List of Tables	7
List of Figures	8
Nomenclature	11
1. Introduction	13
1.1 Background	13
1.2 Project Description	14
2. Straight Stellarator Modeling	17
2.1 Introduction	17
2.2 Stellarator Magnetic Field	18
2.3 Stellarator Flux Function	21
2.4 Stellarator Rotational Transform	22
2.5 Plasma Modeling	24
2.6 Validity of the Model	25
2.7 Summary	26
3. ECRF Propagation	27
3.1 Introduction	27
3.2 ECRF Propagation in a Cold Plasma	28
3.2.1 Appleton-Hartree Dispersion Relation	28
3.2.2 Classifications of Waves in the ECRF	31
3.3 ECRF Absorption in a Finite Temperature Plasma	35
3.3.1 Finite Temperature Effects	35

3.3.2 Wave Damping Formulae	37
3.4 Summary	39
4. Ray Tracing	41
4.1 Introduction	41
4.2 Derivation of the Ray Equations	43
4.3 Limitations	47
4.4 Summary	48
5. Helical Plasma Ray Tracing Code(HERA)	50
5.1 Introduction	50
5.2 Code Development	51
5.3 Structure of MAC, HERA, and GROUT	52
5.3.1 MAC	52
5.3.2 HERA	53
5.3.3 GROUT	56
5.4 Summary	57
6. Simulation Models of Stellarators	58
6.1 Introduction	58
6.2 Modeling Criteria	58
6.3 Heliotron E	60
6.4 Wendelstein VII A	62
6.5 $l = 3$ Stellarator	65
6.6 Summary	68
7. Simulation Results and Conclusions	70
7.1 Introduction	70
7.2 General Results	71
7.2.1 Simulation Figures	71
7.2.2 Launching Position and Mode Scan in Heliotron E	73
7.2.3 Frequency Detuning in Heliotron E	82

7.2.4 Helical Effects	83
7.2.5 Start-Up	86
7.2.6 Wendelstein VII A	88
7.2.7 $l = 3$ Stellarator	96
7.3 Effects of Toroidicity	96
7.4 Comparison with Experimental ECRH in Stellarators	103
7.5 Comparison with Tokamak and Mirror ECRH	104
7.6 Guidelines Defined for ECRH in Stellarators	106
7.7 Summary	110
8. Summary and Conclusions	114
8.1 Summary and Conclusions	114
8.2 Recommendations for Future Investigation	118
Appendix A. Derivatives of the Dispersion Relation	119
References	124

List of Tables

No.	Page	Title
6.1	61	Heliotron E Parameters
6.2	61	Heliotron E Model Parameters
6.3	66	Wendelstein VII A Parameters
6.4	66	Wendelstein VII A Model Parameters
6.5	68	$l = 3$ Stellarator Model Parameters
7.1	73	Four Combinations of Modes and Injection Points
7.2	101	Comparison of Helical and Toroidal Effects

List of Figures

No.	Page	Title
2.1	19	Three Types of Stellarator Windings
2.2	21	Helical Coordinates Shown on a Cylindrical Surface
2.3	23	Flux Surfaces and Magnetic Field Contours of an $l = 2$ Stellarator
2.4	23	Flux Surfaces and Magnetic Field Contours of an $l = 3$ Stellarator
3.1	29	Appleton-Hartree Dispersion Relation Geometry
3.2	32	Fields of the O-mode, X-mode, RHCP, and LHCP Waves
3.3	34	CMA Diagram
3.4	35	Accessibility on CMA Diagram
5.1	55	Launching Options for HERA
6.1	62	Heliotron E Rotational Transform
6.2	63	Heliotron E Model Poloidal Cross-Section
6.3	63	Heliotron E ECRH Launching Geometry
6.4	67	Wendelstein VII A Rotational Transform
6.5	67	Wendelstein VII A Model Poloidal Cross-Section
6.6	69	$l = 3$ Stellarator Model Rotational Transform
6.7	69	$l = 3$ Stellarator Model Poloidal Cross-Section
7.1	72	Simulation Geometry
7.2	74	Trajectories of O-Waves Launched from the Low Field Side in Heliotron E ($\rho = 5^\circ$, $r = 0.50m$)
7.3	75	Trajectories of O-Waves Launched from the Low Field Side in Heliotron E ($\rho = 10^\circ$, $r = 0.50m$)
7.4	76	Trajectories of X-Waves Launched from the Low Field Side in Heliotron E
7.5	77	Trajectories of O-Waves Launched from the High

		Field Side in Heliotron E($\rho = 5^\circ, r = 0.50m$)
7.6	78	Trajectories of X-Waves Launched from the High Field Side in Heliotron E($\rho = 5^\circ, r = 0.50m$)
7.7	80	O-Wave Power Absorption Contour in Heliotron E
7.8	82	Three Types of Two Pass Rays in Heliotron E
7.9	84	Shift of Resonance Layers with Shift in Frequency in Heliotron E
7.10	85	Power Absorption Profiles as a Function of Frequency in Heliotron E($\rho = 5^\circ, r = 0.50m$)
7.11	87	Effects of Helical Geometry on the Ray Trajectory in Heliotron E($\rho = 10^\circ, r = 0.50m$)
7.12	89	Evolution of Resonance Layers with Plasma Formation in Heliotron E
7.13	91	Trajectories of O-Waves Launched from the Low Field Side in Wendelstein VII A($\rho = 5^\circ, r = 0.20m$)
7.14	92	Trajectories of O-Waves Launched from the High Field Side in Wendelstein VII A($\rho = 10^\circ, r = 0.35m$)
7.15	93	Trajectories of X-Waves Launched from the High Field Side in Wendelstein VII A($\rho = 10^\circ, r = 0.35m$)
7.16	94	Comparison of Heliotron E and Wendelstein VII A Damping Terms
7.17	95	Comparison of Heliotron E and Wendelstein VII A Magnetic Fields
7.18	97	Trajectories of O-Waves Launched from the Low Field Side in $l = 3$ Stellarator($\rho = 5^\circ, r = 0.25m$)
7.19	98	Trajectories of O-Waves Launched from the High Field Side in $l = 3$ Stellarator($\rho = 5^\circ, r = 0.25m$)
7.20	99	Trajectories of X-Waves Launched from the High Field Side in $l = 3$ Stellarator($\rho = 15^\circ, r = 0.25m$)
7.21	102	Quasi-Toroidal Effects
7.22	105	ECRF Resonance Layers in Tokamaks and Mirrors
7.23	107	Plots of k vs. Time for O-Waves in Heliotron E

7.24	111	Recommended Waveguide Radiation Pattern
7.25	111	Recommended Launching Position

Nomenclature

Symbol	Dimension	Definition
\bar{a}	m	Average Minor Radius
A	$Tesla \cdot m$	Magnetic Vector Potential
B_o	$Tesla$	Toroidal Magnetic Field
B_h	$Tesla$	Helical Magnetic Field
E	V/m	Electric Field
F	-	Dispersion Relation
k	m^{-1}	Wave Number
k_{\parallel}	m^{-1}	Parallel Wave Number
k_{\perp}	m^{-1}	Perpendicular Wave Number
l	-	l Number
L_B	m	Magnetic Field Gradient Scale Length
m	-	Poloidal Rotation Number
m_n	-	Density Profile Factor
m_T	-	Temperature Profile Factor
n_e	m^{-3}	Electron Density
N	-	Index of Refraction
N_{\parallel}	-	Parallel Index of Refraction
N_{\perp}	-	Perpendicular Index of Refraction
r	m	Radial Coordinate
R	m	Major Radius
t	sec	Time
T	-	Transmission Coefficient
T_e	eV	Electron Temperature
v_e	m/sec	Electron Thermal Velocity
z	m	Axial Coordinate
α	m^{-1}	Inverse Winding Pitch

β	<i>rad</i>	Helical Angle
γ	<i>rad</i>	Azimuthal Angle of Launching Cone
θ	<i>rad</i>	Azimuthal Coordinate
t	-	Rotational Transform
ρ	<i>rad</i>	Launch Cone Half Angle
ϕ	<i>rad</i>	Equivalent Azimuthal Angle in Helical Coordinates
ϕ_B	<i>Tesla · m</i>	Magnetic Scalar Potential
Ψ	-	Flux Function
ω	<i>rad/sec</i>	Wave Frequency
ω_{pe}	<i>rad/sec</i>	Plasma Frequency
ω_{ce}	<i>rad/sec</i>	Electron Cyclotron Frequency

Chapter 1

Introduction

1.1 Background

Four large tokamaks, TFTR, JT-60, JET, and T-20, will come on line in the next few years, claiming to achieve breakeven and to prove the scientific feasibility of fusion power generation. The fusion community must start thinking about the options for reactor designs. At present, tokamaks are best understood, with tandem mirrors, stellarators, and EBT following as back up devices. However, it is still uncertain whether or not tokamaks will make the commercially most attractive reactors. Some of the problems encountered are: small aspect-ratio and bad accessibility to the inside of the torus; inherently pulsed operation; or, in the event of a current drive utilization, continuous power feedback for steady-state operation.

Stellarators, on the other hand, are inherently steady-state devices with field configurations possessing built-in divertors. The only power requirement after ignition for stellarators is the power to run currents through the magnets, which is negligible compared to the power output if superconducting magnets are used. The disadvantages of stellarators as reactor devices are the complexity of construction due to the helical windings, and inherently large power output

because of the large aspect-ratio.

The stellarator concept is one of the oldest in the history of fusion research. The first fusion reactor design was a figure-eight stellarator done at Princeton[1]. The Princeton Model C stellarator(1957-1969) was the major toroidal experiment in the U.S. until tokamaks took over as mainline devices in the late 1960's[2]. Interests in stellarators waxed and waned in the fusion community over the last decade and a half, but recent experimental developments on the Heliotron E and Wendelstein VII A have proven these stellarators to be just as good as medium sized tokamaks with respect to plasma confinement. In short, stellarators are attractive alternatives to tokamaks. Recent approval of the ATF Project[3] will also complement worldwide stellarator research effort.

1.2 Project Description

Once the physics of toroidal plasmas is understood and the plasma is controlled, design decisions will have to be made on the selection of the reactor scheme that is attractive to the electric power industry and society. Much data on each prospective reactor device will be required at that time.

This thesis attempts to supply some such information. It will focus on the radio frequency heating of an idealized stellarator plasma. Stellarators are current-free, steady-state devices, and as such, will require some bulk heating scheme. Currently, two schemes, beam injection and radio frequency injection, are available and both are equally attractive. However, experience with radio frequency heating has produced an abundance of data and theory that suggests it is the better choice for investigation at this time. The short duration of this thesis research limits the scope of the current work to investigating the frequency regime in which electron cyclotron resonance heating(ECRH) takes place.

ECRH frequency regime was chosen over ion cyclotron resonance heating(ICRH) or lower hybrid heating(LHH) regimes for the following reasons.

- (1) It is the simplest place to start. Ions can be neglected and calculations simplified a great deal compared to a full, multi-component plasma treatment.
- (2) Cyclotron layer power absorption mechanism is well understood and the heat deposition is localized, making it suitable for controlling the plasma temperature profile as well as for heating.
- (3) The short wavelength of the frequency regime makes it ideal for the WKB treatment, which is the method employed in this thesis.
- (4) An extensive body of theoretical and experimental work on ECRH of tokamaks and mirrors exists, while works on tokamak ICRH and LHH are not as exhaustive.
- (5) A comparison of simulation with existing and proposed ECRH experiments on stellarators is possible.

The major problem of ECRH at the present time is the unavailability of high-power, high-frequency gyrotrons. At present, 28 GHz gyrotrons are available, but this corresponds to a magnetic field strength of 1 Tesla for fundamental heating, and to even lower values if harmonic heating is considered. At this time, 60 GHz gyrotrons are available in limited quantities on some experiments (Doublet III and Heliotron E). It is hoped that these, as well as higher frequency gyrotrons will be available at prices competitive with other lower frequency sources by the time a reactor design is considered.

In this thesis, a 2-D straight stellarator model is defined, then a 3-D ray tracing computer code is developed for the model. The code is implemented, simulating several existing and fictitious experiments, and results are analyzed. Particular problems to be addressed include:

- (1) investigation of the dependence of power absorption and heating efficiency on the launching position and direction;
- (2) investigation of the effect of helical geometry on wave propagation and absorption;
- (3) comparison of simulation results with ECRH experiments on stellarators;
- (4) comparison of stellarator ECRH with tokamak or mirror ECRH results;
- (5) formulation of a consistent set of guidelines for ECRH in stellarators.

In Chapter 2, the straight stellarator model to be used throughout the thesis is described. Analytical expressions for the magnetic field and the plasma parameters are presented, and the flux function and rotational transform are discussed. The validity and usefulness of the model are also discussed.

Chapter 3 deals with the wave propagation theory in the plasma for electron cyclotron range of frequencies(ECRF). First, an instructive view is given by examining the cold plasma model. Wave physics terminologies are defined and qualitative pictures of the wave propagation are given. Next, wave propagation and absorption in a finite temperature plasma is discussed. Dispersion relation and damping formulae to be used in the code are presented.

In Chapter 4, the physics of ray tracing analysis is discussed and the six ray equations to be used in the code are derived. Limitations of the WKB theory are also discussed.

Having defined the underlying physics, Chapter 5 provides a detailed description of the HERA(HElical plasma RAY tracing code) code family developed for this thesis. Information on how to actually implement the code is given. Listings of the codes may be obtained from the author. This chapter may be skipped without loss of continuity.

In Chapter 6, the three stellarator models are defined. After discussing the modeling criteria, specifications of the models, obtained using MAC(MACHINE parameter code), are presented.

In Chapter 7, results of implementing HERA on the models defined in Chapter 6 are presented. Discussion on the comparison of data with experiment is given. Conclusions drawn from these results are presented, along with a set of suggested guidelines for ECRH experiments in stellarators.

Chapter 8 summarizes the entire project, and suggests future work in this field.

Chapter 2

Straight Stellarator Modeling

2.1 Introduction

In this chapter, the magnetic fields, flux function, rotational transform, and plasma density and temperature profiles for the straight stellarator model are presented. Limitations and applicability of the model are also discussed, with particular emphasis on the absence of toroidal effects.

The term "stellarator" is now a generic one that applies to any toroidal plasma confinement device whose confining magnetic fields are produced entirely by the external coil systems, i.e., there is no current flowing through the plasma. Stellarator devices are characterized by the l number, where l corresponds to the number of singular points of the magnetic field on a given poloidal cross section. The classical stellarator, such as the Princeton Model C or the Wendelstein VII A, has $2l$ helical windings, with currents flowing in alternate directions, in addition to the toroidal windings as in tokamaks (Figure 2.1a). A heliotron device, such as the Heliotron E, has toroidal field coils and l helical windings, with all the helical currents flowing in the same direction (Figure 2.1b). A torsatron is a device with only the helical windings, also with all the currents flowing in the same direction (Figure 2.1c). For heliotrons and

torsatrons, vertical field coils are needed to compensate for the net vertical field produced by the helical windings due to unidirectional currents and toroidicity. There are also designs of stellarators with modular windings, which relax some engineering constraints[4].

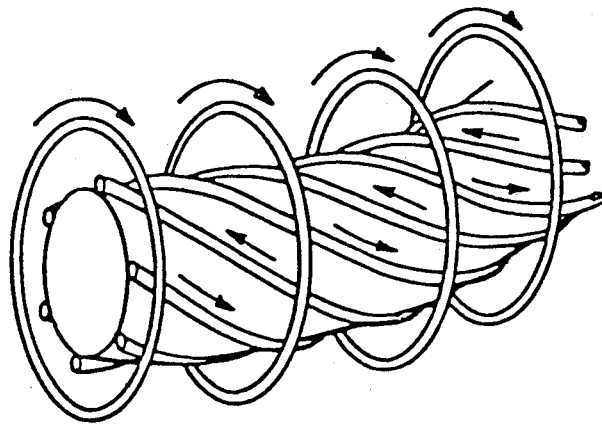
A toroidal stellarator is a fully three-dimensional system in that there exists no axis of symmetry of the magnetic field or the coil windings. In order to obtain an accurate description of the fields, currents flowing through the entire coil system must be evaluated using the Biot-Savart's law, which is a time consuming calculation. The recent advent of high-speed super computers, such as the CRAY-1 and CDC-7600, have made possible the accurate modeling of a toroidal stellarator magnetic field and the plasma parameters by using a spline or a finite element method[5]. Although such methods are employed in some aspects of stellarator research, a less strenuous approach is to consider the limit of an infinite aspect-ratio device, i.e., a straight stellarator. Such an approach is considered to be valid for large aspect-ratio devices like Heliotron E and Wendelstein VII A, which have aspect-ratios of 11 and 20, respectively.

The expressions for the magnetic fields in a straight stellarator reduce to simple analytical forms, thereby greatly reducing the computational burden. Furthermore, all the relevant properties of stellarator fields, such as the existence of a separatrix and the outwardly increasing rotational transform profile, are retained.

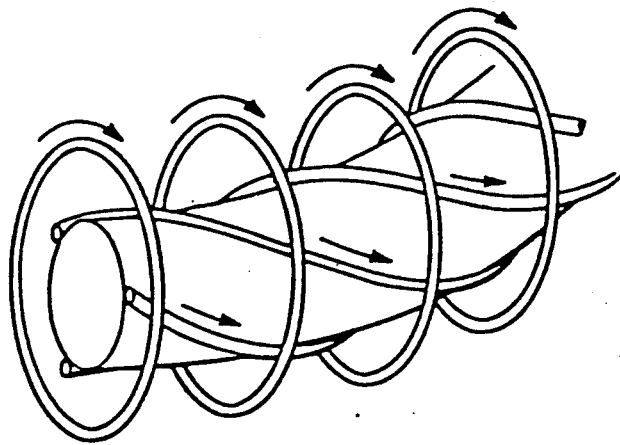
2.2 Stellarator Magnetic Field

Assume straight classical stellarator windings as shown in Figure 2.1a, with the number of helical windings equal to $2l$. Further assume the windings to be thin filaments. Then the magnetic field scalar potential inside the windings is given by[6],

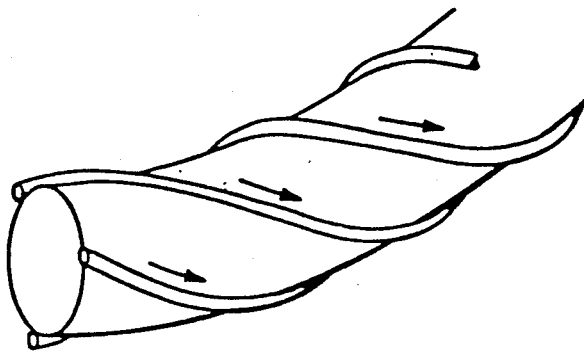
$$\phi_B = B_0 z + \frac{i}{\alpha} \sum_l B_{hl} I'_l(l\alpha r) \sin(l\phi). \quad (2.1)$$



a. Stellarator ($l = 3$)



b. Heliotron ($l = 3$)



c. Torsatron ($l = 3$)

Figure 2.1 Three Types of Stellarator Windings[4]

Here, B_o and B_h are the magnitudes of the toroidal and helical magnetic fields, respectively, and α is the inverse winding pitch given by $\alpha = \frac{2\pi}{p}$, where p is the winding pitch. The equation is expressed in cylindrical coordinates, r , θ , and z . The equivalent azimuthal angle of the helical coordinate system, ϕ , is given by $\phi = \theta - \alpha z$. Differentiation of the l -th order modified Bessel function of the first kind with respect to the argument, $l\alpha r$, is denoted by I'_l . The summation is taken over l and its integral multiples in order that the effect of a finite cross section coil may be taken into account.

The components of the magnetic field are given by $\nabla\phi_B = \underline{B}$:

$$B_r = \sum_l l B_{hl} I'_l(l\alpha r) \sin(l\phi); \quad (2.2)$$

$$B_\theta = \sum_l \left(\frac{1}{\alpha r}\right) l B_{hl} I'_l(l\alpha r) \cos(l\phi); \quad (2.3)$$

$$B_z = B_o - \sum_l l B_{hl} I'_l(l\alpha r) \cos(l\phi). \quad (2.4)$$

Quantities such as $\nabla\underline{B}$, $|\underline{B}|$ etc., are obtained by further differentiation or algebra.

In addition to the components of the magnetic field in r , θ , and z directions, it is also useful to derive the expression for the component of the magnetic field in ϕ direction. Consider Figure 2.2, which is a view of an unrolled cylindrical surface. The solid diagonal line is the helical coordinate axis, with helical angle β . The equivalent azimuthal angle is denoted by ϕ [7]. Then the component of the magnetic field in ϕ direction is given by

$$B_\phi = B_\theta \cos \beta - B_z \sin \beta \quad (2.5)$$

from simple trigonometry. Defining a quantity $q \equiv (1 + \alpha^2 r^2)^{\frac{1}{2}}$, Equation (2.5) can be rewritten as

$$B_\phi = \frac{1}{q} B_\theta - \frac{\alpha r}{q} B_z. \quad (2.6)$$

Changing the ratio of $\frac{B_h}{B_o}$ allows this coil configuration to model heliotrons and torsatrons as well.

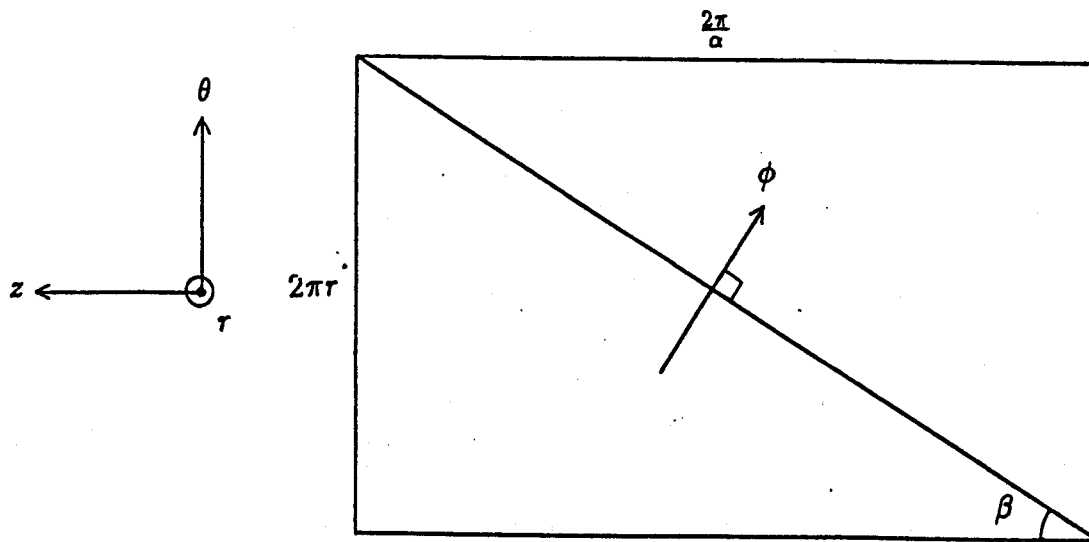


Figure 2.2 Helical Coordinates Shown on a Cylindrical Surface

2.3 Stellarator Flux Function

Flux surfaces are surfaces on which the magnetic field lines lie. Furthermore, these surfaces coincide with constant pressure surfaces for MHD equilibrium. Therefore, it is useful to define a function that parameterizes the flux surfaces for calculation of density and temperature profiles.

The components of the magnetic vector potential \underline{A} , defined by

$$\nabla \times \underline{A} = \underline{B} \quad (2.7)$$

are given by[6]:

$$A_r = -\frac{1}{\alpha^2 r} \sum_l B_{hl} I_l(l\alpha r) \sin(l\phi); \quad (2.8)$$

$$A_\theta = \frac{B_o}{2} r - \frac{1}{\alpha} \sum_l B_{hl} I'_l(l\alpha r) \cos(l\phi); \quad (2.9)$$

$$A_z = 0. \quad (2.10)$$

The straight stellarator flux function, Ψ defined as $\Psi = A_z + \alpha r A_\theta$ is therefore,

$$\Psi(r, \phi) = B_o \frac{\alpha r^2}{2} - r \sum_l B_{hl} I'_l(l\alpha r) \cos(l\phi). \quad (2.11)$$

Different values of Ψ correspond to different flux surfaces. As it is defined, $\Psi(0, \phi) = 0$ and increases with r for positive values of B_o and B_h .

Note that the separatrix, which is the last closed surface, is defined by the saddle points where $\frac{\partial \Psi}{\partial r} = 0$ and $\frac{\partial \Psi}{\partial \theta} = 0$ are satisfied simultaneously. The flux function at the saddle point has a local maximum if its value is plotted against r , and has a local minimum if its value is plotted against θ . Consequently, on the separatrix surface, $\frac{\partial \Psi}{\partial r}$ is small at the saddle point but it is large at points other than the saddle point.

Typical $l = 2$ and $l = 3$ flux surfaces generated by MAC(MACHine parameters code - to be described in Chapter 5) are shown in Figures 2.3 and 2.4. These figures also show constant magnetic field contours(dotted lines). Arrows indicate the directions of $\nabla |B|$. These contours are similar to multipole fields, where the number of poles equals l .

2.4 Stellarator Rotational Transform

Rotational transform ι of a magnetic field system is a measure of the twist of the field lines of the system. It is defined as,

$$\iota \equiv \frac{\text{rotation of the field line in poloidal direction}}{\text{rotation of the field line in toroidal direction}}. \quad (2.12)$$

It is a function defined on a flux surface. The more commonly used quantity is $\iota \equiv \frac{\iota}{2\pi}$. This quantity is related to q , the tokamak safety factor, by $q = \frac{1}{\iota}$.

In an infinite, straight system, ι must be defined suitably. Namely, ι per field period will be used to characterize the system. Then,

$$\iota_{f.p.} = \int_0^{2\pi} \frac{1}{l} \left(1 + \frac{\phi}{\alpha z(\phi)} \right) d\phi, \quad (2.13)$$

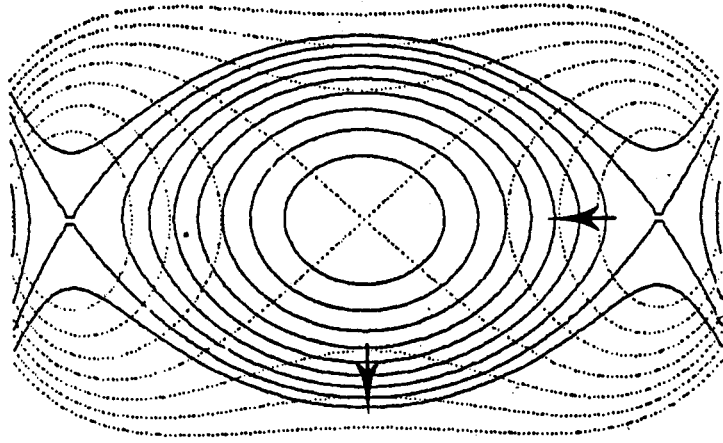


Figure 2.3 Flux Surfaces and Magnetic Field Contours of an $l = 2$ Stellarator

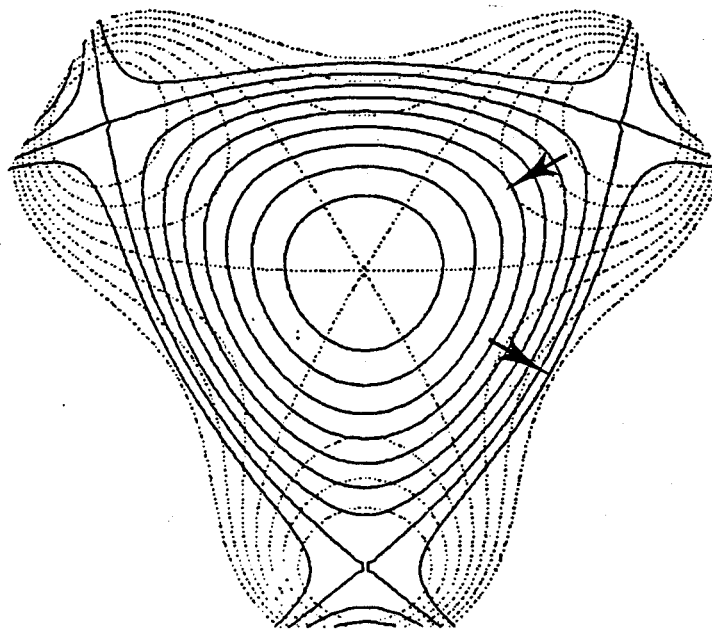


Figure 2.4 Flux Surfaces and Magnetic Field Contours of an $l = 3$ Stellarator

where all the quantities are defined previously. Here the integration path in fixed coordinates must be taken along a particular field line. Differential equations for the change in the position of a field line can be written as:

$$\frac{dr}{d\phi} = \frac{B_r r}{q B_\phi}; \quad (2.14)$$

$$\frac{dz}{d\phi} = \frac{B_z r}{q B_\phi}; \quad (2.15)$$

where, again, all the quantities on the right-hand sides are given in Section 2.2. Integrating these two differential equations will give r at each ϕ and a final z corresponding to $\phi = 2\pi$, or one poloidal rotation around the flux surface. This will allow both the evaluation of Equation (2.13) and the average radius. Evaluation of the average radius is preferred since, although ϵ is a function of the flux function, it is customary to consider it as a function of the average radius of the flux surface, i.e., $\epsilon_{f.p} = \epsilon_{f.p}(\bar{r})$.

In general, the rotational transform for a stellarator geometry is small at the center and increases with radius, which is opposite to tokamaks. An $l = 2$ stellarator will have a finite transform on axis, but will have a small shear (small variation of ϵ). On the other hand, an $l = 3$ stellarator will have a zero transform on axis with a large shear [8].

2.5 Plasma Modeling

The generation of plasma density and temperature profiles is greatly simplified if the following forms are assumed for the profiles:

$$n_i(r, \phi) = n_{i0} \left(1 - \frac{\Psi}{\Psi_s}\right)^{m_n}; \quad (2.16)$$

and

$$T_i(r, \phi) = T_{i0} \left(1 - \frac{\Psi}{\Psi_s}\right)^{m_T}; \quad (2.17)$$

where $n_i(r, \phi)$ and $T_i(r, \phi)$ are the density and temperature profiles of the i -th plasma species, respectively. Ψ is the flux function and Ψ_s is the flux function

evaluated at the separatrix. Exponents m_n and m_T are the powers to which the respective profiles are raised. The peak density and temperature for the i -th plasma species are denoted by n_{i0} and T_{i0} , respectively. These profiles then imply that the pressure, $P = n\kappa T$, is also a function of the flux function, which is qualitatively consistent with the MHD equilibrium condition, $\nabla p \times \underline{B} = 0$.

This model assumes that the density will go to zero at the edge, and the edge will be on the last closed flux surface. It ignores the existence of scrape-off layers and diverted particles that may play a role in refracting injected waves.

2.6 Validity of the Model

The straight stellarator model is essentially the limit of an infinite aspect-ratio, and toroidicity does not enter into consideration. The effects of toroidicity are three-fold:

- (1) the toroidal component of the magnetic field will fall off as $\frac{1}{R}$, where R is the major radius of the plasma;
- (2) the separatrix, discussed in Section 2.3, is no longer a surface, but occupies a finite region of space;
- (3) the poloidal cross-section of the plasma loses symmetry due to the toroidal field changing across the cross-section.

No effort was made to compare this model with a toroidal stellarator model due to the unavailability of the latter. However, the effects of toroidicity on wave propagation and absorption is discussed in Chapter 7, by considering a quasi-toroidal model. It is shown that for Heliotron E, the toroidal effect is small compared to the helical effect, and that the general feature of the flux surface does not change very much.

There are problems in applying the straight model to helical axis stellarators or modular stellarators. In helical axis stellarators, the axis will undergo a helical rotation in a distance on the order of a field period, invalidating the approximation of a straight axis. In modular stellarators, the helical symmetry

is absent, which precludes the use of the straight model[9]. The model is applicable to stellarators currently in operation, including the proposed ATF, since they are all of the classical type.

In conclusion, the straight stellarator model should be accurate for large aspect-ratio and short pitched devices, where one field period can be closely approximated by a cylinder; assuming that the device is a variation of the classical stellarator and not of the modular type. The model is also fully satisfactory for investigation of helical field effects on wave propagation.

2.7 Summary

In this chapter, the mathematical model of a straight stellarator was defined in detail. Starting from an analytical model for the magnetic fields inside a stellarator winding, the field components, vector potential, and flux function were derived. For the field components, the component perpendicular to the helical axis was derived in addition to the components in the cylindrical coordinate system. A secondary property of interest, the rotational transform, was also derived. Finally, simple but fairly realistic profiles for the plasma density and temperature were defined.

The model is applicable to large aspect-ratio devices with continuous windings. It is not applicable to helical axis or modular stellarators. The dominance of toroidal effects in small aspect-ratio devices preclude the application of this model as well.

Chapter 3

ECRF Propagation Theory

3.1 Introduction

The problem of electromagnetic wave propagation in plasmas is a widely researched subject. The propagation, occurrence, and damping of waves are important both for plasma heating and instability analysis.

Numerous experiments have been conducted to date on different plasma confinement devices for electron cyclotron range of frequencies (ECRF), and numerical and theoretical works are also in abundance [10-14]. However, these works are mostly for tokamaks and mirrors, and seldom for stellarators. Extrapolation of experimental results on these devices to stellarators can only be accomplished with detailed theoretical understanding. Theoretical works on these devices, on the other hand, are the starting point of stellarator ECRH analysis. This and other points will be discussed later.

In this chapter, wave propagation and absorption in the ECRF is discussed. Section 3.2 will describe the wave propagation in a cold plasma, defining and identifying resonances and cut-offs. Classification of different waves is also discussed. CMA diagram is presented and utilized to discuss accessibility. Section 3.3 will describe the damping mechanism of the wave in a finite

temperature plasma. Formulae for calculating the damping rate are presented here. Section 3.4 summarizes this chapter.

3.2 ECRF Propagation in a Cold Plasma

3.2.1 Appleton-Hartree Dispersion Relation

The discussion in this section will proceed with the understanding that the propagation characteristic, and therefore the ray trajectory of a wave in a hot plasma agrees well with that of a wave in a cold plasma as long as the wave does not approach cold plasma resonance or cut-off[10]. This condition that the wave not approach cold plasma resonance is required since the wavelength should be long compared to the electron Larmor radius, i.e., $k_{\perp} \rho \ll 1$, and the wave's phase velocity should be greater than the electron thermal velocity, i.e., $\frac{\omega}{k_{\parallel}} \gg v_e$. The condition that the wave not approach a cut-off is required since in a finite temperature plasma, tunneling and reflection take place at cut-off layers, which are not accounted for in the cold plasma theory.

Definitions of resonances and cut-offs will be clarified in a later section, but the above fact motivates the development of a ray-tracing code using a cold plasma dispersion relation, which is many times simpler than the hot plasma version. Furthermore, assuming an infinitely massive ion background and considering only the electron terms introduces little error since the region of interest is $\omega \simeq \omega_{ce}, \omega_{pe} \gg \omega_{ci}, \omega_{pi}$. Here, ω_c and ω_p are the cyclotron frequency and the plasma frequency, respectively, and e and i denote electrons and ions. In addition to simple algebra, cold plasma dispersion relation makes it easy to identify wave modes, resonances, and cut-offs.

The Appleton-Hartree dispersion relation is the standard cold plasma dispersion relation for high frequency waves. The derivation is given in many standard text books, such as Stix[11]. The assumptions are that the plasma is cold, infinite, and homogeneous, and that it is immersed in a homogeneous magnetic field. The dispersion relation, in its determinant form, is given by[11],

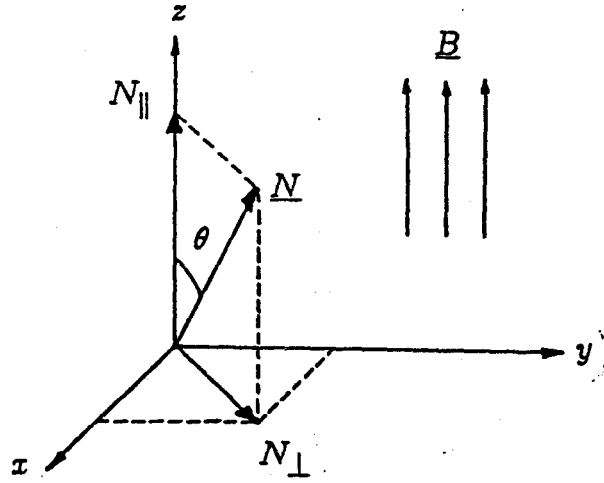


Figure 3.1 Appleton-Hartree Dispersion Relation Geometry

$$F = \det \begin{pmatrix} S - N^2 \cos^2 \theta & -iD & N^2 \cos \theta \sin \theta \\ iD & S - N^2 & 0 \\ N^2 \cos \theta \sin \theta & 0 & P - N^2 \sin^2 \theta \end{pmatrix} = 0 \quad (3.1)$$

where

$$R = 1 - \frac{\omega_{pe}^2}{\omega^2} \left(\frac{\omega}{\omega + \omega_{ce}} \right); \quad (3.2)$$

$$L = 1 - \frac{\omega_{pe}^2}{\omega^2} \left(\frac{\omega}{\omega - \omega_{ce}} \right); \quad (3.3)$$

$$S = \frac{1}{2}(R + L); \quad (3.4)$$

$$D = \frac{1}{2}(R - L); \quad (3.5)$$

$$P = 1 - \frac{\omega_{pe}^2}{\omega^2}; \quad (3.6)$$

$$\omega_{ce} = \frac{q_e B_0}{m_e}; \quad (3.7)$$

$$\omega_{pe} = \left(\frac{n_e e^2}{m_e \epsilon_0} \right)^{\frac{1}{2}}. \quad (3.8)$$

Here, N is the index of refraction, $N = \frac{kc}{\omega}$. The angle between the magnetic field vector and the wave vector, θ , is given by $\theta \equiv \cos^{-1} \frac{N \cdot B}{|N||B|}$ (Figure 3.1).

When the determinant is expressed in terms of N , the result is a quadratic equation for N^2 .

$$F = AN^4 - BN^2 + C = 0 \quad (3.9)$$

where

$$\begin{aligned} A &= S \sin^2 \theta + P \cos^2 \theta; \\ B &= RL \sin^2 \theta + PS(1 + \cos^2 \theta); \\ C &= PRL. \end{aligned} \quad (3.10)$$

When this equation is solved for N^2 , two roots are obtained, suggesting that two kinds of waves with a same frequency exist in a cold plasma.

Depending on plasma parameters, N^2 can take wide range of values. A resonance is defined as a point where N^2 goes to infinity, and a cut-off is defined as a point where N^2 goes to zero. At a resonance, the wave's group velocity, v_g , given by $v_g = \frac{\partial \omega}{\partial k}$, goes to zero, implying that the wave will remain at the resonance until it dissipates all its energy. At a cut-off, the wave is evanescent. In most cases, a wave approaching a cut-off point in an inhomogeneous plasma will reverse its direction and propagate away. Regions where N^2 is negative is the evanescence region. Cold plasma waves do not exist in this region.

Conditions for cold plasma resonances can be found from the dispersion relation (Equation (3.9)). Resonance condition ($N \mapsto \infty$) for perpendicular propagation ($\theta = \frac{\pi}{2}$) is given by $S = 0$, which, when solved for ω , gives the upper-hybrid resonance,

$$\omega = (\omega_{ce}^2 + \omega_{pe}^2)^{\frac{1}{2}}. \quad (3.28)$$

The cut-off condition ($N = 0$) is found when $P = 0$, $R = 0$, or $L = 0$. The relation $P = 0$ gives the plasma cut-off,

$$\omega = \omega_{pe}. \quad (3.29)$$

This condition sets an upper limit on the density of the plasma to which a wave can propagate. Conditions $R = 0$ and $L = 0$ gives the so-called right-hand

and left-hand cut-offs,

$$\omega = \frac{1}{2}(\pm\omega_{ce} + (\omega_{ce}^2 + 4\omega_{pe}^2)^{\frac{1}{2}}). \quad (3.30)$$

Here, the plus and the minus sign correspond to right and left cut-offs, respectively.

In the expression derived so far, N and θ specify completely the wave orientation with respect to the local magnetic field. Azimuthal orientation is not a consideration since the plasma is assumed to be isotropic(Figure 3.1). However, for computational purposes, it is more convenient to work with variables N_{\parallel} and N_{\perp} , which are the refractive indices parallel and perpendicular to the magnetic field, respectively. Written out in terms of these new variables, the dispersion relation to be dealt with becomes,

$$F = SN_{\perp}^4 + (N_{\parallel}^2(S + P) - PS - RL)N_{\perp}^2 + (PN_{\parallel}^4 - 2PSN_{\parallel}^2 + PRL) = 0. \quad (3.31)$$

3.2.2 Classifications of Waves in the ECRF

The quadratic solution to the dispersion relation suggests the existence of two waves with a same frequency, in regions where $B^2 - 4AC > 0$. A wave in a magnetized medium is classified in three ways. There are: the classification by the polarization of the wave electric field for $\theta = 0$ propagation; the classification by the orientation of the wave electric field with respect to the static magnetic field; and the classification by the magnitude of the phase velocity.

In the first classification, waves are termed right-hand-circularly-polarized or left-hand-circularly-polarized if the wave electric field rotates about the homogeneous magnetic field to the right or to the left, respectively. The second classification distinguishes between an ordinary wave and an extraordinary wave, evaluated at a propagation angle of $\theta = \frac{\pi}{2}$. The difference is the orientation of the wave electric field, which is parallel to the homogeneous magnetic field for the ordinary wave(O-wave) and perpendicular for the extraordinary wave(X-wave). These four cases are illustrated in Figure 3.2.

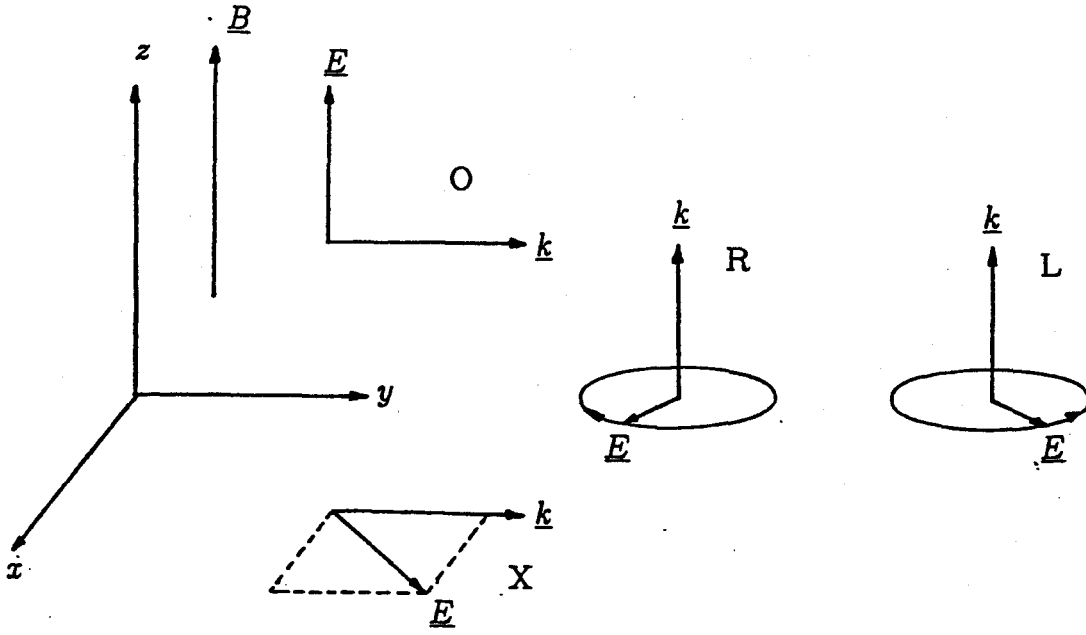


Figure 3.2 Fields of the O-mode, X-mode, RHCP, and LHCP Waves

The two kinds of classifications described above can be determined by solving the wave equation,

$$\underline{F} \cdot \underline{E} = 0, \quad (3.32)$$

for the wave electric field, with proper values of N and θ determined from $F = 0$. Specifically, for $\theta = 0$ propagation, the wave polarization is given by,

$$\frac{iE_x}{E_y} = \frac{N^2 - S}{D}. \quad (3.33)$$

The expression is equal to 1 if the wave is right-circularly-polarized, and is equal to -1 if the wave is left-circularly-polarized.

The third classification, that of fast and slow waves, is determined simply by comparing the magnitudes of the phase velocity, $v_{ph} = \frac{\omega}{k}$. Consequently, smaller root of N corresponds to the fast wave and the larger one to the slow wave.

To see all the information discussed in this section, use is made of a CMA(Clemmow-Mullaly-Allis) diagram(Figure 3.3)[11]. The vertical axis of the diagram shows the change in the magnetic field normalized to $\frac{\omega_{ce}}{\omega}$, and the

horizontal axis shows the change in density normalized to $\frac{\omega_{pe}}{\omega}$. R, L, O, and X in the diagram denotes right-hand, left-hand, ordinary, and extraordinary waves, respectively. A wave is classified both in terms of its polarization at $\theta = 0$ and electric field orientation at $\theta = \frac{\pi}{2}$, i.e., RX-waves, LO-waves, etc. The closed lines are the wave normal surfaces, oriented with respect to the magnetic field that is assumed to be pointed in positive y direction. A wave normal surface is a surface that is traced out by the tip of the phase velocity vector. The relative sizes of the wave normal surfaces distinguish between fast and slow waves. Resonances and cut-offs are indicated by captioned curves.

In the ECRF, there are five principal regions, labeled accordingly in Figure 3.3 with Roman numerals.

Region I is the high field region, thus termed because $\omega < \omega_{ce}$. Here, RX-wave and LO-wave both propagate.

Region II is the region between the electron cyclotron resonance and the upper-hybrid resonance. Again both waves exist, but RX-wave does not propagate at $\theta = 0$.

Region III is the evanescent region for the RX-wave.

Region IV is the low field edge region where both RX-wave and LO-wave exist.

Region V is beyond $P = 0$, or the plasma cut-off, and RO-wave does not propagate in this region.

Beyond the left-hand cut-off, there is no wave propagation.

In summary, X-wave sees the upper-hybrid resonance, the right- and left-hand cut-offs, while O-wave sees the plasma cut-off.

A resonance is said to be accessible if the wave injected from the edge of the plasma is able to reach it without encountering cut-off layers or evanescent regions on its trajectory. The CMA diagram can be used to schematically illustrate accessibility conditions. As the wave propagates into higher density region from the edge, the point on the diagram moves from somewhere on the vertical axis to the right. In addition, an increase in the magnetic field corresponds to a movement upward, and a decrease to a movement downward. Hence, the changes in the field and the density that the wave sees will result in a trajectory in the diagram.

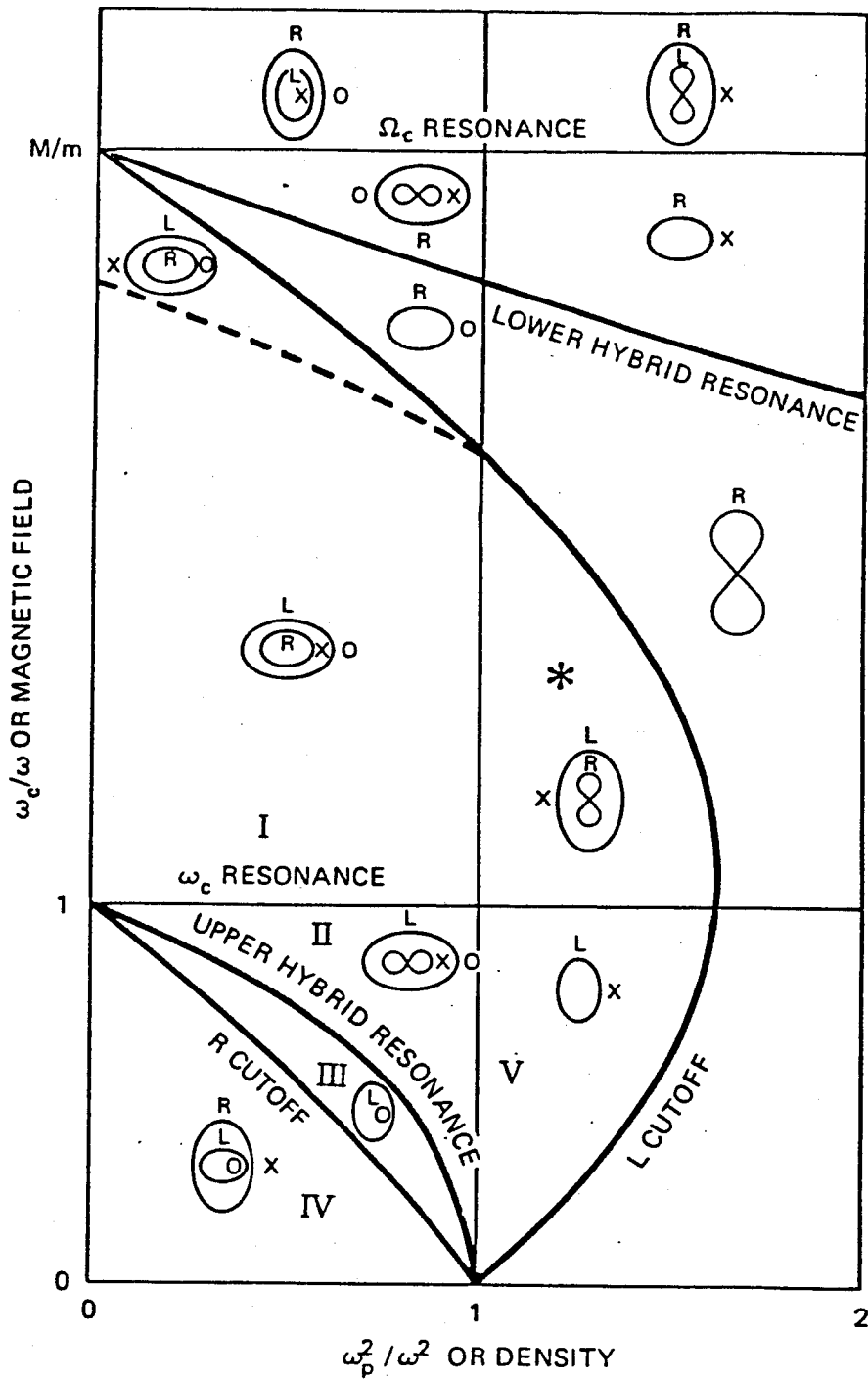


Figure 3.3 CMA Diagram[15]

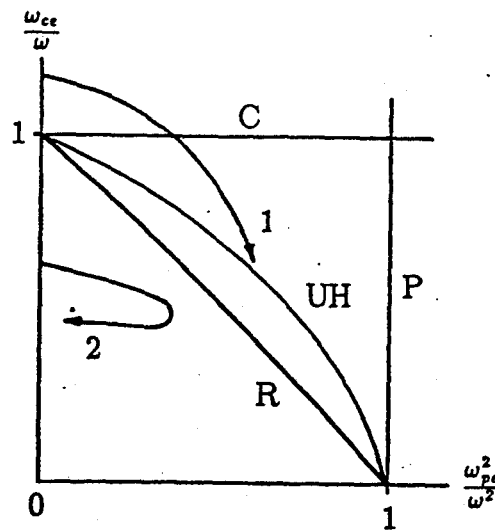


Figure 3.4 Accessibility on CMA Diagram

As an example, consider the accessibility to the upper-hybrid resonance of an extraordinary wave. Path 1 in Figure 3.4 shows a wave that was able to access the resonance. This wave started from a high field region and propagated to a lower field region. Path 2 in the same figure indicates a wave that was unable to access the resonance. Here, the wave encountered right-hand cut-off as it propagated from a low density region to a higher density region.

These results are strictly for an idealized cold plasma. For a finite temperature plasma, electron cyclotron resonances at the fundamental and the second harmonic are the dominant resonances for both the ordinary wave and the extraordinary wave. This will be discussed in the next section.

3.3 ECRF Absorption in a Finite Temperature Plasma

3.3.1 Finite Temperature Effects

In a finite temperature plasma, several things change with respect to the solution of the dispersion relation. First, the finite temperature dispersion relation is a transcendental equation with infinite number of roots for N .

This means that in addition to the O- and the X-waves present in the cold plasma, electrostatic waves also propagate. Next, the wave vector becomes complex where the real part contributes to propagation and the imaginary part contributes to damping. Furthermore, the magnitude of the wave vector remains finite at resonances, i.e., there is a limiting process on the damping rate.

The dominant power absorption mechanism in a finite temperature plasma is the cyclotron absorption at the fundamental electron cyclotron frequency, for which the collisionless dissipation and finite temperature effects are responsible[16]. For the X-wave, the perpendicular component of the electric field rotating in a right hand fashion resonates with the electrons if the condition that $\omega = \omega_{ce} + k_{\parallel}v_{\parallel e}$ is satisfied. Due to the velocity distribution of electrons, this resonance takes place over a finite band width, resulting in finite width resonance layer for non-zero values of k_{\parallel} .

For the O-wave, the component of the electric field parallel to the magnetic field transfers net energy to the electrons with finite Larmor radii, also if $\omega = \omega_{ce} + k_{\parallel}v_{\parallel e}$ is satisfied. Since the parallel component of the wave vector is responsible for the perpendicular fields, the absorption of X-waves is expected to increase with the decrease in the angle of propagation, θ . The absorption of O-waves is expected to decrease with the decrease in the angle of propagation since the electric field parallel to the magnetic field is excited by the perpendicular component of the wave vector.

The upper-hybrid resonance layer, which emerged straightforwardly in the Appleton-Hartree dispersion relation, takes on complicated physics in a finite temperature plasma. For temperatures up to a few electron-volts, power absorption takes place at the upper-hybrid layer due to nonlinear interactions[12]. Once the temperature is above several electron-volts however, mode conversion of the X-wave to the electrostatic plasma wave(Bernstein wave) becomes the dominant process[13]. Bernstein wave will then propagate backwards into the cyclotron layer and gets absorbed.

To properly account for the nonlinear processes at the upper-hybrid layer,

absorption, mode conversion, and tunneling must all be taken into account. Application of such detailed treatment to ray-tracing is beyond the scope of this thesis and is left as a future work.

3.3.2 Wave Damping Formulae

The fraction of the wave power transmitted through a resonance of length L in a homogeneous plasma can be expressed as,

$$T = e^{-2\text{Im}(k)L}, \quad (3.34)$$

where $\text{Im}(k)$ denotes the imaginary part of the wave vector. Note here that the overall absorption through a resonance depends on two factors, the magnitude of the imaginary part of the wave vector, and the width of the resonance in the direction of propagation. In an inhomogeneous plasma, the former is a local quantity determined by the plasma parameters and the value of the magnetic field, while the latter is determined by the magnetic field gradient scale length, which is set by the magnetic geometry.

The one dimensional transmission coefficient model has been evaluated by numerous authors for cyclotron resonances[10][12][14][16]. Here the case of the fundamental electron cyclotron resonance for the O- and the X-waves are presented. Using the notation of Antonsen and Porkolab[14], the general form for the transmission coefficient is given by:

$$T = \exp\left(-2\pi \frac{L_B \omega}{c} \frac{T_e}{m_e c^2} Q\right); \quad (3.35)$$

where, for the O-wave,

$$Q_{O1} = \frac{1}{4} \frac{\omega_{pe}^2}{\omega^2} \frac{\left(1 - \frac{\omega_{pe}^2}{\omega^2}\right)^{\frac{1}{2}}}{\left(1 + N_{\parallel}^2 \left(1 - \frac{\omega_{pe}^2}{\omega^2}\right)\right)}; \quad (3.36)$$

and for the X-wave,

$$Q_{X1} = N_{\parallel}^2 \frac{\left(1 + \frac{\omega_{pe}^2}{\omega^2}\right)^2 \left(2 - \frac{\omega_{pe}^2}{\omega^2}\right)^{\frac{1}{2}}}{4 \frac{\omega_{pe}^2}{\omega^2}}. \quad (3.37)$$

These expressions for T quantify the dependence of absorption on the temperature and density. Namely, in Q_{O1} , the increase of Q with density is approximately linear until $\frac{\omega_{pe}^2}{\omega^2}$ approaches 1, in which case the cut-off effect will reduce Q finally to zero (maximum Q_{O1} occurs at $\frac{\omega_{pe}^2}{\omega^2} \simeq 0.8$ [14]). For the X-wave, Q_{X1} goes as the inverse of density. As for the dependence on the wave vector, it can be seen that Q_{O1} increases with a decrease in k_{\parallel} and Q_{X1} increases with an increase in k_{\parallel} . The remaining terms in the exponent of the transmission formula indicate that absorption increases with increases in the temperature and magnetic field gradient scale length, L_B .

These expressions for the transmission coefficient are simple one-dimensional results and do not hold for an inhomogeneous plasma in a complicated magnetic geometry. Therefore, in order to assess accurately the local damping term in this kind of situation, an expression should be found for $\text{Im}(k)$ on and around the resonance.

Since the physics at the upper-hybrid layer is neglected, and since at present stage, only the fundamental heating is realistic due to low frequency sources available; it is sufficient to consider the damping at the fundamental resonance. Search for existing methods of obtaining the damping term uncovered the results of Batchelor[17].

Assumptions are:

$$\text{Re}(k) \gg \text{Im}(k), \quad (3.38)$$

$$k_{\perp} \rho_e \ll 1, \quad (3.39)$$

and,

$$\frac{(\omega - l\omega_{ce})}{k_{\parallel} v_e} \gg 1 \quad (l \neq 1), \quad (3.40)$$

i.e., weak damping, the perpendicular wavelength large compared to the Larmor radius, and the wave frequency close to the fundamental cyclotron frequency. Then, expansion of the finite temperature terms about the cold plasma dispersion relation leads to the following expression for $\text{Im}(k)$ [17].

$$\text{Im}(k) = -\frac{\omega}{c} \frac{2 \frac{v_e}{c} \cos \theta N \Lambda_1}{\frac{\omega_{pe}^2}{\omega^2} \frac{\partial \Lambda_0}{\partial N}} \text{Im} \left(\frac{1}{Z(\xi)} \right), \quad (3.41)$$

where,

$$\Lambda_0 = \sin^2 \theta N^4 - \left((1-P)(1 + \cos^2 \theta) + (2-4q) \sin^2 \theta \right) N^2 + 2(1-P)(1-2q), \quad (3.42)$$

$$\begin{aligned} \Lambda_1 = & \left(\left(1 - q + P \frac{\omega}{\omega_{ce}} \right) \sin^2 \theta + (1-P) \cos^2 \theta \right) N^4 \\ & - \left((1-q)(1-P)(1 + \cos^2 \theta) - P^2 \frac{\omega^2}{4\omega_{ce}} (1 + \cos^2 \theta) \tan^2 \theta \right. \\ & \left. + \left(1 + P \frac{\omega}{\omega_{ce}} \right) (1-2q) \sin^2 \theta \right) N^2 \\ & + (1-P)(1-2q) - P^2 \frac{\omega^2}{2\omega_{ce}} (1-2q) \tan^2 \theta. \end{aligned} \quad (3.43)$$

Here, P is defined in Equation(3.6), θ is the propagation angle, N is the index of refraction, and $q = \frac{\omega_{pe}^2}{2\omega(\omega + \omega_{ce})}$. The electron thermal velocity is denoted by v_e , and $Z(\xi)$ is the plasma dispersion function, with the argument ξ given by $\xi = \frac{(\omega - \omega_{ce})}{k_{\parallel} v_e}$ [18].

The further limitation of the formula in addition to Equations (3.38) through (3.40) is that the relativistic effect, which becomes important for $N_{\parallel} \leq \frac{v_e}{c}$, is neglected. However, this effect is primarily on the shape of the absorption profile and not on the total absorption[14], so it does not necessarily rule out the application of Equation (3.41) to nearly perpendicular propagation.

3.4 Summary

The highlights of ECRF propagation characteristics were discussed in this chapter. Following a brief overview, Appleton-Hartree dispersion relation for waves in a cold plasma was presented, and resonances and cut-offs as defined in the dispersion relation were extracted. Three methods for the classification of waves in the ECRF, of which there are two, were introduced. Finally, CMA diagram was reviewed, and an example given on the accessibility to the upper-hybrid resonance by the extraordinary mode of propagation.

In Section 3.3, absorption of waves due to finite temperature effects were discussed. In a finite temperature plasma, infinite number of roots are found,

the wave vector becomes complex, and the wave number is finite at resonance. The dominant absorption is at the cyclotron resonance for both O- and X-waves, and the upper-hybrid layer becomes a mode conversion layer for temperatures above a few electron-volts. Cyclotron absorption increases with magnetic field gradient scale length and temperature, and also depends on k_{\parallel} and density.

In the latter part of Section 3.3, transmission coefficient formulae were introduced for the two modes, and dependencies of T on T_e , n_e , L_B , k_{\parallel} were quantified. Noting that these one-dimensional approximations were inaccurate for complicated geometry, damping formula for arbitrary angle of propagation in a complex geometry was presented to be used in the computer code. This formula takes into account the relevant effects at the cyclotron layer except for the relativistic effect which is important for nearly perpendicular propagation and affects the shape of the damping profile.

Chapter 4

Ray Tracing

4.1 Introduction

In this chapter, a widely accepted technique for wave propagation analysis in a magnetized plasma is introduced and developed. The WKB(Wentzel-Kramers-Brillouin) theory, otherwise known as geometrical optics, is the method in question.

It is easier to see what the theory entails by listing the approximations employed, rather than by attempting to define the theory in words or formulae. The assumptions of the WKB approximation are:

- (1) perturbed wave fields are small compared to static fields;
- (2) the characteristics of the propagation medium change slowly both in time and space, compared to the wavelength or the frequency of the wave;
- (3) the change in wavelength in space and time is small compared to its magnitude;
- (4) the wave is weakly damped, i.e., the perturbed field amplitudes must be slowly varying and the imaginary part of the wave vector must be small compared to the real part.

Proceeding from the WKB approximation, further assumptions entail the use of a ray-tracing technique. The assumptions here are:

- (1) the medium is isotropic in the vicinity of the ray front;
- (2) the waves are plane waves, with the direction of propagation normal to the plane wave front.

The technique involves solving a set of differential equations that characterize the wave propagation in the medium, with a proper initial condition on the ray initiation point and direction.

Ray-tracing in a plasma has been investigated by many authors[19-24]. However, almost all the application in this area up to now has been done on either the tokamaks or mirrors, with the majority of the work done on the former. Since the full three-dimensional analysis of the ray equations add to complexity and computer time, many of the works cited above reduce the free parameters of the analysis either by changing the geometry(e.g., a straight tokamak), or assuming additional symmetry(e.g., concentric flux surfaces), or both. For example, a perpendicularly stratified slab model with $\frac{1}{R}$ varying magnetic field and parabolic plasma profiles is used to simulate a tokamak[20]. These assumptions are justified for simplified analysis of ECRF, which is precisely what Reference [20] is treating; however, when lower hybrid waves are considered for example, toroidal eigenmodes play an important role, and the toroidal effect cannot be left out[21-22].

As it was stated in Chapter 2, the model used in this thesis also neglects toroidal effects and even the $\frac{1}{R}$ fall-off of the magnetic field. However, unlike tokamaks, symmetry in the z direction does not exist in stellarators so that even though the magnetic field and the plasma parameters can be completely specified by r and ϕ as it was shown in Chapter 2; all three dimensions, r , θ , and z are needed to specify completely the trajectory of the wave, i.e., ray-tracing in stellarators is inherently a three-dimensional problem. This fact also rules out the possibility of simplification by assuming parallel or perpendicular stratification.

In the following sections, ray equations for arbitrary stratification in three-dimensional medium are derived in cylindrical coordinates. The equations are then manipulated to obtain suitable forms for computation. The damping formula introduced in Chapter 3 is also treated to give the expression for power absorption in computable form. Limitations, both theoretical and practical are then discussed, followed by a summary.

4.2 Derivation of the Ray Equations

In the rest of this work, waves will be characterized by \underline{k} and ω , the wave vector and the frequency. The wave vector notation is chosen over the index of refraction, N , used in Chapter 3 since the former relates more readily to the physical environment with its dimension of inverse length. It is also the commonly used variable in WKB treatment.

In the WKB approximation, the wave field is expressed as[23],

$$f = A_0 e^{i(\underline{k} \cdot \underline{x} - \omega t)}. \quad (4.1)$$

Here, A_0 is assumed constant compared to the phase factor $S = \underline{k} \cdot \underline{x} - \omega t$, which is also called the *eikonal*. In the plasma, $F(\underline{x}, \underline{k}, \omega) = 0$ must be satisfied everywhere, where F is the dispersion relation. The equations governing this condition, the ray equations, can be derived applying this eikonal approximation to the linearized Maxwell's equations[11]. They are:

$$\frac{d\underline{x}}{d\tau} = \frac{\partial F}{\partial \underline{k}}; \quad (4.2)$$

and

$$\frac{d\underline{k}}{d\tau} = -\frac{\partial F}{\partial \underline{x}}. \quad (4.3)$$

Here, τ is a dimensionless parameter along the ray. For a more general case of $F = F(\underline{x}, \underline{k}, \omega, t) = 0$, another equation relating τ to t can be obtained.

$$\frac{dt}{d\tau} = -\frac{\partial F}{\partial \omega}. \quad (4.4)$$

Combining these three relations will yield two vector ray equations with physical significance, namely:

$$\frac{d\mathbf{x}}{dt} = -\frac{\frac{\partial F}{\partial \mathbf{k}}}{\frac{\partial F}{\partial \omega}}, \quad \text{group velocity equation;} \quad (4.5)$$

and

$$\frac{d\mathbf{k}}{dt} = \frac{\frac{\partial F}{\partial \mathbf{x}}}{\frac{\partial F}{\partial \omega}}, \quad \text{Snell's law equation.} \quad (4.6)$$

The ray equations, as they are written in cartesian coordinates, are separate component-by-component equations. However, for the present case it is preferred to derive these equations in cylindrical coordinates since the magnetic field and the plasma profiles are given in the same. To carry the step further to helical coordinates would have introduced additional steps because of the scale factors which are not straightforward, and since the plotting of results are done in stationary(cylindrical) coordinates.

When the equations are derived in general orthogonal curvilinear coordinates, such as the cylindrical coordinates, effects of the coordinate curvature and the variation of the scale factors must be taken into account[21]. Hence, a general expression for a single component of the Snell's law equation is,

$$\frac{1}{h_i} \frac{d}{dt} h_i k_i = \frac{1}{\frac{\partial F}{\partial \omega}} \left(\frac{1}{h_i} \frac{\partial F}{\partial \xi_i} + \sum_j \frac{\partial F}{\partial k_j} \frac{k_j}{h_j h_i} \frac{\partial h_i}{\partial \xi_i} \right), \quad (4.7)$$

where ξ 's are the coordinates and h 's are the scale factors. Subscripts i and j denote the three components of the coordinate system(r , θ , and z for cylindrical coordinates). Then the Snell's law equations in cylindrical coordinates become:

$$\frac{dk_r}{dt} = \frac{1}{F_\omega} \left(F_r - F_{k_\theta} \frac{k_\theta}{r} \right); \quad (4.8)$$

$$\frac{d(\tau k_\theta)}{dt} = \frac{F_\theta}{F_\omega}; \quad (4.9)$$

$$\frac{dk_z}{dt} = \frac{F_z}{F_\omega}. \quad (4.10)$$

Here the short hand notation using subscripts is introduced. A subscript of F implies partial differentiation of F with respect to that subscript, but subscripts

of k refer to the particular components of k . For example, F_{k_θ} denotes the partial differentiation of F with respect to the θ component of k . The group velocity equations are still rather straightforward, save the scaling factor for the θ component.

$$\frac{dr}{dt} = -\frac{F_{k_r}}{F_\omega}; \quad (4.11)$$

$$r \frac{d\theta}{dt} = -\frac{F_{k_\theta}}{F_\omega}; \quad (4.12)$$

$$\frac{dz}{dt} = -\frac{F_{k_z}}{F_\omega}. \quad (4.13)$$

The actual form of the equations is still more complicated, since the derivatives of the dispersion relation with respect to k_r , k_θ , and k_z must be converted to the derivatives with respect to k_\perp and k_\parallel using the chain rules; because the dispersion relation is expressed in terms of the latter. Using the relation that:

$$k_\parallel = \frac{\mathbf{k} \cdot \mathbf{B}}{|\mathbf{B}|}; \quad (4.14)$$

$$k_\perp = (k^2 - k_\parallel^2)^{\frac{1}{2}}; \quad (4.15)$$

and applying chain rules, the following relationships can be obtained.

$$F_{k_i} = F_{k_\perp} \frac{\partial k_\perp}{\partial k_i} + F_{k_\parallel} \frac{\partial k_\parallel}{\partial k_i}; \quad (4.16)$$

$$\frac{\partial k_\perp}{\partial k_i} = \frac{k_i}{k_\perp} - \frac{k_\parallel}{k_\perp} \frac{B_i}{|\mathbf{B}|}; \quad (4.17)$$

$$\frac{\partial k_\parallel}{\partial k_i} = \frac{B_i}{|\mathbf{B}|}. \quad (4.18)$$

Finally, substituting Equations (4.16) through (4.18) into (4.8) through (4.13), the six ray equations for numerical evaluation become:

$$\frac{dk_r}{dt} = \frac{1}{F_\omega} \left(F_r - \frac{k_\theta}{r} F_{k_\perp} \left(\frac{k_\theta}{k_\perp} - \frac{k_\parallel}{k_\perp} \frac{B_\theta}{|B|} \right) + F_{k_\parallel} \frac{B_\theta}{|B|} \right); \quad (4.19)$$

$$\frac{d(rk_\theta)}{dt} = \frac{F_\theta}{F_\omega}; \quad (4.20)$$

$$\frac{dk_z}{dt} = \frac{F_z}{F_\omega}; \quad (4.21)$$

$$\frac{dr}{dt} = -\frac{1}{F_\omega} \left(F_{k_\perp} \left(\frac{k_r}{k_\perp} - \frac{k_\parallel}{k_\perp} \frac{B_r}{|B|} \right) + F_{k_\parallel} \frac{B_r}{|B|} \right); \quad (4.22)$$

$$r \frac{d\theta}{dt} = -\frac{1}{F_\omega} \left(F_{k_\perp} \left(\frac{k_\theta}{k_\perp} - \frac{k_\parallel}{k_\perp} \frac{B_\theta}{|B|} \right) + F_{k_\parallel} \frac{B_\theta}{|B|} \right); \quad (4.23)$$

$$\frac{dz}{dt} = -\frac{1}{F_\omega} \left(F_{k_\perp} \left(\frac{k_z}{k_\perp} - \frac{k_\parallel}{k_\perp} \frac{B_z}{|B|} \right) + F_{k_\parallel} \frac{B_z}{|B|} \right). \quad (4.24)$$

Magnetic field components in the plasma are obtained by the expressions in Chapter 2, and partial derivatives of F can be calculated separately (Appendix A). Thus Equations (4.19) through (4.24) are the six ray equations in a suitable form for computation. They can be solved for the six unknowns, $r, \theta, z, k_r, k_\theta,$ and k_z given a proper initial condition.

In Chapter 3, the imaginary part of the wave number was derived using a finite temperature approximation. Since the wave fields can be expressed as given in Equation (4.1), it follows that the damping decrement of the field is given by

$$\delta f = A_0 e^{-\text{Im}(k)\delta x}, \quad (4.25)$$

where δx denotes the change in the position of the wave front. The power decrement is just the square of this. Therefore, this formula can be used to calculate the power absorption at each step, accumulation of which will give the total damping taking place up to the specified position. Written out in integral form, this becomes,

$$f(\underline{x}) = A_0^2 e^{-2 \int_0^{\underline{x}} \text{Im}(k(\underline{x})) \cdot d\underline{x}}, \quad (4.26)$$

where A_0^2 implies power relationship. The expression for $\text{Im}(k)$ as given in Equation (3.41) is already suitable for computation, so it need not be reevaluated here. There is some ambiguity as to the direction of the imaginary part of the wave vector, since the damping formula is a scalar expression. Here, it is taken to be in the same direction as the real part of \underline{k} [17].

4.3 Limitations

Limitations of the ray equations, or of the results predicted by them, are numerous. First, there is the inherent limitation that is embodied in the dispersion relation. Second, there is the mathematical limitation in which regions where one or all of the equations are not analytical (also inherent in the dispersion relation as well). Finally, there is the theoretical limitation which puts a limit on the validity of the solution.

The first limitation of the dispersion relation is that the wave range is limited to the ECRF, and that no tunneling, mode conversion, or partial reflection is permitted at the upper-hybrid layer and the right-hand cut-off layer. In order to alleviate the difficulty of ECRF boundary, ion terms may be introduced. It is a trivial task, but not done here since the region of interest is, in fact, ECRF. For the other restriction, mathematical models of tunneling and mode conversion can be constructed and connected in a piece-wise fashion but this also requires deeper investigation into quasilinear and asymptotic processes, which is beyond the scope of this thesis.

The second limitation of mathematical difficulty arises whenever a partial derivative becomes too large or too small, and except for absolute divergence to infinity, the problem may be termed as numerical. In particular, there is an instability in the region of small radius. Although this is something that cannot be avoided, it is possible not to lose continuity by "bracketing" the rays, i.e., shoot one above and one below the instability and interpolate. The problem of large gradient often arises near the plasma edge.

The third limitation on the interpretation has two parts. The first has to do with items (2) and (3) of the WKB approximation assumptions. Condition (2) is equivalent to demanding that,

$$Lk \gg 1. \quad (4.27)$$

where L is the scale length of the gradients of the medium. This condition is not satisfied in the edge regions where gradients are large (L is small), and near cut-off regions where k is small. For condition (3), the mathematical expression is given by McVey[23],

$$\nabla k \cdot \left(\frac{k}{k} \right) \ll k^2. \quad (4.28)$$

This equation states that the change of k along the direction of propagation must be small compared to the magnitude. Second item of the third limitation has to do with WKB approximation assumptions (1) and (4) introduced at the beginning of this chapter, in addition to the fact that the wave fields should have nearly constant amplitudes (Equation (4.1)). This puts a limit on the applicability of the approximation to the actual plasma heating problem where wave fields may be comparable to the static field. This limit is also consonant with the limits on the damping formula, namely that the ray should be weakly damped, and $\text{Re}(k) \gg \text{Im}(k)$.

4.4 Summary

The ray-tracing technique for numerical analysis of wave propagation was presented in this chapter. In the introduction, underlying assumptions of WKB approximation and ray-tracing technique were discussed. Here, past works of ray-tracing on tokamaks and mirrors, and the assumptions made in them were discussed. It was found that some of the assumptions, plane stratification for example, are not valid for the straight stellarator model, and that a full three-dimensional treatment is required. So in Section 4.2, the six ray equations in cylindrical coordinates suitable for computation were derived. Using the expression for the imaginary part of the wave vector derived in Chapter 3, a power absorption formula was presented, also in a form suitable for coding.

Section 4.3 discussed the limitations, both theoretical and practical, of this analysis. The cases in which the analysis can be applied are determined by whether or not the dispersion relation accounts for all the phenomena for that

case. In this work, cases are limited to ECRF and cyclotron resonance due to the nature of the dispersion relation and the damping formula. Numerical instabilities may prohibit evaluations of certain cases, but this can be alleviated by bracketing and interpolation. Even if all the physical phenomena are treated, and no numerical difficulties arise, there is the question of whether or not all the assumptions underlying the theory are satisfied. It is found that in some parameter regions, this is not the case, and that limits are placed on the validity of the results.

Chapter 5

Helical Plasma Ray Tracing Code(HERA)

5.1 Introduction

The computer codes developed for this thesis are described here. The reader who is not interested in the particulars of the codes is assured that skipping this chapter will not result in the loss of continuity.

The three computer codes developed for this research are:

- (1) MAC (MACHINE parameters code);
- (2) HERA (HELICAL plasma RAY tracing code);
- (3) GROUT (GRAPHICS OUTPUT code).

These three codes reside on the CRAY-I computer at MFECC(Magnetic Fusion Energy Computer Center). MAC is a code that, for given input parameters, executes the modeling of a straight stellarator, and outputs suitable graphics for easy interpretation and visualization of the determined model. HERA, which is the most complex of the three, does the ray-tracing based on the geometry defined by MAC, and outputs a data file in text format. GROUT creates graphics using the output from HERA. In Section 5.2, processes involved in developing HERA are discussed. Description of the three codes follow in Section 5.3.

5.2 Code Development

Development of HERA involved the following evolution processes:

- (1) confirm the use and workings of EXTINT[25], the numerical integrator;
- (2) confirm the accuracy of the cold plasma dispersion relation and its derivatives;
- (3) confirm the accuracy of the ray equations;
- (4) incorporate the damping routine.

In phase one, the simplest possible ray-tracing code was written as an exercise. This was a code incorporating a slab geometry with constant magnetic field, parabolic density and temperature profiles, and a Bohm-Gross wave dispersion relation[11]. This problem is one-dimensional, and the wave trajectory can be found analytically, so it is easy to see by inspection whether the dispersion relation and its derivatives, ray equations, density and temperature profiles were correct or not. Therefore, this exercise served as one for checking the particular version of EXTINT used in the code.

In phase two, the Appleton-Hartree dispersion relation was checked for several points in parameter space to insure that physically correct solution is given. For example, $N = 0$ at a cut-off point, large N at a resonance, etc. Then the partial derivatives of the dispersion relation were derived(Appendix A), these were checked by a finite difference method.

Before proceeding to phase three, MAC was developed. This served as a check for the family of magnetic field equations. Then in phase three, the derivation of the ray equations were carried out, as outlined in Chapter 4. The only way to fully verify the equations was to try them out in the actual straight stellarator geometry. After some debugging, the ray equations were verified and HERA started running.

For phase four, literature search produced the results of Batchelor et. al. on the ray-tracing analysis of ECRH in EBT[24]. As presented in Chapter 3,

the damping formula was reviewed and adopted. The damping rate predicted by the code was bench-marked against one-dimensional absorption coefficient calculations available from other sources[14].

5.3 Structures of HERA, GROUT, and MAC

5.3.1 MAC

MAC determines and outputs the magnetic field configuration of the straight, helically symmetric plasma, given the input parameters B_o , B_h , l , and α , where the quantities are defined in Chapter 2. Due to the finite physical dimensions of the helical windings, the modeling of a real machine requires considering contributions from the machine l and $2l$ fields. MAC is capable of superimposing up to three fields generated by conductors corresponding to different l numbers. It will also find the position of the saddle point which defines the separatrix, and the value of the flux function on the separatrix; the latter is needed to determine the expressions for the plasma density and temperature profiles (Equations (2.16) and (2.17)). The flux surface in the $r - \phi$ plane is plotted, and superimposed on this plot are the electron cyclotron, upper-hybrid, and right cut-off surfaces given a suitably defined density profile. It will also compute $t_{f.p.}$, the rotational transform per field period, versus the average radius over the poloidal cross-section. These are used to generate the rotational transform profile useful in determining whether or not a particular combination of machine parameters accurately model an existing or proposed experiment. MAC uses both the NAG and TV80LIB libraries residing on the MFECC CRAY-I.

Subroutines of MAC include contour plotting routines, root finders, and flux and field component functions. Since the flux function is multi-valued, the root finding with respect to the search for the saddle point is sensitive to the initial guess given by the user.

5.3.2 HERA

HERA is a ray-tracing code for ECRF waves in a plasma confined in a straight stellarator. It solves the ray equations (Equations (4.19) through (4.24)) given appropriate initial conditions and the time step interval.

The input to the code are the following quantities:

- (1) machine parameters, determined by MAC;
- (2) plasma parameters;
- (3) wave parameters;
- (4) code options.

These total approximately 35 numbers for any given run.

HERA produces a text output file. Information contained in this output file includes:

- (1) position of the ray at each step;
- (2) wave vector components at each position;
- (3) damping decrements;
- (4) wave amplitude and power at each position;
- (5) power deposition rate at each position;
- (6) value of the magnetic field, density, and temperature along the ray.

The code is modularized into 23 subroutines each of which belongs to one of the following groups.

- (1) Wave launching and initialization routines.
- (2) Dispersion relation and its derivatives routines.
- (3) Magnetic field and plasma parameters routines.
- (4) Ray equation generating routines.
- (5) Damping decrement calculators.
- (6) Numerical integrator package (EXTINT).
- (7) Special function routines.
- (8) Checking routines.
- (9) Root finders.
- (10) Data storage and normalization routines.

Theoretical details of group (2) are explained in Chapter 3 and Appendix A; group (3), in Chapter 2; group (4), in Chapter 4; group (5), in Chapters 3 and 4; group (6), in Boris and Winsor[25]. Groups (9)[26] and (10) are utility routines. For group(7), special functions, there are the modified Bessel function and the plasma dispersion function. Modified Bessel function routine uses the IMSL library plus recursion formulae[27] to evaluate the function and its first derivative. The plasma dispersion function subroutine is obtained from Callen[28]. Groups (1) and (8) are of particular interest to the operation of the code, and they are described below.

Group (1) is the initialization and launching routines. Since the code is solving an initial value problem, incorporating the ability to specify the initial condition with sufficient degree of freedom is most important. When the code is executed, the ray is launched somewhat inside the plasma to avoid numerical instabilities arising from the large values of the density gradient at the edge. In addition to the specification of the wave mode and the launching position, HERA gives four options with respect to the specification of the initial conditions. As illustrated in Figure 5.1, they are:

- (1) launch the wave with k_{\perp} perpendicular to the flux surface, and with a specified k_{\parallel} ;
- (2) launch the wave with k_{\perp} aimed at the plasma axis, and with a specified k_{\parallel} ;
- (3) launch the wave with specified k_{θ} and k_{\parallel} (if compatible) from the saddle point;
- (4) launch the wave at some point external to the plasma with specific k .

First and second options are included by virtue of their simplicity. The novice user will need to specify only some position and k_{\parallel} . If the point specified is inside the plasma, it is unaltered. If it is outside, value of r will be reduced so that the ray starts near the edge(options (1), (2), and (3)). Option (3) is convenient for evaluating the effects of the launching angle with the same k_{\parallel} . Option (4) allows complete freedom in the specification of the initial condition.

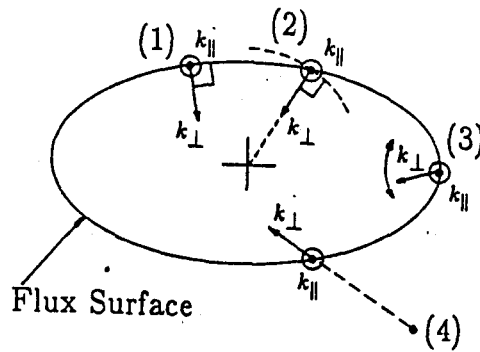


Figure 5.1 Launching Options for HERA

It is useful, for example, when a specific radiation pattern is desired for an antenna design. Extensive use of this last option is made in Chapter 7.

Note that options (1) and (2) will effectively collapse to one, for example, in the case of a tokamak with concentric flux surfaces and very strong toroidal field. In the case of a slab model, options (1) through (3) are one and the same. Here again, the three dimensional nature of the stellarator manifests in the need to fully specify all three components of the wave vector in order to have total control over the specification of the initial condition.

Group (8) is the checking routines. The code will terminate under the following cases.

- (1) Prescribed maximum number of steps have been performed.
- (2) The ray is out of the plasma.
- (3) 99 % of the wave power has been absorbed.
- (4) WKB approximation is violated.
- (5) Solution of the ray equations disagree with the dispersion relation.
- (6) Some sort of numerical instability is encountered and the integrator fails to converge.

Cases (1) through (3) are what is expected of the code. In case (4), the magnitude of the change of the wave vector relative to the magnitude of the

vector itself, is compared at each step to insure that Equation (4.28) is not violated. This condition is encountered mostly near cut-offs or the edges. Case (5) occurs most frequently when the ray is nearing the end of its trajectory in the edge region, the poor convergence of the equations due to the large values of the gradients cause this failure mode. Case (6) may manifest itself as it is, by terminating the execution of EXTINT after a prescribed number of attempts, or by causing the solution to "jump", i.e., find convergence in the parameter space far away from the previous point. For example, the ray may suddenly traverse the entire poloidal cross-section in one step and find itself outside the plasma(Case (2)).

In order to ensure the proper convergence of the integrator, a small enough time step must be selected. On the other hand, too small a time step would produce too large an output file and consume large amounts of CPU time. For this reason, finding an appropriate time interval is very important. Cases have shown that time intervals differing by only a factor of 1.5 can give grossly different results. For example, $\delta t = 1.0 \times 10^{-13}$ may give a valid result while $\delta t = 1.5 \times 10^{-13}$ may fail after 100 steps. Since EXTINT automatically reduces the time interval until it finds convergence, this would present little problem if the convergence was unique. However, the convergence is sometimes found in physically unacceptable parameter space as mentioned above, so that careful selection of δt is, in fact, necessary. In general, edge regions and central regions give most trouble due to large gradients and small radii, respectively. However, false convergence occurs mainly in the edge region. For this reason, HERA's code options include the capability to increase the time step after certain number of steps, i.e., after the large gradient region has been traversed. In this way, both the convergence and the economy are satisfied.

Typical execution time of HERA is around 10 seconds for 2000 steps on the MFECC CRAY. It requires the NAG library.

5.3.3 GROUT

GROUT requires the output file from HERA and a separate code option file

for input. The ray trajectory is plotted in:

- (1) $r - \theta$ plane;
- (2) $r - \phi$ plane;
- (3) $r - z(\theta = 0)$ plane.

After these come plots of the real part of the wave vector, the imaginary part of the wave vector, the wave amplitude, and the wave power versus t , r , θ , z , and ϕ . Finally, there are the plots of r , θ , z , ϕ , $|B|$, n_e , and T_e versus t .

Different versions of GROUT have been created in the course of the research. For example, most of the plots in Chapter 7 are created using GROUT2, which is capable of superimposing up to 10 rays on one frame. GROUT may be modified to produce only those outputs required for a specific analysis.

5.4 Summary

In this chapter, the three computer codes, MAC, HERA, and GROUT, that were developed for this thesis have been described. Development of HERA was a multi-stage process owing to the number of uncertain procedures involved. The stages included verifying the integrator, the derivatives, the ray equations, and the damping term. MAC determines the machine and plasma parameters of the model. HERA does the ray tracing calculation. Some fine points in implementing HERA include selection of the options for determining the initial condition, and choosing appropriate code options for a successful run and good economy. GROUT is a separate graphics code for output, with enough flexibility for personal tailoring.

A typical procedure for implementing these three codes will be to first find the parameters that model an existing or proposed experiment using MAC, run ECRH cases with HERA and produce output using GROUT.

Chapter 6

Simulation Models of Stellarators

6.1 Introduction

In this chapter, specific models of the straight stellarators used for ECRH simulation will be defined. First, modeling criteria are defined in Section 6.2 to determine whether the model simulates the magnetic field geometry and the plasma parameters of a particular device. This section will also indicate how to converge on a model, starting from available specifications. In, Sections 6.3 through 6.5, three models are defined. One will closely approximate Heliotron E, while another will approximate Wendelstein VII A. The third model will be that of a fictitious $l = 3$ stellarator. The reasons for these selections will also be given. Section 6.6 is the summary.

6.2 Modeling Criteria

Criteria, and therefore a hierarchy of priorities must be set up in order to model a device since the simplified mathematical model cannot reproduce the device in every detail. Choice has to be made as to what the important properties

are, and what can be left out.

It was decided early that the toroidal effects will be neglected, hence the introduction of a straight stellarator in Chapter 2, and steady-state is assumed as well. The two major categories for modeling are the magnetic geometry and plasma parameters.

Quantities to be observed with respect to the magnetic geometry are:

- (1) l number;
- (2) inverse winding pitch(α);
- (3) magnetic field strength on axis(B_o);
- (4) rotational transform profile(when available);
- (5) distance from the axis to the separatrix, or, the general size and shape of the last closed flux surface.

Items (1), (2), and (3) are simple to adhere to since they appear directly in the equations for the magnetic field(Equations (2.2) through (2.4)). For a toroidal device, α is defined as,

$$\alpha \equiv \frac{m}{lR}, \quad (6.1)$$

where m is the poloidal rotation number and R is the major radius.

The last two items, (4) and (5) must be adjusted using the remaining free parameters which are the helical field strengths, both the fundamental and the harmonic. The method to follow in order to determine these quantities is to find a value of B_{hl} that will give the desired rotational transform on the axis; then introduce B_{h2l} (positive or negative) to adjust the radius of the separatrix since the effect of B_{h2l} on the rotational transform on axis is much less than that of B_{hl} .

The two quantities to be observed with respect to plasma parameters are the density and temperature profiles. Ion species density and temperature does not enter into consideration in the ECRF(Chapter 3).

As it has been discussed in Section 2.5, these profiles will be modeled as simple functions of the flux function(Equations (2.16) and (2.17)). Here the problem of

time dependence emerges. Namely, the profiles at the end of the RF pulse will be different from that at the beginning of the pulse in an experiment. Clearly, such evolution of the profiles cannot be considered without the extensive addition of a Fokker-Planck analysis and time dependent ray-tracing. Since such investigations are beyond the scope of this thesis, profiles are determined in a time averaged sense. Furthermore, the simple forms of the density and the temperature as given in Chapter 2 and used in the code prohibit the modeling of a complicated profile, a dip in the central density or temperature, for example, which sometimes occur for ECRH start-up.

6.3 Heliotron E

Heliotron E is a large heliotron device operating since 1981 at Kyoto Plasma Physics Laboratory. This machine currently has 200 kW of 28 GHz ECRH on line, and 54 GHz is expected in the near future[29]. Machine specifications, plasma parameters, and ECRH parameters are listed in Table 6.1[30]. This machine is an ideal one to be simulated by the straight model due to its small toroidal effect[31].

MAC was implemented to arrive at the model parameters shown in Table 6.2; the rotational transform profile in Figure 6.1; and a view of a poloidal cross-section, with resonance and cut-off layers in Figure 6.2. Figure 6.1 shows good agreement between the actual machine transform and the model transform, particularly for the central region. The rotational transform near the edge in an actual machine is affected by the toroidal effect so that MAC cannot be expected to reach an agreement on the profile in this region. The layers shown in Figure 6.2 are for the case of a wave frequency corresponding to the cyclotron frequency on axis. The ECRF launching geometry for Heliotron E is illustrated in Figure 6.3. Here the wave is injected from the low field side, and most of the radiated energy is within 20° of the radiated cone.

Table 6.1
Heliotron E Parameters

Major Radius	$R = 2.2m$
Minor Radius	$\bar{a} = 0.20m$
Magnetic Field on Axis	$B_o = 1.0Tesla(ECRH)$ $= 2.0Tesla(Max.)$
l Number	$l = 2$
Poloidal Rotation Number	$m = 19$
Inverse Winding Pitch	$\alpha = 4.3182m^{-1}$
Plasma Density(typ.)	$\bar{n}_e = 5.0 \times 10^{18}m^{-3}$
Plasma Temperature(typ.)	$\bar{T}_e = 500eV$
ECRH Frequency	$f = 28GHz$
ECRH Power	$P = 200kW$
ECRH Pulse Length	$t_{pulse} = 10msec(40msec \text{ max.})$

Table 6.2
Heliotron E Model Parameters

Axial Magnetic Field	$B_o = 1Tesla$
$l = 2$ Helical Magnetic Field	$B_{h2} = 0.32Tesla$
$l = 4$ Helical Magnetic Field	$B_{h4} = -0.0112Tesla$
Inverse Winding Pitch	$\alpha = 4.3182m^{-1}$
Separatrix Radius	$r_s = 0.3026m$
Peak Density	$n_{eo} = 7.50 \times 10^{18}m^{-3}$
Density Profile Factor	$m_n = 0.5$
Peak Temperature	$T_{eo} = 500eV$
Temperature Profile Factor	$m_T = 0.5$

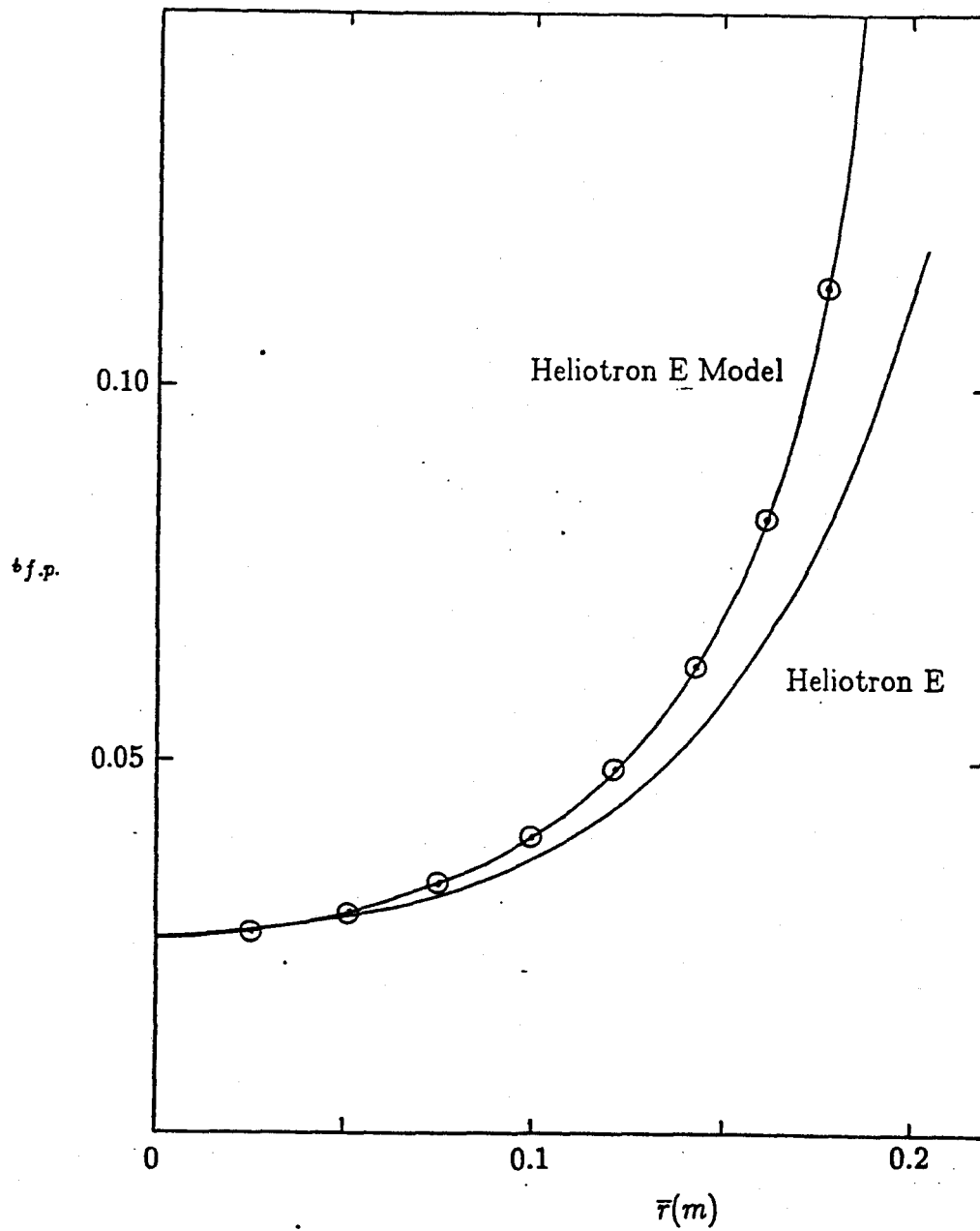
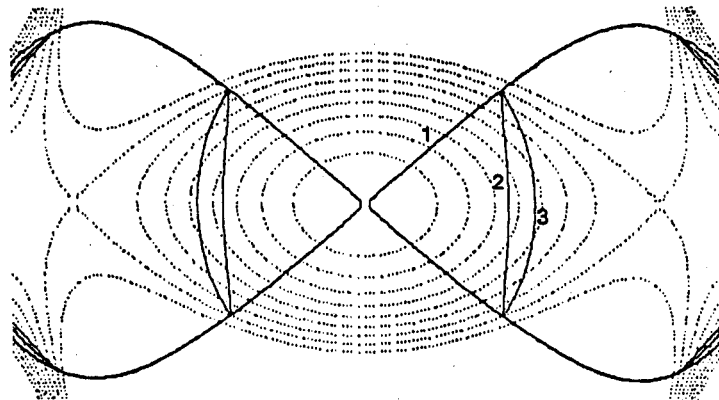


Figure 6.1 Heliotron E Rotational Transform ($t_{f.p.}$)

6.4 Wendelstein VII A

Wendelstein VII A is an $l = 2$ classical stellarator at Garching, operating since 1976. Modeling of this device is motivated by the ECRH experiment planned in the near future. Its machine specifications, typical plasma parameters for



- 1 - Cyclotron Resonance Layer
- 2 - Upper-Hybrid Resonance Layer
- 3 - Right Cut-Off Layer

Figure 6.2 Heliotron E Model Poloidal Cross-Section

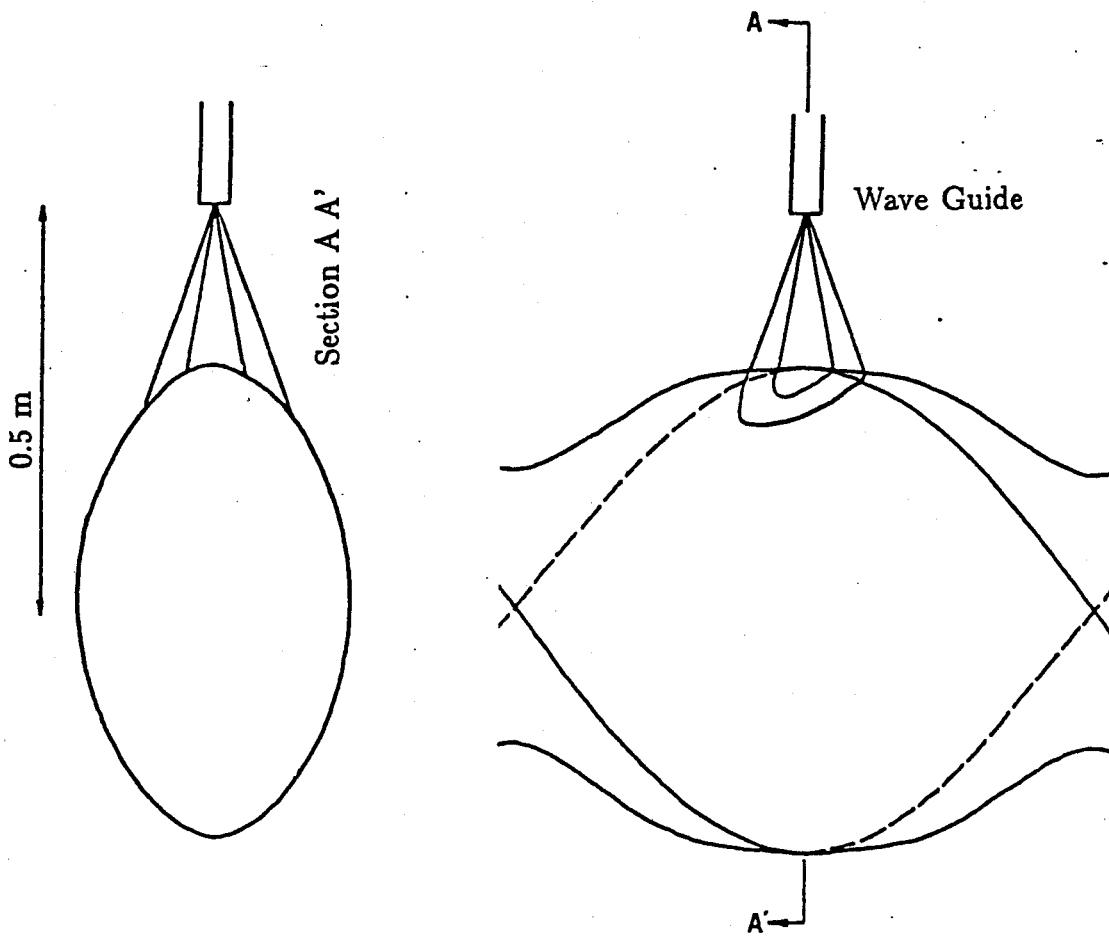


Figure 6.3 Heliotron E Launching Geometry

low field OH discharges, and projected ECRH specifications are listed in Table 6.3[32-34]. The field period(2.5m) is longer than the major radius(2m), so that the straight stellarator approximation is questionable over a field period. However, the large aspect ratio of 20 compensates for this point since the region of immediate concern for perpendicular injection of RF waves is the injection point plus or minus a distance on the order of the minor radius in the toroidal direction.

MAC was applied to come up with a self-consistent model for the projected ECRH experiment parameters, i.e., toroidal field of 1Tesla and plasma parameters, deflated from the 2.5Tesla values to keep $\beta \equiv \frac{2\mu_0 n k T}{B^2}$ constant. The task was complicated by the fact that Wendelstein VII A uses a molybdenum limiter of 13cm radius to define the plasma edge and the last flux surface[35]. Therefore, the default method of defining the separatrix surface to be the plasma edge is not applicable. Hence, a mathematical "limiter," which sets the density and the temperature to 0 on the flux surface whose maximum radius is 13cm, was introduced in MAC. Helical fields, B_{h2} and B_{h4} , were varied until the average minor radius of the plasma edge, i.e., the aforementioned flux surface, approached 10cm and the rotational transform on axis fell within the range noted in Table 6.3. The limiter option was necessary also from the point of view of matching the transform profile. Since, by definition, $t_{f.p.}$ equals $\frac{1}{2}$ at the separatrix surface for the straight model, nearly constant profile cannot be obtained if the entire region up to the separatrix is considered.

Resulting model parameters are shown in Table 6.4. The rotational transform profile, which is essentially flat, is shown in Figure 6.4; and the cross-section with resonance layers, in Figure 6.5. Of particular note, Figure 6.5(cross-section) shows the upper-hybrid and right cut-off layers to be very close to each other as well as to the plasma edge, which is expected to inhibit the propagation of X-waves from the low field side.

Compared to the Heliotron E model, there are several differences in the magnetic geometry of the Wendelstein VII A model. They are:

- (1) the plasma boundary specified by the limiter makes for more circular

flux surfaces;

- (2) since the rotational transform is nearly constant, the field is almost shearless;
- (3) shearless field in a straight geometry implies small value of $\nabla | \underline{B} |$ over the cross-section.

As an indication of (3), the lowest and the highest fields in the Wendelstein VII A model plasma are 0.99 *Tesla* and 1.01 *Tesla*, respectively, while those of the Heliotron E model plasma are 0.66 *Tesla* and 1.16 *Tesla*.

6.5 $l = 3$ Stellarator

Both Heliotron E and Wendelstein VII A are $l = 2$ machines that have general flux surfaces of the kind depicted in Figure 2.3. For the third machine to be simulated, an $l = 3$ stellarator is considered, with machine and plasma parameters in a range similar to the two preceding cases.

The purpose of this exercise is to check the advantages, if any, of a multi-cyclotron layered plasma. In an $l = 2$ stellarator, there are four cyclotron layers stemming from the plasma center, whereas in an $l = 3$ stellarator, there are six of them. Therefore, the ray is more likely to encounter two, if not more cyclotron layers in the latter device. To actually model this "fictitious" machine, no strict reference numbers existed, except that the values fall within the range of a present day experimental device. Specifically, the axial magnetic field was set at 1*Tesla* as in the other two devices, and the helical field value was varied until the separatrix radius fell between those of Heliotron E and Wendelstein VII A.

The model parameters are shown in Table 6.5, and relevant parts of the output from MAC are shown in Figures 6.6(rotational transform profile) and 6.7(poloidal cross-section).

Table 6.3
Wendelstein VII A Parameters

Major Radius	$R = 2.0m$
Average Minor Radius	$\bar{a} = 0.1m$
Magnetic Field on Axis	$B_o = 3.5Tesla(Max.)$ $= 1.0Tesla(ECRH)$
l Number	$l = 2$
Poloidal Rotation Number	$m = 5$
Inverse Winding Pitch	$\alpha = 1.25m^{-1}$
Rotational Transform on Axis	$t_o = 0.055 - 0.23$
Plasma Density(2.5T Ohmic Discharge)	$\bar{n}_e = 5.0 - 60.0 \times 10^{18}m^{-3}$
Plasma Temperature(2.5T Ohmic Discharge)	$\bar{T}_e = 200 - 900eV$
ECRH Frequency	$f = 28GHz$
ECRH Power	$P = 200kW$
ECRH Pulse Length	$t_{pulse} = 40ms(max.)$

Table 6.4
Wendelstein VII A Model Parameters

Axial Magnetic Field	$B_o = 1.0Tesla$
$l = 2$ Helical Magnetic Field	$B_{h2} = 0.36Tesla$
$l = 4$ Helical Magnetic Field	$B_{h4} = 0.06Tesla$
Inverse Winding Pitch	$\alpha = 1.25m^{-1}$
Limiter Radius	$r_l = 0.13m$
Average Minor Radius	$\bar{a} = 0.106m$
Peak Density	$n_{co} = 6.0 \times 10^{18}m^{-3}$
Density Profile Factor	$m_n = 0.5$
Peak Temperature	$T_{co} = 300eV$
Temperature Profile Factor	$m_T = 0.5$

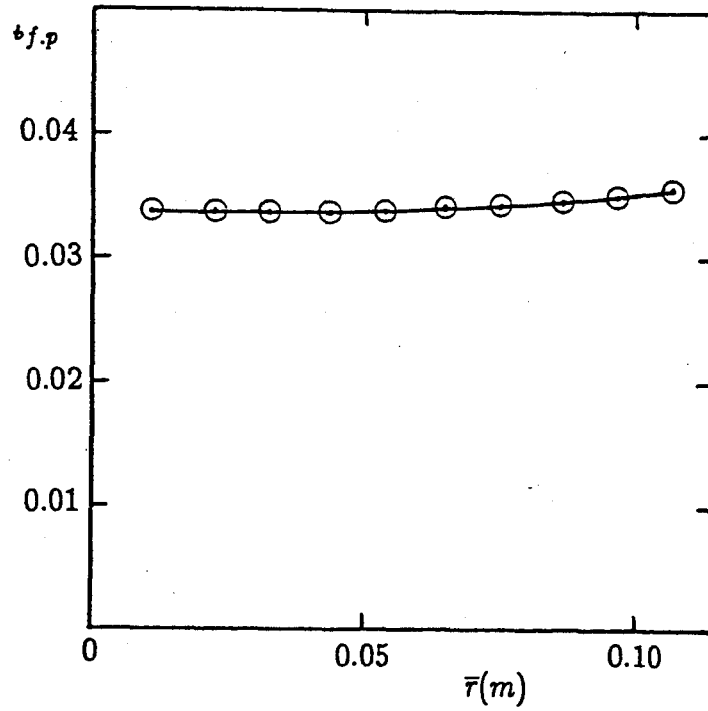
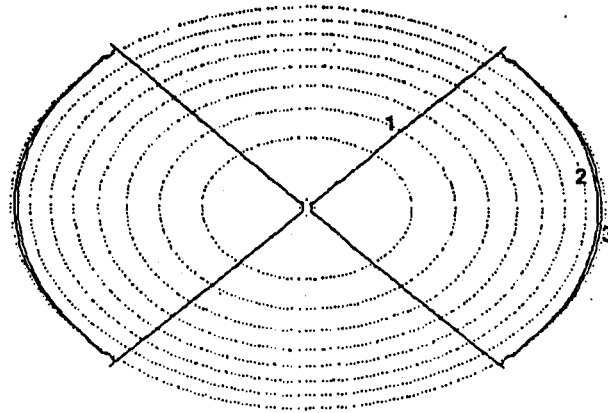


Figure 6.4 Wendelstein VII A Rotational Transform



- 1 - Cyclotron Resonance Layer
- 2 - Upper-Hybrid Resonance Layer
- 3 - Right Cut-Off Layer

Figure 6.5 Wendelstein VII A Model Poloidal Cross-Section

Table 6.5

 $l = 3$ Stellarator Model Parameters

Axial Magnetic Field	$B_o = 1\text{Tesla}$
$l = 3$ Helical Magnetic Field	$B_{h3} = 0.25\text{Tesla}$
Inverse Winding Pitch	$\alpha = 5.0\text{m}^{-1}$
Separatrix Radius	$r_s = 0.176\text{m}$
Peak Density	$n_{eo} = 8.0 \times 10^{18}\text{m}^{-3}$
Density Profile Factor	$m_n = 0.5$
Peak Temperature	$T_{eo} = 500\text{eV}$
Temperature Profile Factor	$m_T = 0.5$

6.6 Summary

Criteria for modeling of an actual device by the straight stellarator model were defined. They consisted of magnetic field criteria and plasma criteria, where former defined the machine dimensions and the latter were given typical values.

Three stellarator models were defined, based on the criteria defined previously. Two came from existing machines, Heliotron E and Wendelstein VII A. Heliotron E already has an ECRH on line, while Wendelstein VII A plans to have ECRH on line in the near future as well. In addition, these two machines are contrasted by the fact that Heliotron E has high shear, and Wendelstein VII A is shearless. Effects of shear on the wave propagation, if any, are hoped to emerge from comparison. For the third model, a fictitious $l = 3$ stellarator was chosen. The purpose of this selection is to compare the $l = 2$ and $l = 3$ systems and to see, from ECRH point of view, which is desirable.

In the following chapters, the three models will casually be referred to as "Heliotron E," "Wendelstein VII A," and " $l = 3$ Stellarator," with the understanding that the *models* of these machines are implied.

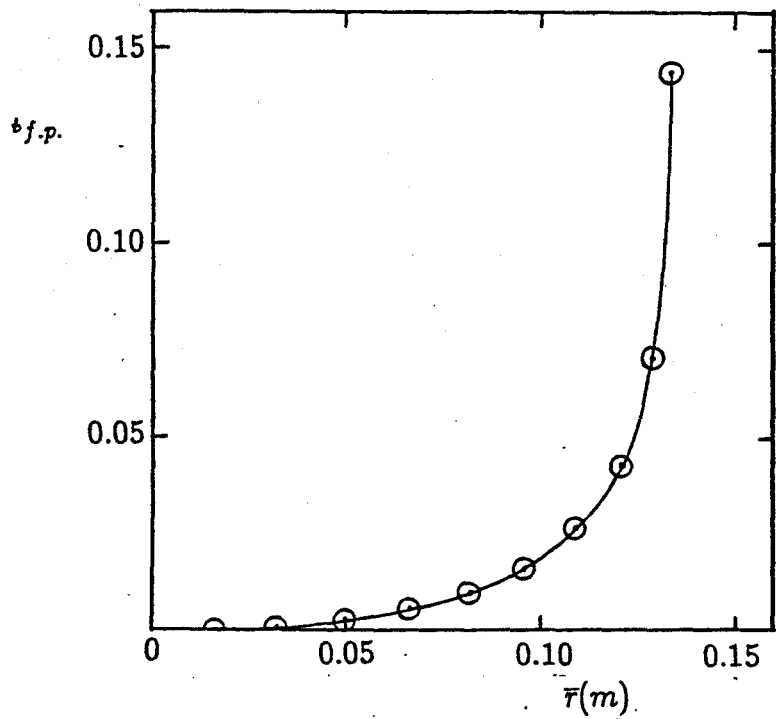


Figure 6.6 $l = 3$ Stellarator Rotational Transform

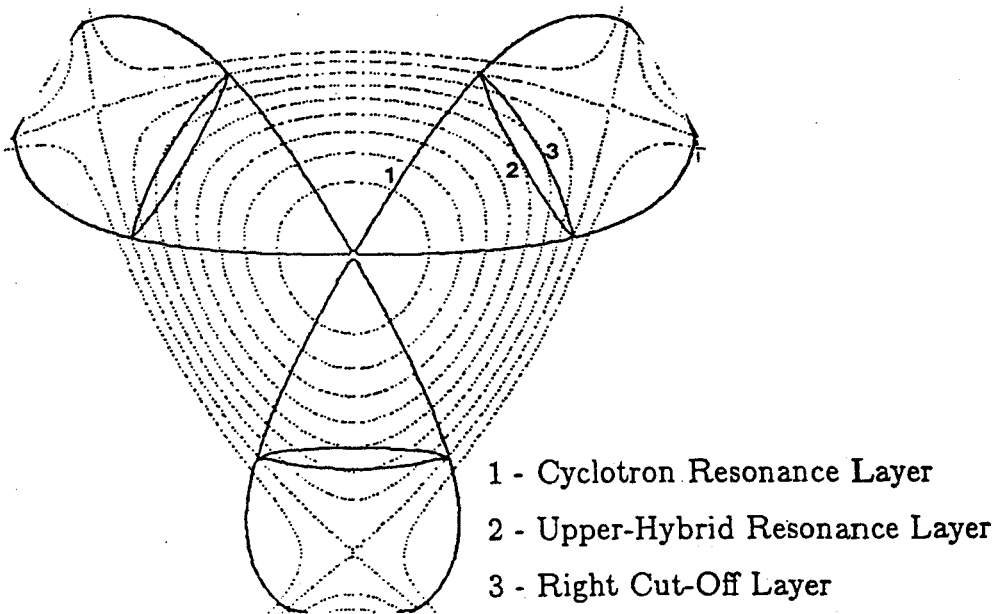


Figure 6.7 $l = 3$ Stellarator Model Poloidal Cross-Section

Chapter 7

Simulation Results

7.1 Introduction

For the three model stellarators defined in the previous chapter, systematic simulation schedule was set up and executed. The basic questions that were addressed in the simulation are the following:

- (1) dependence of accessibility and power absorption on the launching position and direction;
- (2) simulation of the existing launching geometry in Heliotron E.
- (3) dependence of accessibility and power absorption on the shape and position of the resonance layers;
- (4) dependence of ray trajectories on helical effects, isolated from density and temperature effects;
- (5) simulation of a start-up with ECRH;

Simulation items (2) through (5) were carried out only on Heliotron E. The reasons for doing this are twofold. First, there is the trade-off between the amount of work on the computer and the additional information to be gained by it. The conclusion reached after the initial set of simulation and analysis was that further analyses are required before additional computation in order to utilize effectively the computer time. Second, three models were chosen not

to do exhaustive study of each, but to complement one another. To this end, most of the basic stellarator simulation to be compared with other types of devices are done on Heliotron E, and Wendelstein VII A is used to investigate the difference in propagation, if any, in a shearless plasma. As pointed out in Chapter 6, the $l = 3$ stellarator was chosen specifically to investigate the effect of the difference in l numbers.

Section 7.2 states the general results of the simulation in terms of the results that apply to stellarators in general, and results pertaining to specific models. In Section 7.3, simple models are presented to consider the effects of toroidicity on the simulation results. Section 7.4 compares the results with experimental results in Heliotron E. Section 7.5 gives a qualitative discussion on the difference in ECRF propagation for stellarators, tokamaks, and mirrors. In Section 7.6, an attempt is made to come up with a consistent set of guidelines for ECRH experiments in stellarators. Section 7.7 summarizes this chapter.

7.2 General Results

7.2.1 Simulation Figures

Four part figures, such as Figure 7.2, are an important part of the analyses, and since there are quite a number of them, how to read these is explained here. The upper-left figure shows the ray trajectories (solid lines) plotted in the $r - \phi$ plane. Flux surfaces are shown in dotted lines, and the last closed flux surface defines the plasma boundary. Note that the rays are always launched from the right, and that it starts somewhat inside the edge to avoid numerical instabilities. Electron cyclotron layer is also superimposed on this plot in solid lines. The upper-right figure shows the ray trajectories plotted in the $r - \theta$ plane, which is the stationary plane. Axes show x and y directions for the purpose of orientation, and the distance is given in centimeters. The lower-left figure shows the ray trajectories plotted in the $z - r(\theta = 0)$ plane. Here again, distances are given in centimeters; the vertical axis corresponds

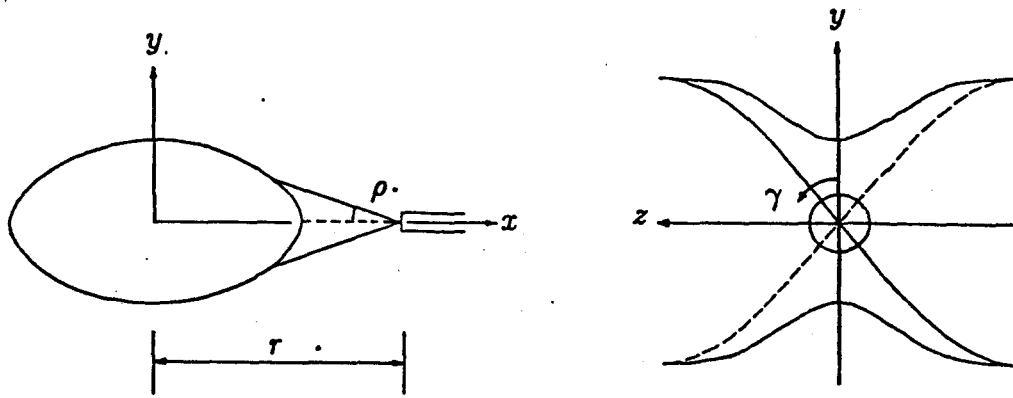


Figure 7.1 Simulation Geometry

to the z -direction and the horizontal axis to the r -direction. The rays are numbered in at least one of the three figures, usually the one which most clearly distinguishes between adjacent rays. These numbers are used in identifying the power absorption rate given in the lower-right bar graph. Here, the vertical axis is the power absorption rate in %, and the horizontal axis is the ray numbers and the launching direction, γ (to be explained next). Stacked bars marked "2" and "3" refer to the fraction of power absorbed in the second or the third pass through a resonance.

All the data in this chapter were produced using the launching option (4) of HERA (Chapter 5), i.e., a launching point outside the plasma and a direction of the wave vector were specified. The group of rays that are shown on a same figure have the same mode and the launching position. The direction of the rays are chosen such that they would form a half cone about the normal, which is the line that is in the $r - \theta$ plane, and connects the launching point and the plasma axis. In other words, rays on a same figure have the same cone half angle, ρ , but different azimuthal angles, γ (Figure 7.1). Distance from the machine axis to the launching position is denoted by r . Since the plasma, and therefore the ray trajectories have symmetry with respect to the origin shown in Figure 7.1, only the region $z > 0$ ($0 \leq \gamma < \pi$) was considered.

There are four combinations in which a wave can be launched from outside the plasma with respect to the magnetic field strength at the injection point

Table 7.1

Four Combinations of Modes and Injection Points

Case	Mode	Injection Point
I	Ordinary	Low Field Side
II	Extraordinary	Low Field Side
III	Ordinary	High Field Side
IV	Extraordinary	High Field Side

and the mode of the wave. These four combinations are listed in Table 7.1, and will be referred to as "Case I" etc.

7.2.2 Launching Position and Mode Scan in Heliotron E

In Figures 7.2 through 7.6, the basic results, namely, the ray trajectories and the power absorption rates are given for the four cases in Heliotron E. In the low field side launches, the launching point was taken to be the waveguide throat of the actual launching geometry (Figure 6.3). For the high field side launches, same geometry was assumed, but with the launching point translated by $\frac{\pi}{2\alpha}$ in the z direction. Figures 7.2 and 7.3 both show Case I, but with different values of ρ , while Figures 7.4 through 7.6 show Cases II through IV.

In Figure 7.2 (Case I, $\rho = 5^\circ$), the average power absorption per ray is 28 %; in Figure 7.3 (Case I, $\rho = 10^\circ$), 16 %; in Figure 7.5 (Case III, $\rho = 5^\circ$), 69 %; and in Figure 7.6 (Case IV, $\rho = 5^\circ$), 16 %. No power absorption took place in Case II, as the rays were reflected out as it approached the right cut-off layer. It appears that the O-waves launched from the high field side is the most favorable case, since the total absorption rate is over a factor of 2 larger than the other cases.

These results are consistent with the accepted theory of ECRF propagation and absorption discussed in Chapter 3, namely that the absorption peaks at $\theta = 0$ for O-waves and at $\theta = \frac{\pi}{2}$ for X-waves. Since these rays are injected

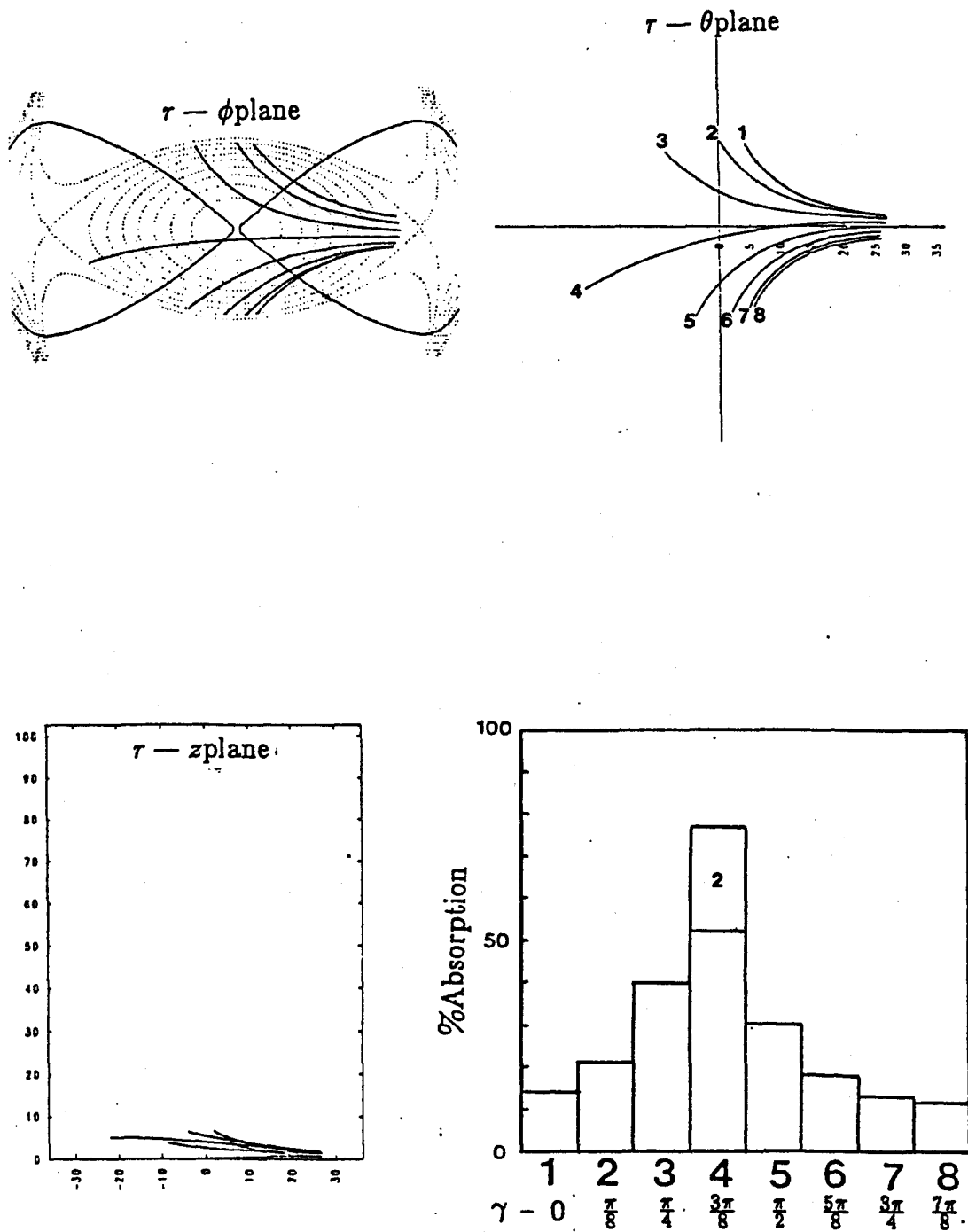


Figure 7.2 Trajectories of O-Waves Launched from the Low Field Side in Heliotron $E(\rho = 5^\circ, r = 0.50m)$

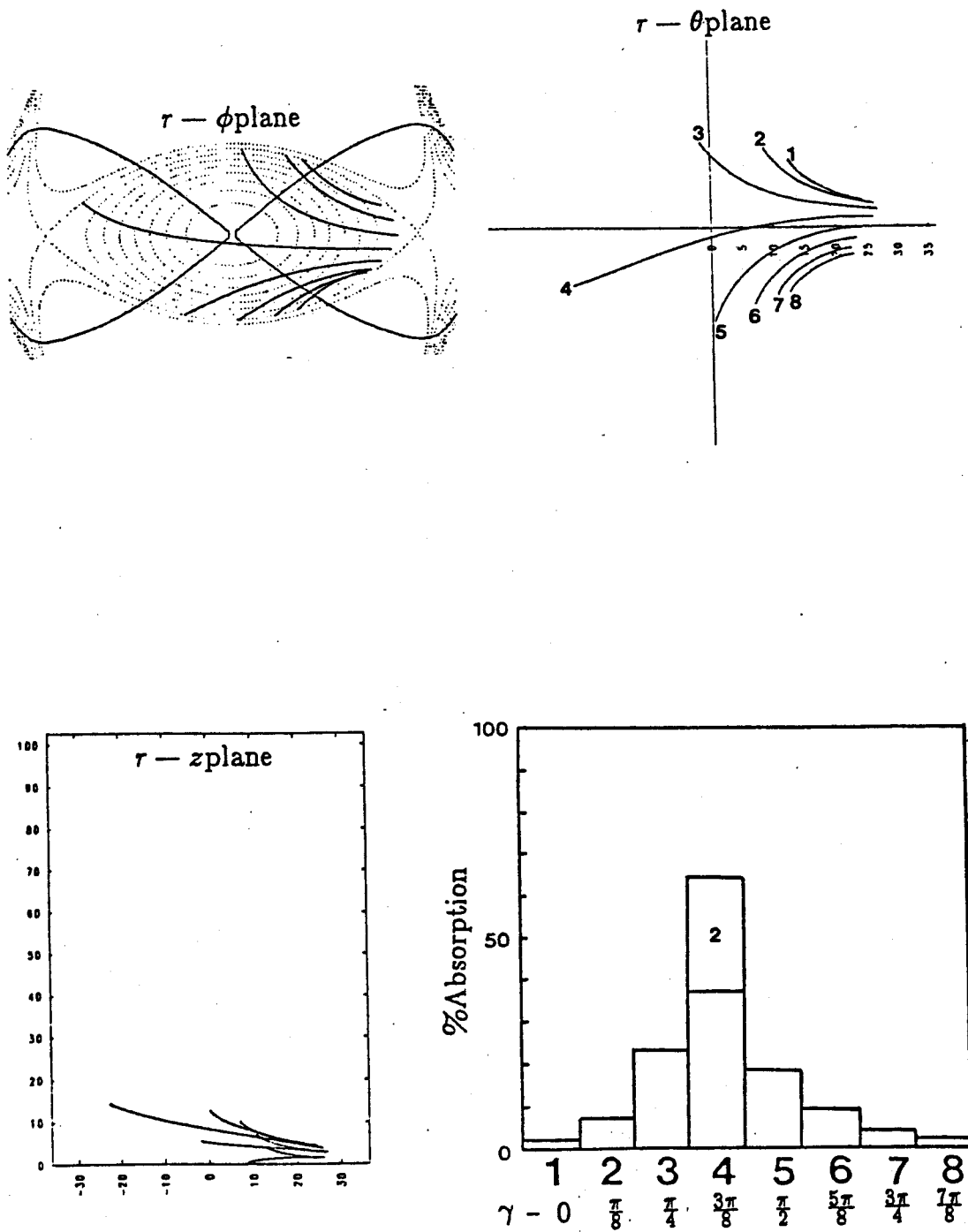


Figure 7.3 Trajectories of O-Waves Launched from the Low Field Side in Heliotron $E(\rho = 10^\circ, r = 0.50m)$

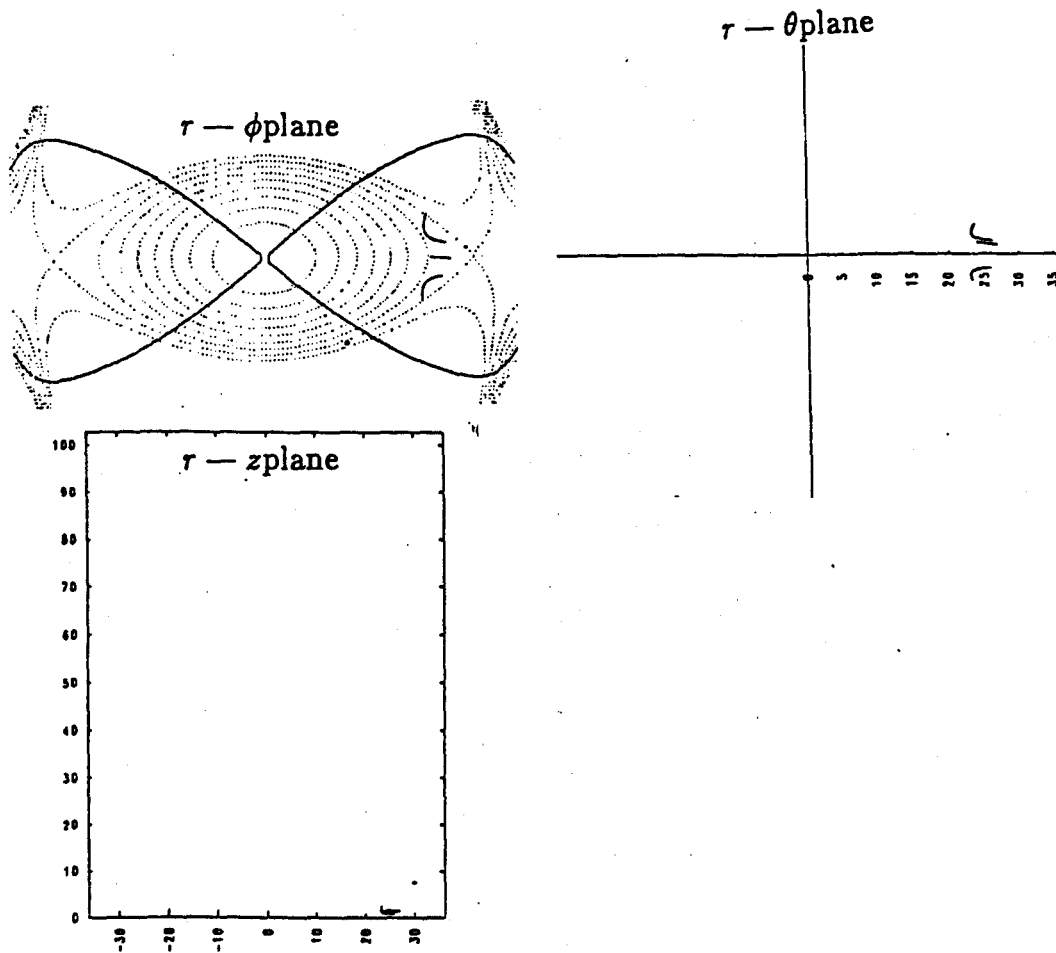


Figure 7.4 Trajectories of X-Waves Launched from the Low Field Side in Heliotron E

almost perpendicular to the field lines, O-waves, as expected, experience more absorption. The dependencies of absorption on the density and temperature are responsible for the center-peaked absorption profiles.

Unlike the markedly different behaviors of the two modes launched from the low field side, the trajectories of O- and X-waves launched from the high field side (Figures 7.5 and 7.6) look similar due to the absence of the right-hand cut-off layer, and the injection angle which avoids the upper-hybrid resonance layer altogether. The difference in the trajectories of these two groups of rays is due to the fact that the O-waves see the plasma cut-off approaching as they climb up the density gradient, and tend to diverge from the center, while

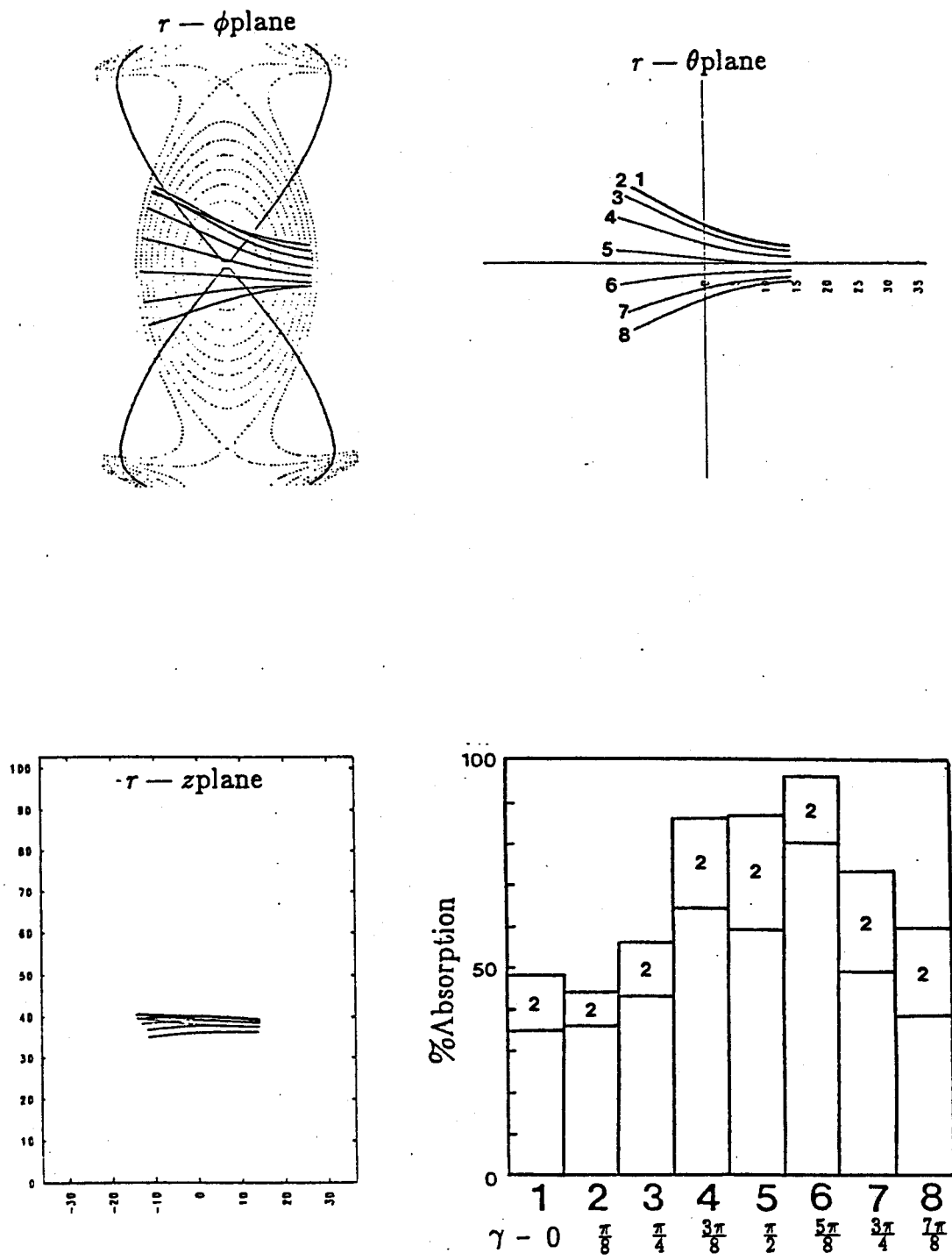


Figure 7.5 Trajectories of O-Waves Launched from the High Field Side in Heliotron E ($\rho = 5^\circ$, $r = 0.50m$)

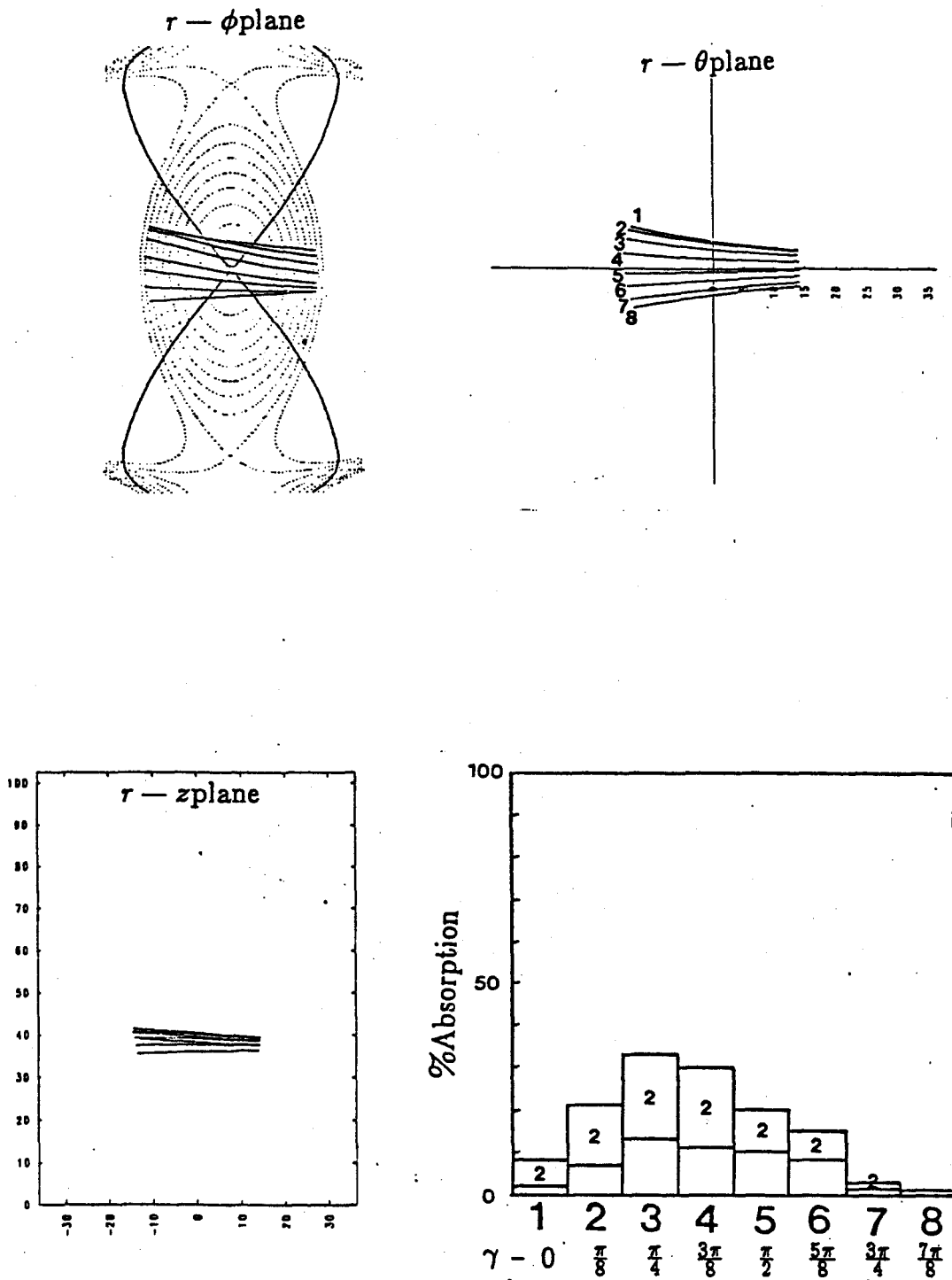


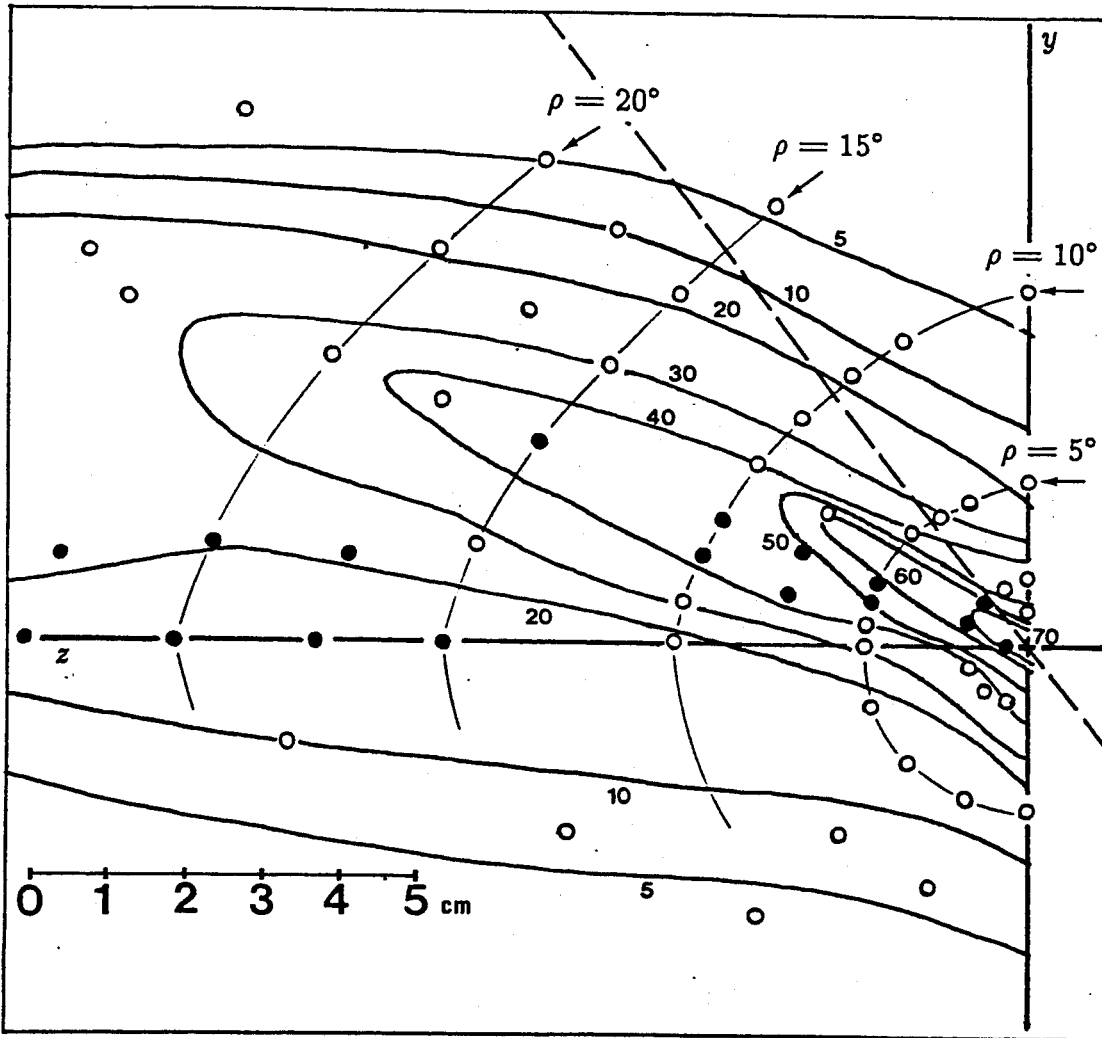
Figure 7.6 Trajectories of X-Waves Launched from the High Field Side in Heliotron $E(\rho = 5^\circ, r = 0.50m)$

X-waves do not. This difference in the ray curvature is apparent if $r - \theta$ plane plots are examined: in Figure 7.5 $r - \theta$ plane plot, the rays are markedly curved, while in the same plot in Figure 7.6, they are nearly straight lines.

Comparison of the O-waves launched from different sides leads to the following observation. Examining the $r - \theta$ plane plots, it is found that the rays are more curved in the case of the low field side launch(Figure 7.2) than the high field side launch(Figure 7.5). This is due to the fact that the angle between the density gradient vector and the wave vector is larger for Case I than for case III, thus introducing more correction to the direction for the former than for the latter. The total curvature experienced by the ray is also smaller for Case III since the distance from the edge to the center is short compared to that for Case I. The consequence of these is that the waves launched from the high field side deposit more of its energy in the central region, which is a favorable process.

The low field side launch of the O-waves was pursued further, and upwards of sixty rays were launched. The resulting power absorption is plotted in Figure 7.7, which shows the projection of the Heliotron E plasma surface on a $y - z$ plane, where y is taken to be upward and z is the toroidal direction. Circles indicate points at which rays, radiated from the throat of the wave guide(Figure 6.3), enter the plasma. The solid lines are the contours of constant power absorption. In another words, the power absorption of a ray is related to the injection point of that ray. The contours of constant power absorption are similar in shape to elongated ellipses, with its long axis at an angle little more than a half way between the horizontal and the saddle point line.

The shape and orientation of the contours can be explained as follows. As the rays carry more k_z component, it will spend more and more time in the resonance layer because of its large k_{\parallel} , thereby increasing absorption. This is why the contours are peaked in the horizontal direction. If a ray enters the plasma above the saddle point line in Figure 7.7, the density gradient bends the ray outwards in the absolute frame as the ray propagates inward and in the positive z direction; and the rotation of the plasma also bends the ray outwards



- — Single Pass Ray Injection Point
- — Double Pass Ray Injection Point
- — Saddle-Point Line

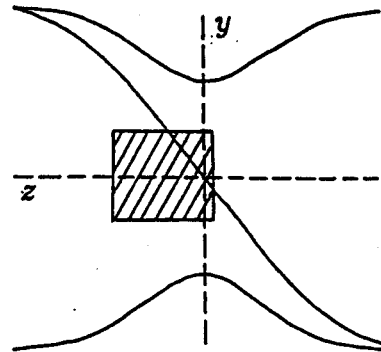


Figure 7.7 O-Wave Power Absorption Contour in Heliotron E

in the $r - \phi$ frame. Hence, rays that enter the plasma above the separatrix with finite k_z will spend a short time inside the plasma and experience little absorption.

When a ray enters the plasma below the saddle point line in the same figure, the density gradient tends to bend it outward, but the rotation of the plasma flux surface tends to bend it inward in $r - \phi$ space. These two mechanisms compete, and for appropriate combinations, the ray will pass close to the center of the plasma, resulting in high absorption rate. Ray Number 2 in Figure 7.2 corresponds to a ray injected above the saddle point, and ray Number 4 in the same figure corresponds to a ray injected below the saddle point, experiencing high absorption.

Another feature indicated on this figure is the distribution of regions where the injected ray passes through the cyclotron resonance twice, once on the near side and once on the far side. Note that there are two separate regions in which this phenomenon occurs, one close to the launching axis, and another further down in the z direction.

A typical ray in the first region is depicted in Figure 7.8 as Ray 1. It goes in near the saddle point, aimed directly at the center. Since it has a very small k_z component, the $r - \phi$ plane plot and the $r - \theta$ plane plot are essentially the same. The result is a nearly straight ray over the greater part of the trajectory, passing through two resonance layers close to the center. Typical rays in the second region in Figure 7.7 are depicted in Figure 7.8 as Rays 2 and 3. For Ray 2, the $r - \phi$ plane plot gives nearly a straight line parallel to a line connecting the two saddle points, while the same ray plotted in the $r - \theta$ plane shows a heavily curved trajectory in fixed space. This is because the injection angle of the ray was such that the curvature of the ray due to the density gradient was exactly "matched" to the rotation of the flux surface. Hence, this second two pass region is a result of the helical geometry effect. The rotation of the plasma will eventually overtake the ray as it is given more k_z component so that finally, a ray entering from the 4th quadrant will cut across the center and come out in the 2nd quadrant in the $r - \phi$ plane plot (Ray 3). If this were

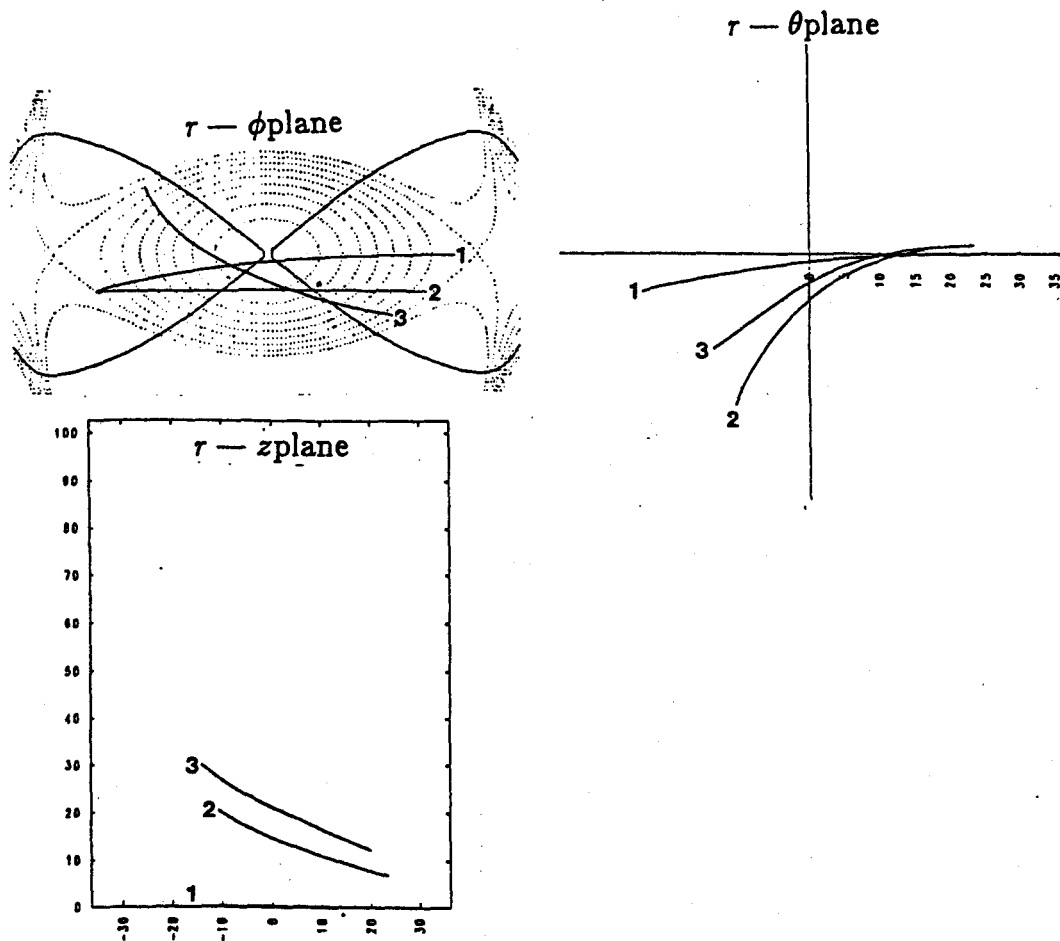


Figure 7.8 Three Types of Two Pass Rays in Heliotron E

to go on for larger values of k_z , a ray could be seen just circulating inside the plasma until it loses all its energy. However, this cannot be expected to go on indefinitely in actual stellarators due to the toroidal curvature.

7.2.3 Frequency Detuning in Heliotron E

Effect of the frequency on the heating profile was also investigated. This was done by shifting the frequency while holding the machine parameters constant. This scenario results in changing the shape and the position of the resonance layers. The five $r - \phi$ plane plots for cases in which the frequency was shifted by a maximum of $\pm 10\%$ are shown in Figure 7.9. As it can be seen, lowering

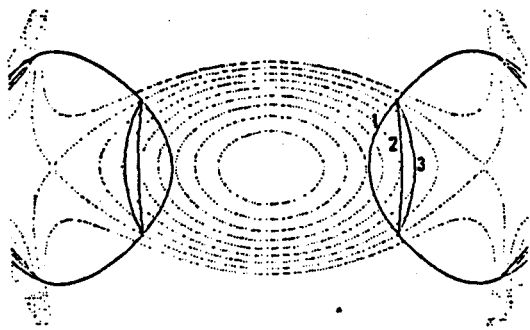
the frequency brings the resonance layers to the low field side, and tend to place all three layers close together due to the large density gradient. Increasing the frequency brings the cyclotron layers to the high field side, and the other two layers (upper-hybrid and right cut-off) to the center of the plasma. In either case, the cyclotron layer is pushed out from the central region, which should result in a decrease in the absorption rate since power absorption is proportional to temperature.

To see what the heating profiles look like for the five cases, O-waves were launched from the low field side with a 5° cone half angle. Resulting heating profiles are shown in Figure 7.10. Ray trajectories, not shown here, are all similar to Figure 7.2, although the plasma cut off effect will tend to bend the rays more for $\omega < \omega_{ce}(0)$ and less for $\omega > \omega_{ce}(0)$, where $\omega_{ce}(0)$ is the cyclotron frequency corresponding to the magnetic field on axis. Convention of the bar graphs are similar to those in other figures, except for the horizontal axis which is marked in terms of the azimuthal angle, γ , of the launch cone only. For $\omega = 0.90\omega_{ce}(0)$, the average power absorption is 10 %; for $\omega = 0.95\omega_{ce}(0)$, 15 %; for $\omega = \omega_{ce}(0)$, 28 %; for $\omega = 1.05\omega_{ce}(0)$, 20 %; and for $\omega = 1.10\omega_{ce}(0)$, 8 %.

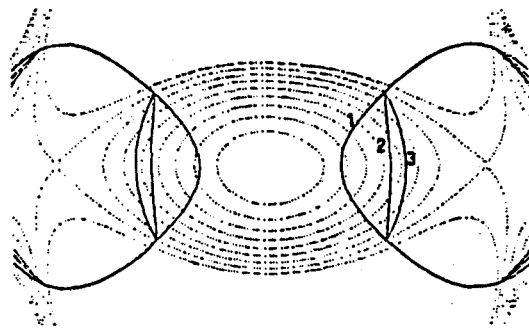
The trend is clear and can be summarized as follows: as the frequency is decreased, the density variation on the cyclotron layer becomes smaller making the absorption rate uniform; as the frequency is increased, more and more rays launched towards the mid plane see no resonance at all thereby creating a big gap in the absorption profile as seen in Figure 7.10, graphs d and e. Opposite scenario is true for rays launched from the high field side, i.e., more uniform absorption rate for an increase in frequency, and an absorption gap in the center for a decrease in frequency.

7.2.4 Helical Effects

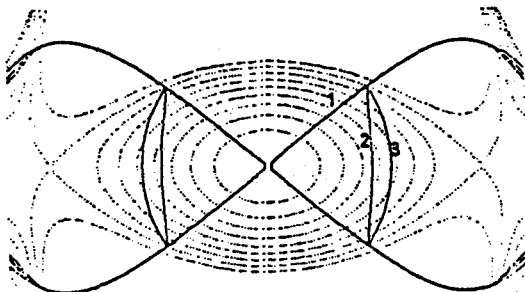
So far, cases have been run using the magnetic fields and plasma profiles defined in Chapter 2. It was seen that the density gradient is responsible for the ray curvature, and the heating profiles could also be attributed to the values



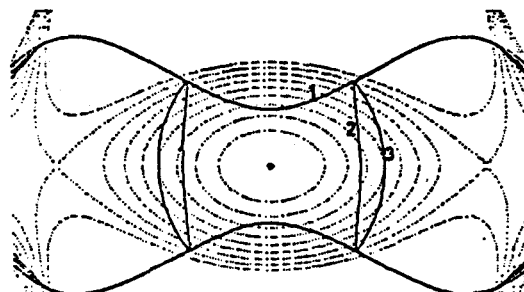
a. $\omega = 0.90\omega_{ce}(0)$



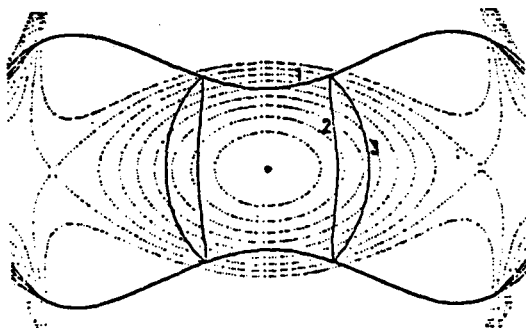
b. $\omega = 0.95\omega_{ce}(0)$



c. $\omega = 1.00\omega_{ce}(0)$



d. $\omega = 1.05\omega_{ce}(0)$



e. $\omega = 1.10\omega_{ce}(0)$

- 1 — Cyclotron Resonance Layer.
- 2 — Upper Hybrid Resonance Layer.
- 3 — Right Hand Cut-Off Layer.

Figure 7.9 Shift of Resonance Layers with Shift in Frequency in Heliotron E

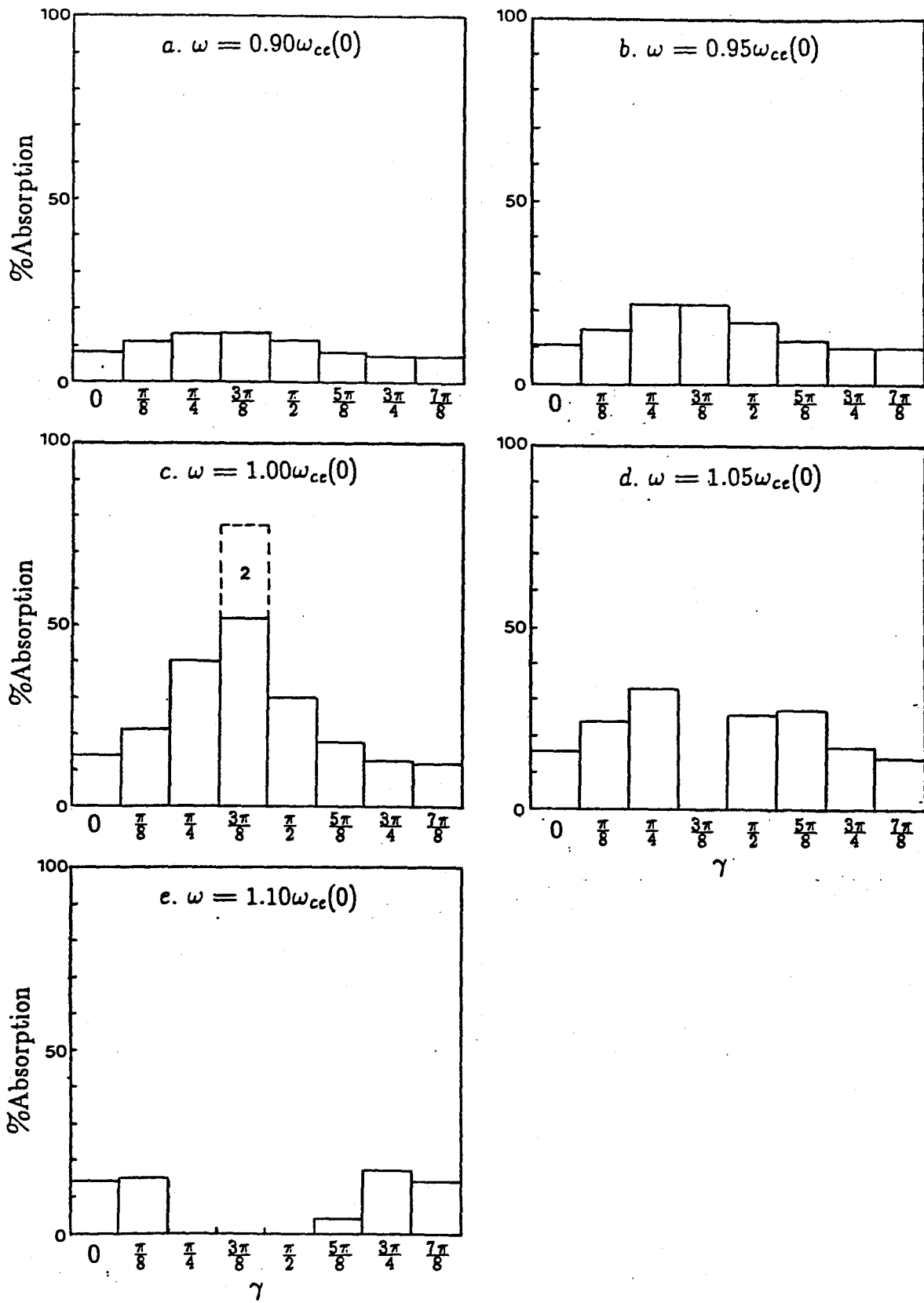


Figure 7.10 Power Absorption Profiles as a Function of Frequency in Heliotron E ($\rho = 5^\circ, r = 0.50m$)

of the density and the temperature in the resonance layers. Next the isolation of the effect of the helical geometry, i.e., the helicity (rotational transform) and the shear, was carried out. To accomplish this, the density and temperature profile factors, m_n and m_T were set to zero in Equations (2.16) and (2.17), so that a plasma with uniform temperature and density is given, i.e., Heliotron E model parameters of Table 6.2 were used but with $m_n = m_T = 0$. Case I with $\rho = 10^\circ$ for this plasma is shown in Figure 7.11, which should be compared with Figure 7.3.

First thing to note is that the rays are straight, as seen in the $r - \theta$ plane, which leads to the observation that the effect of helicity on the propagation is small. The slight bending of the rays outward in $r - \phi$ or the $r - z$ plane are due to the plasma cut-off effect, which increases with the magnitude of the parallel wave number even for a constant density [36].

Second, despite the fact that the plasma is uniform with constant density and temperature, the absorption in the center of the plasma is large compared to the outside. This is because the shear is smaller in the central region, which results in a longer magnetic field gradient scale length, L_B , which in turn results in a wider resonance layer. Thus the helical effect as seen in Heliotron E is responsible for enhancing the central absorption.

7.2.5 Start-Up

ECRH can be used in place of the ohmic discharge to break down and form the plasma [37-38]. This should be a very important consideration for reactors and larger experiments. With enough power in the ECRH, it is possible to bring the plasma from breakdown stage all the way up to ignition, a feat unachievable with ohmic drive. It was proposed at the beginning of this chapter to investigate the phenomenon of start-up in stellarators; where at low initial temperatures, most of the power absorption takes place at the upper-hybrid layer for the X-waves; and as the temperature increases, cyclotron resonance becomes the dominant absorption mechanism. However, presently available tools are not sufficient to carry out this work. Namely, the models for power absorption

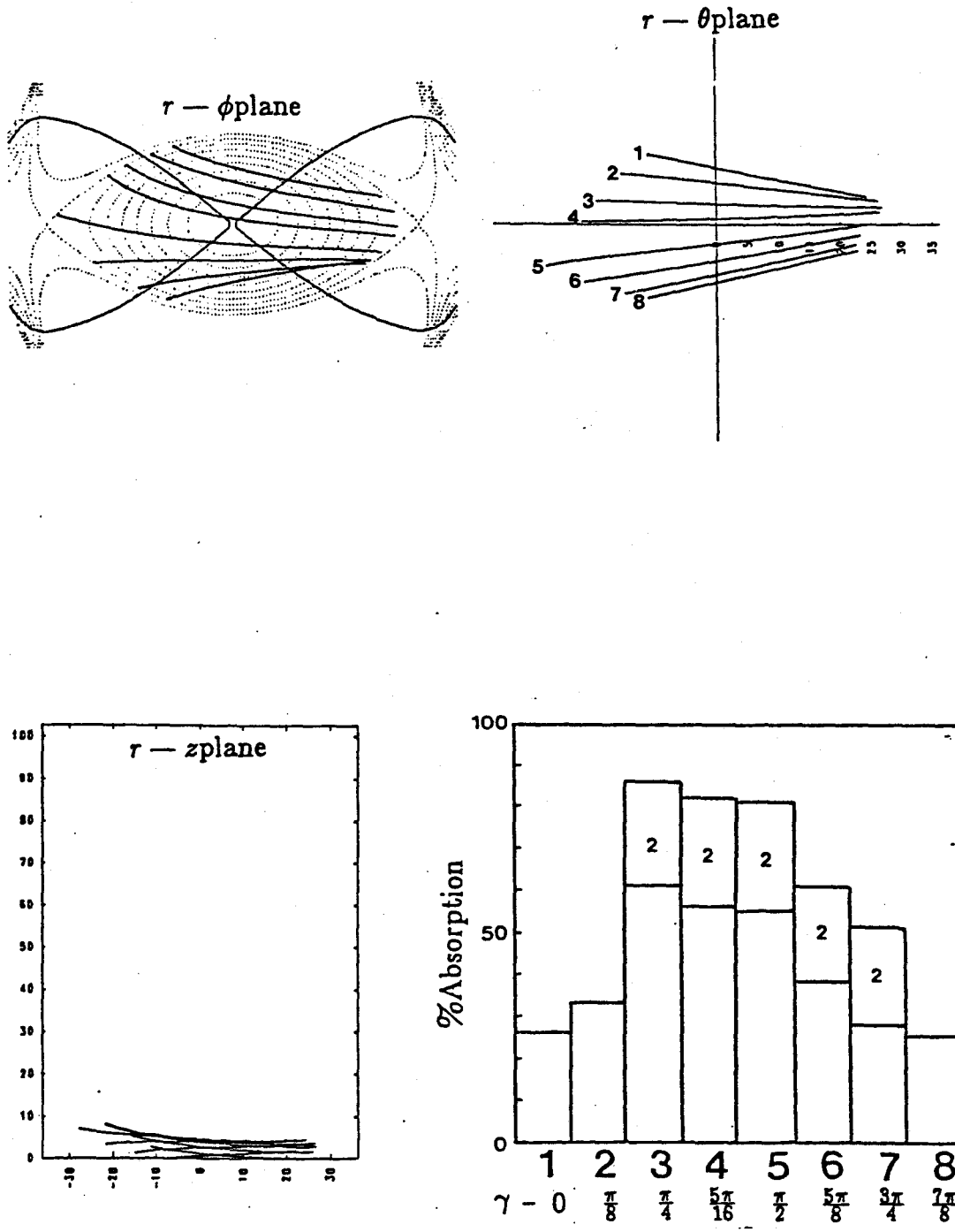


Figure 7.11 Effects of Helical Geometry on the Ray Trajectory in Heliotron E ($\rho = 10^\circ$, $r = 0.50m$)

at the upper-hybrid layer at low temperatures, and the mode conversion of X-waves to Bernstein waves at the upper-hybrid layer at higher temperatures, are missing.

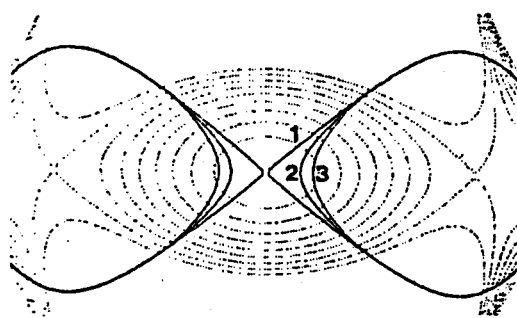
Here it will simply be shown how the resonance layers evolve with density, i.e., plasma formation. Figure 7.12 shows the resonance layer plots for Heliotron E with density varying from 0.5×10^{18} to $7.5 \times 10^{18} m^{-3}$. In the case of zero density, it should be noted that all three layers collapse to one, as can be seen outside the plasma.

Based on the temperature dependence of the processes at the cyclotron and the upper-hybrid layers, the following scenario can be considered. In the initial stage, most of the ionization is carried out in the center of the plasma, where both cyclotron and upper-hybrid layers are present (Figure 7.12 a and b), here nonlinear processes at the upper-hybrid layer is the dominant source of absorption at low temperatures, as discussed in Chapter 3. Then, as the density builds up, upper-hybrid and right cut-off layers are pushed outwards (Figure 7.12 d and e), the degree of this departure being greater for systems with small field gradient in the plasma. Finally, when the temperature is hot enough, practically all the power deposition takes place in the cyclotron layer, and upper-hybrid layer contributes only to the mode conversion of X-waves into plasma waves, which gets absorbed subsequently near the cyclotron layer.

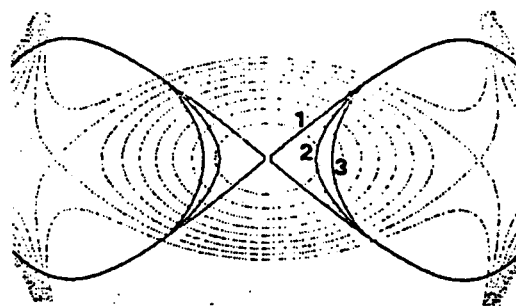
7.2.6 Wendelstein VII A

The simulation results of Wendelstein VII A are shown in Figures 7.13 through 7.15 for Cases I, III, and IV. Case II is absent here since the WKB approximation is not valid in the region between the plasma edge and the right cut-off for X-waves.

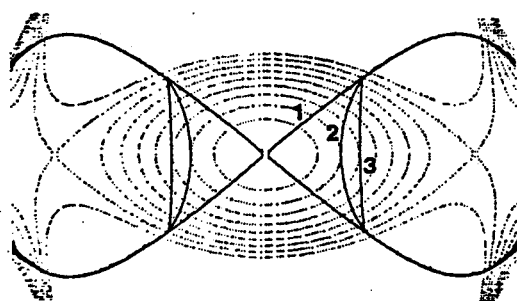
In Figure 7.13, O-waves launched from the low field side are shown. Here, in the case of $\rho = 5^\circ$, the absorption is almost complete, averaging 99 % per ray. O-waves and X-waves are launched with $\rho = 10^\circ$ from the high field side (Figures 7.14 and 7.15) and here again, absorption is significant (86 % and 60 %, respectively). In addition, the high field side trajectories of O- and



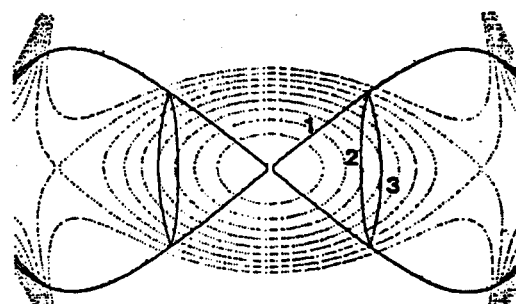
a. $n_{e0} = 0.50 \times 10^{18} m^{-3}$



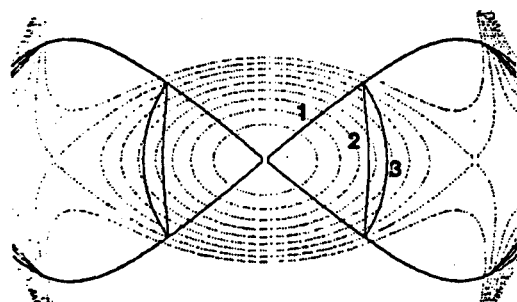
b. $n_{e0} = 1.00 \times 10^{18} m^{-3}$



c. $n_{e0} = 3.00 \times 10^{18} m^{-3}$



d. $n_{e0} = 5.00 \times 10^{18} m^{-3}$



e. $n_{e0} = 7.50 \times 10^{18} m^{-3}$

$m_n = 0.5$

- 1 — Cyclotron Resonance Layer
- 2 — Upper Hybrid Resonance Layer
- 3 — Right Hand Cut-Off Layer

Figure 7.12 Evolution of Resonance Layers with Plasma Formation in Heliotron E

X-waves are more similar than the two waves for Heliotron E, due to the low peak density which contributes to the decrease in the plasma cut-off effect.

In Wendelstein VII A, the absorption is higher than in Heliotron E despite the former's smaller cross section. Comparison of the typical damping and magnetic field profiles for the two devices are given in Figures 7.16 and 7.17. Figure 7.16 shows the plot of $\text{Im}(k)$ vs. time, while 7.17 shows the plot of B vs. time. The two rays are for Case IV and they correspond to Ray 8 in Figure 7.6 and Ray 5 in Figure 7.15, respectively. Note that the vertical scale differs from plot to plot. Also note that the total time that the ray spends inside the plasma is approximately equal. The difference in the magnitude of $\text{Im}(k)$, which is about 10, can be accounted for if the difference in the magnitude of k_{\parallel} (which is 3) and the difference in $\frac{\omega_{pe}^2}{\omega^2}$ (which is 1.1) is taken into account in Equation (3.37). Namely,

$$\text{Im}(k) \approx Q_{X1} = N_{\parallel}^2 \frac{(1 + \frac{\omega_{pe}^2}{\omega^2})^2 (2 - \frac{\omega_{pe}^2}{\omega^2})^{\frac{1}{2}}}{4 \frac{\omega_{pe}^2}{\omega^2}}. \quad (7.1)$$

For Heliotron E, $\frac{\omega_{pe}^2}{\omega^2} = 0.77$ and $N_{\parallel}^2 = 0.018$; and for Wendelstein VII A, $\frac{\omega_{pe}^2}{\omega^2} = 0.83$ and $N_{\parallel}^2 = 0.057$. Using these values in Equation (7.1) gives $Q_{X1} = 0.0056$ for Heliotron E, and $Q_{X1} = 0.062$ for Wendelstein VII A; and the ratio of the two is about 11, approximately equal to the factor of 10 as seen in the figures. The differences in the magnitude of $\text{Im}(k)$ for the two devices for Cases I and III can be accounted for in a similar way using the expression for Q_{O1} (Equation (3.36)). It is reminded here that these differences in $\text{Im}(k)$ are not particular properties of the devices themselves, but of the selected launching angles and the plasma parameters.

Even though a little diversion was made to account for the difference in the magnitudes of $\text{Im}(k)$ in the two cases, these figures illustrate a single point, which is the correlation between the field gradient and the width of the absorption. In Figure 7.16 b, the absorption is taking place over the entire time that the wave is propagating in the plasma because the magnitude of the magnetic field is close to the resonance value throughout (Figure 7.17 b). In

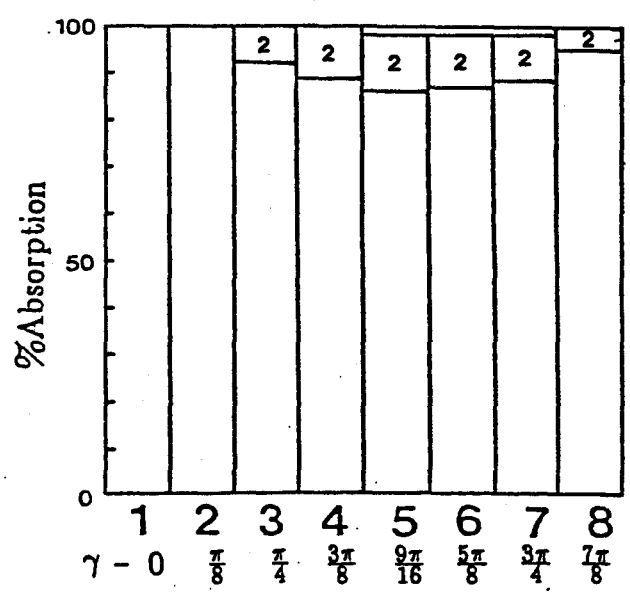
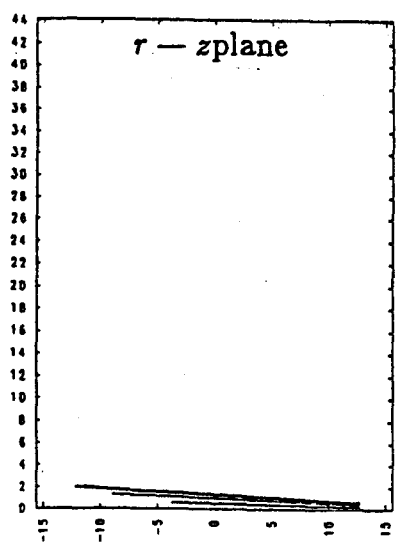
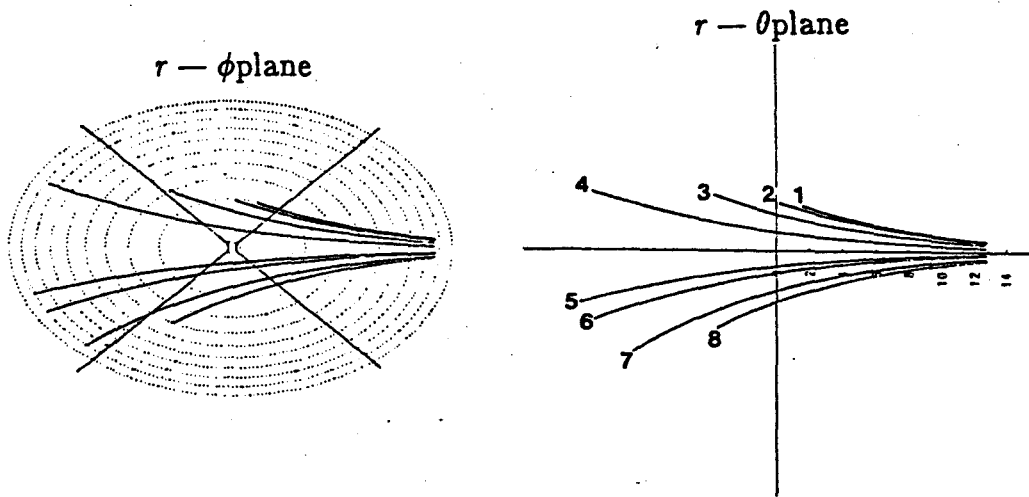


Figure 7.13 Trajectories of O-Waves Launched from the Low Field Side in Wendelstein VII A ($\rho = 5^\circ$, $r = 0.20m$)

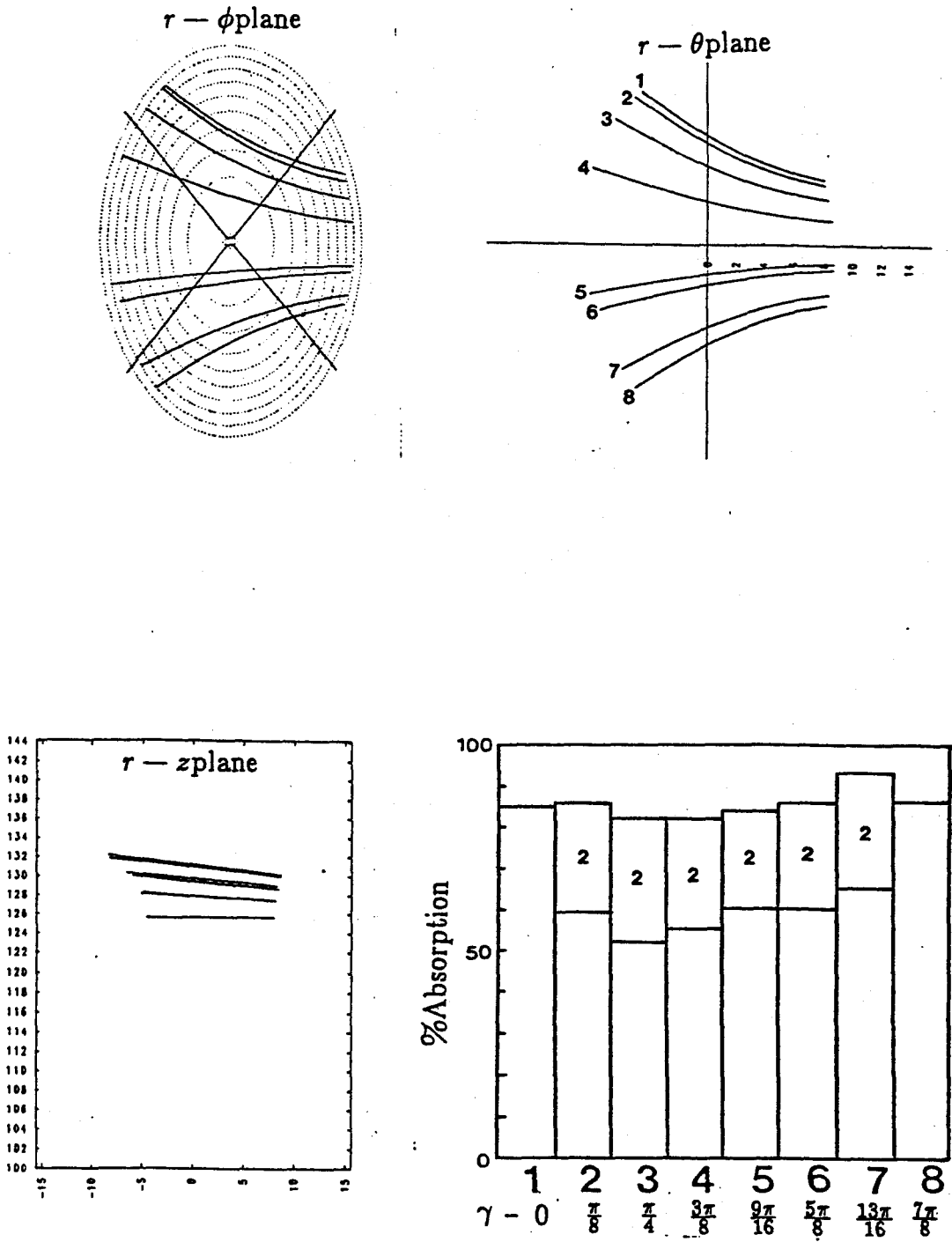


Figure 7.14 Trajectories of O-Waves Launched from the High Field Side in Wendelstein VII A ($\rho = 10^\circ$, $r = 0.35m$)

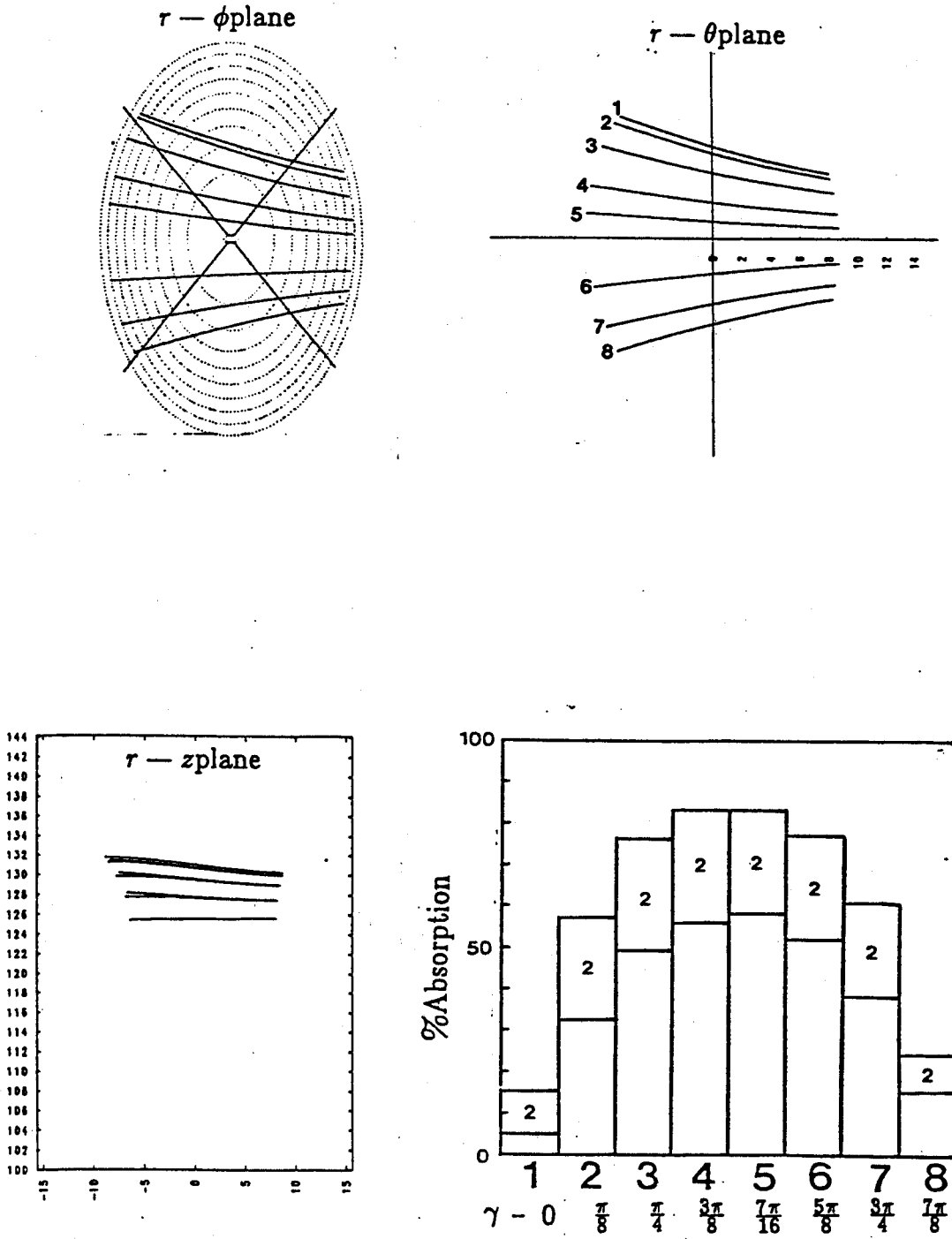
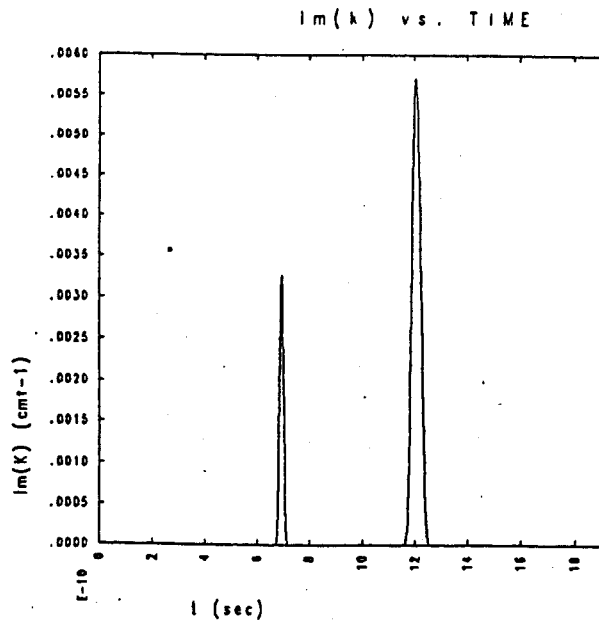


Figure 7.15 Trajectories of X-Waves Launched from the High Field Side in Wendelstein VII A ($\rho = 10^\circ$, $r = 0.35m$)

a. Case IV, Heliotron E (Ray 8, Figure 7.6)



b. Case IV, Wendelstein VII A (Ray 5, Figure 7.15)

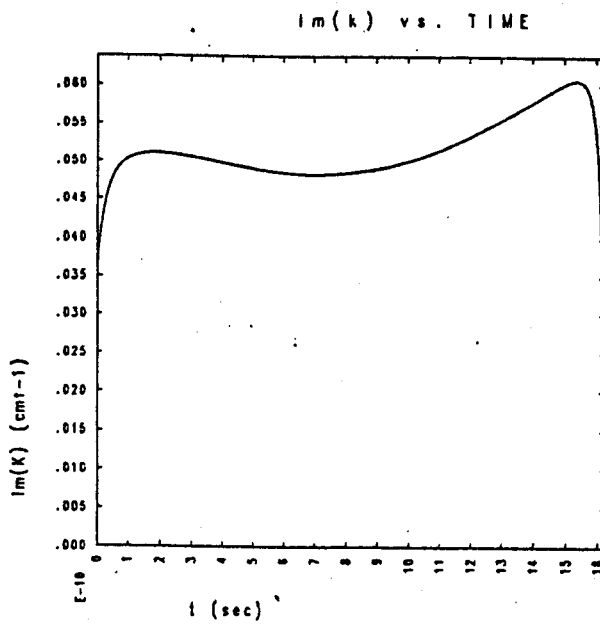
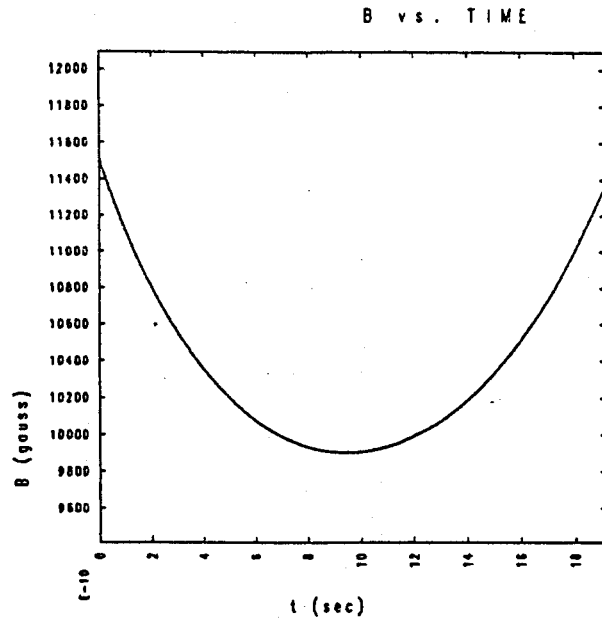


Figure 7.16 Comparison of Heliotron E and Wendelstein VII A Damping Terms

a. Case IV, Heliotron E (Ray 8, Figure 7.6)



b. Case IV, Wendelstein VII A (Ray 5, Figure 7.15)

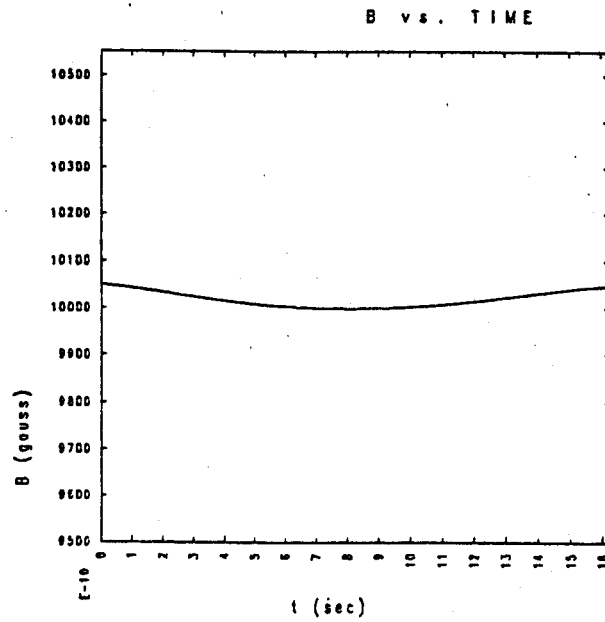


Figure 7.17 Comparison of Heliotron E and Wendelstein VII A Magnetic Field

Figure 7.16 a, due to the large change that the field magnitude undergoes (Figure 7.17 a), the resonances are essentially short spikes in time corresponding to short spatial absorption.

Therefore, the long L_B due to the shearless geometry enhances absorption as seen by the comparison of Wendelstein VII A and Heliotron E.

7.2.7 $l = 3$ Stellarator .

Figures 7.18 through 7.20 show Cases I, III, and IV for the $l = 3$ Stellarator. X-waves from the low field side are reflected out just as in the two previous devices. This result is again not presented since the rays do not propagate very far before the WKB criterion (Equation (4.28)) is violated. O-waves, both from the low field side and the high field side, experience high absorption (73 % and 95 %, respectively), and also pass through the resonance at least twice. Here again, the peak of the absorption graph is near the center, indicating more absorption in the central region. The X-wave absorption from the high field side (47 %) is lower than the O-wave, which is consistent with previous results.

Although quantitative comparison of $l = 3$ Stellarator with Heliotron E and Wendelstein VII A is difficult due to the different peak density and density profile (even though m_n is the same the behavior of the flux function is not), advantage of going to a larger l number for ECRH is clear. Rays pass through more cyclotron layers, resulting in high total absorption.

7.3 Effects of Toroidicity

For the two existing devices, Heliotron E and Wendelstein VII A, the applicability of the simulation results is an intriguing question. To determine this, the relative significance of the helical and the toroidal effects were compared. As a global measure of the two effects, the maximum difference in the magnetic field strength in the plasma due to the straight stellarator effect is compared to the

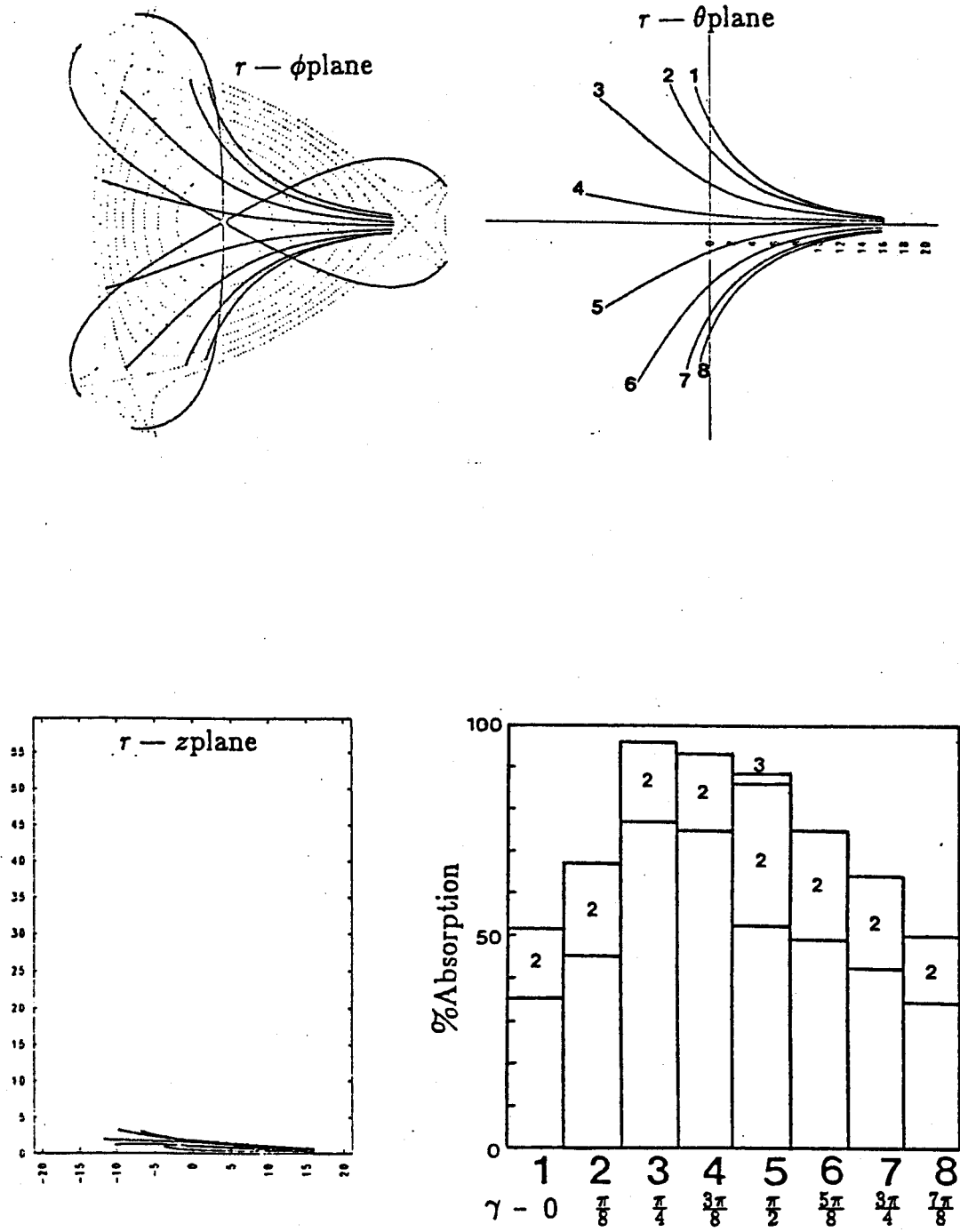


Figure 7.18 Trajectories of O-Waves Launched from the Low Field Side in $l = 3$ Stellarator ($\rho = 5^\circ$, $r = 0.25m$)

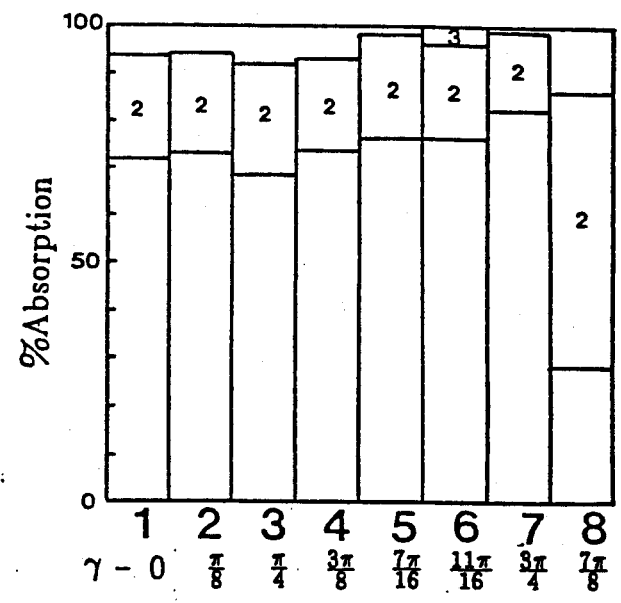
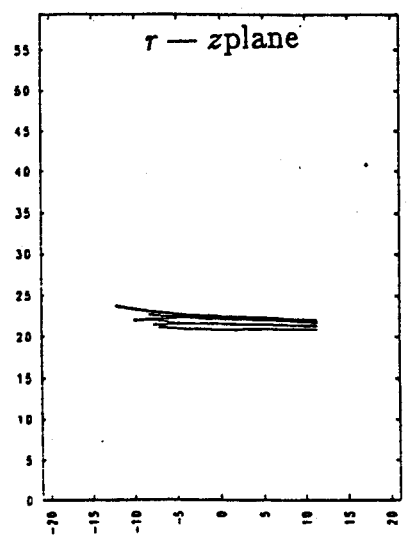
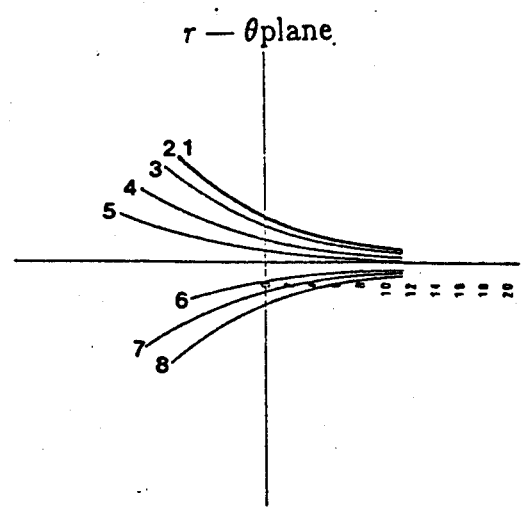
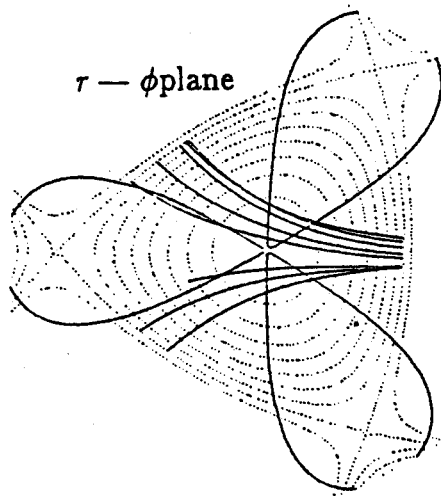


Figure 7.19 Trajectories of O-Waves Launched from the High Field Side in $l = 3$ Stellarator ($\rho = 5^\circ$, $r = 0.25m$)

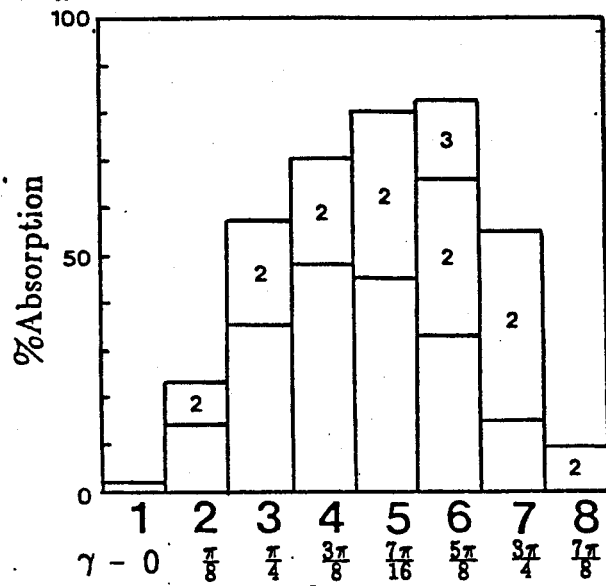
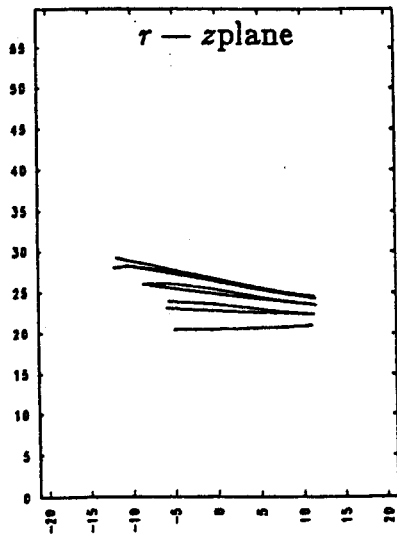
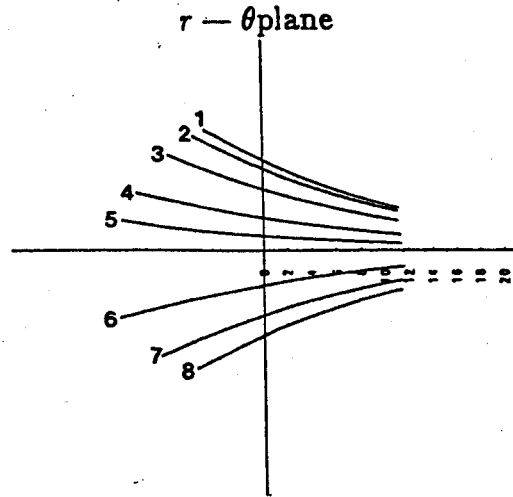
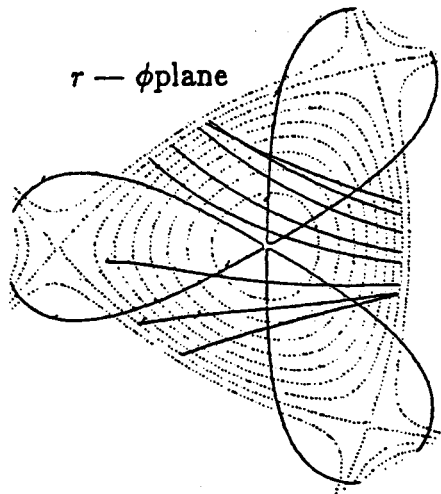


Figure 7.20 Trajectories of X-Waves Launched from the High Field Side in $l = 3$ Stellarator ($\rho = 15^\circ$, $r = 0.25m$)

same due to the toroidal effect. These values are obtained by the following prescriptions.

$$\Delta B_{hel} = B_{hel}^{max} - B_{hel}^{min}; \quad (7.2)$$

$$B_{hel}^{max} = B(\phi = \frac{\pi}{l}, r = r_s); \quad (7.3)$$

$$B_{hel}^{min} = B(\phi = 0, r = r_s); \quad (7.4)$$

$$\Delta B_{tor} = B_{tor}^{max} - B_{tor}^{min}; \quad (7.5)$$

$$B_{tor}^{max} = \frac{B_o R}{R - \bar{a}}; \quad (7.6)$$

$$B_{tor}^{min} = \frac{B_o R}{R + \bar{a}}. \quad (7.7)$$

Here, subscripts *hel* and *tor* refer to helical and toroidal components and the superscripts *max* and *min* refer to the maximum and the minimum values. Using these definitions, ΔB_{hel} and ΔB_{tor} were calculated for the two devices. The results are shown in Table 7.2. It shows that for Heliotron E, the value of $\frac{\Delta B_{tor}}{\Delta B_{hel}}$ is 0.36, which indicates that the global field gradient is dominated by the helical effect, while for Wendelstein VII A, the toroidal effect is the dominant source of the field gradient, with the value of the same quantity being 5. Therefore, the toroidal effect on the absorption length is expected to be small in the case of Heliotron E; but in Wendelstein VII A, the absorption length is expected to be reduced significantly, since the field gradient per length in the Wendelstein VII A device is increased considerably by the toroidal effect and becomes comparable in magnitude to the Heliotron E value.

It can be inferred therefore that the toroidal effect will totally dominate in Wendelstein VII A, and the applicability of the results of the straight analysis is doubtful. However, for Heliotron E the global effect of the toroidal field gradient is small compared to the helical effect so the result of the straight analysis is expected to hold.

Even if the size of the cyclotron resonance layer is not affected by the toroidal effect in Heliotron E, the shape and the position are. To determine precisely the location of the cyclotron resonance layer in a toroidal stellarator requires the use of a more elaborate magnetic field calculation than the one used in this research. In order to obtain roughly a first order correction by the

Table 7.2
Comparison of Helical and Toroidal Effects

	Heliotron E	Wendelstein VII A
$R(m)$	2.2	2.0
$\bar{a}(m)$	0.2	0.1
A	11	20
<hr/>		
$B_{hel}^{max}(Tesla)$	1.16	1.01
$B_{hel}^{min}(Tesla)$	0.66	0.99
$\Delta B_{hel}(Tesla)$	0.50	0.02
<hr/>		
$B_{tor}^{max}(Tesla)$	1.10	1.05
$B_{tor}^{min}(Tesla)$	0.92	0.95
$\Delta B_{tor}(Tesla)$	0.18	0.10
<hr/>		
$\frac{\Delta B_{tor}}{\Delta B_{hel}}$	0.36	5.00
$\frac{\Delta B}{\bar{a}}(Tesla/m)$	2.50	1.00

toroidal effect to the magnetic geometry, the magnetic field and flux function equations (Equations (2.2) through (2.4), (2.11)), were modified such that both B_o and B_h fall off as $\frac{1}{R}$, i.e.:

$$B_o(r, \theta) = \frac{B_o R}{(R + r \cos \theta)}; \quad (7.8)$$

$$B_h(r, \theta) = \frac{B_h R}{(R + r \cos \theta)}. \quad (7.9)$$

It must be emphasized here that this is a very crude approximation. But using these expressions, flux surface plots, with the cyclotron layer for Heliotron E oriented in two primary directions with respect to the mid-plane, were obtained and are shown in Figure 7.21.

In this figure, all the machine parameters are as given in Table 6.1, and the resonant frequency corresponds to a 1 *Tesla* magnetic field. The resulting

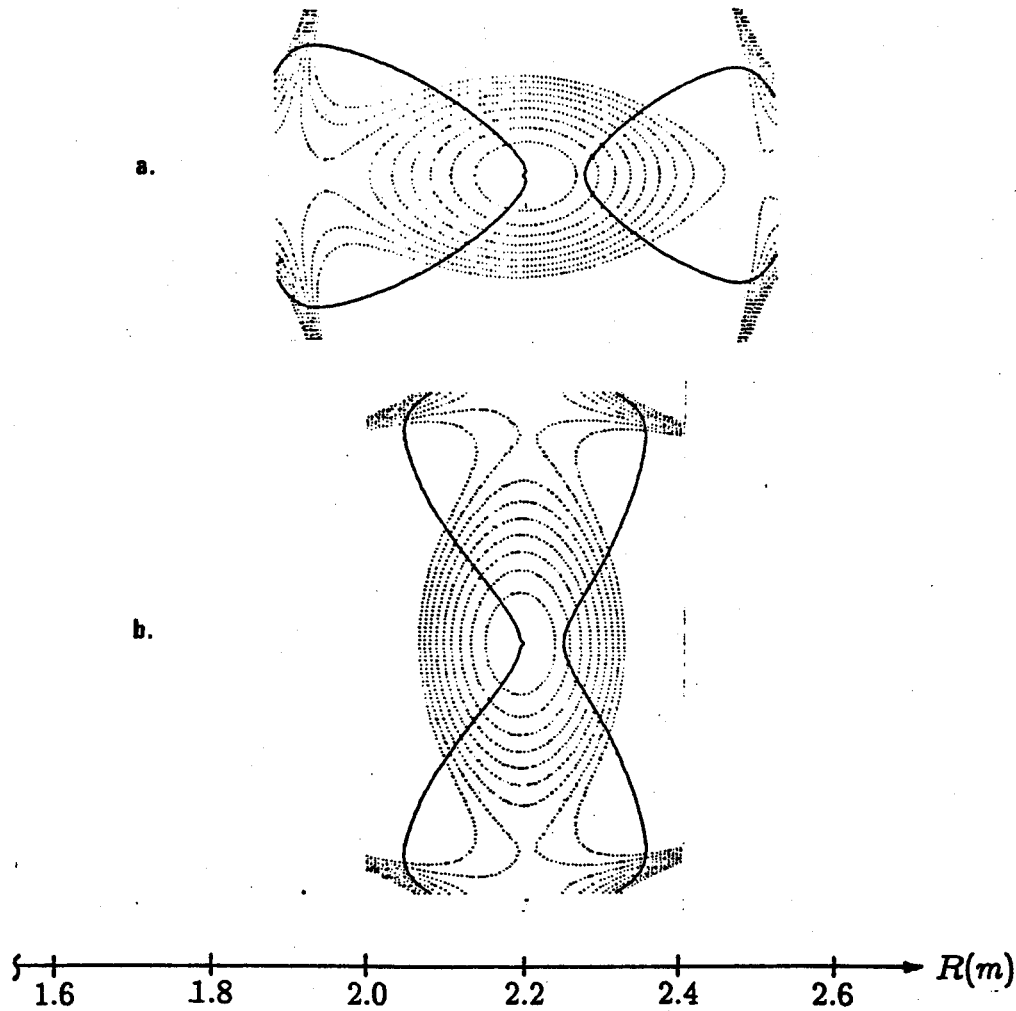


Figure 7.21 Quasi-Toroidal Effects

change in the flux surface is that it loses the symmetries with respect to the principal axes, although the general shape is conserved. As for the resonance layer, Figure 7.21 a shows a deformation similar to a decrease in the wave frequency (see Figure 7.9 a or b), while Figure 7.21 b shows a deformation similar to an increase in the wave frequency (Figure 7.9 d or e). It is possible to create an X point of the cyclotron layer at the center of the plasma in one or the other plot by tuning the frequency, but not in both at the same time.

Based on this finding, it can be seen that waves launched from the top or the bottom will see the gap in the center, and will result in an absorption profile

similar to Figure 7.10 d or e, while if the waves are launched from the sides, the absorption profile will be similar to Figure 7.10 a or b. Hence, the first order effect of toroidicity on the position of the resonance layer is similar to that of frequency detuning, and in that case, a higher absorption will result if the waveguide is positioned such that it does not see the gap in the resonance layer, i.e., low field launch in the case of Figure 7.21 a, high field launch in the case of Figure 7.21 b.

7.4 Comparison with Experimental ECRH in Stellarators

ECRH experiments in stellarators have been conducted in Cleo, JIPPT-II, and Heliotron E in recent years. In Cleo, 12kW of RF power at 17.5GHz is used for start-up and heating experiments[38]. For perpendicular injection, results indicate lower reflectivity of O-waves compared to X-waves, and the X-wave absorption is attributed to the mode conversion at the upper-hybrid layer into a Bernstein wave, with subsequent absorption of that inbetween electron cyclotron and upper-hybrid layers. In JIPPT-II, 40kW at 35.5GHz is launched from the top and the outside[39]. Results show equal heating efficiency of O- and X-waves at $2.2 \times 10^{13} eV \cdot cm^{-3} \cdot kW^{-1}$ at $\bar{n} = 6 \times 10^{12} cm^{-3}$. Reflection and depolarization at the vacuum chamber wall are thought to be responsible for the high absorption of X-waves.

It should be noted at this point that even though Cleo and JIPPT-II are classical stellarators, the toroidal effect is so much stronger compared to the helical effect in the bulk of the plasma that the resonance layers are considerably different from those of the straight stellarator. In addition, the experimental focus so far is on the study of current-free plasma generation and not on the wave propagation, so that it is difficult to extract a common denominator between the simulations done here and these experimental results.

In Heliotron E, ECRH data are, as given in Table 6.1, 200kW at 28GHz for 10ms. This experiment is scheduled to be up-graded to 100ms of 1MW at

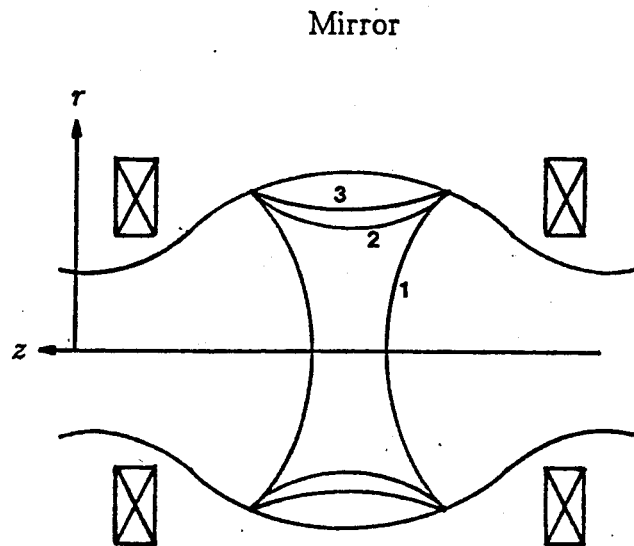
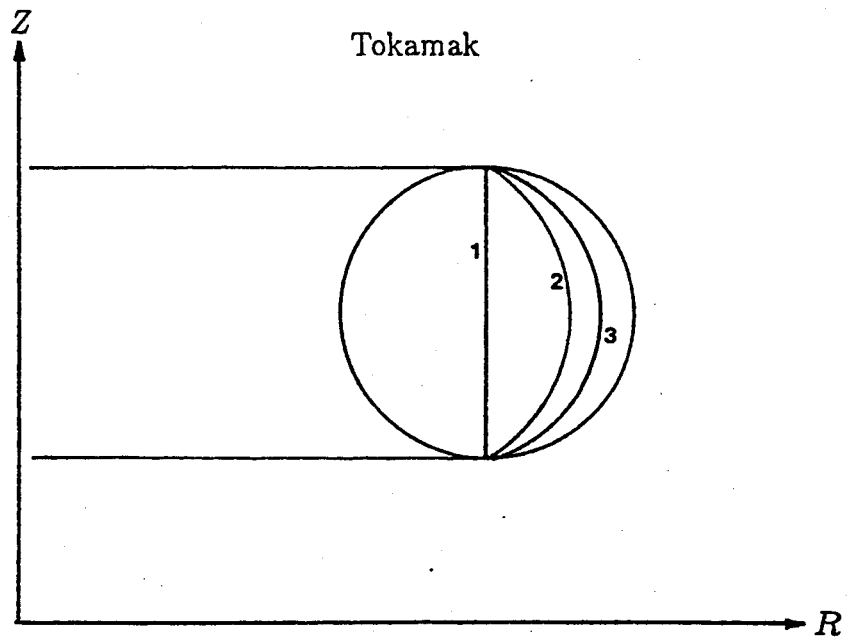
54GHz. Results show high heating efficiencies of $10\text{eV}/\text{kW}$ at the center, or $8\text{J}/\text{kW}$ of average energy for, 50 - 50 mixture of O- and X-waves launched perpendicularly from the low field side on the outside mid-plane[40]. The absorption efficiency is close to 100 %, which clearly disagrees with results presented here. The simulation results have shown that X-waves are totally reflected off the right cut-off layer, and that the O-wave absorption is, at best, on the order of 25 % even for very well focused rays (small ρ).

This discrepancy can be explained by the reflected X-waves and transmitted O-waves undergoing reflection and depolarization at the metallic wall of the vacuum chamber, as suggested in other experiments including JIPPT-II[39] and EBT[17]. Therefore, it is seen that the present state of the simulation model is insufficient in covering all the important aspects of the experiment.

7.5 Comparison with Tokamak and Mirror ECRH

In order to compare stellarator ECRH to tokamak or mirror ECRH, it is necessary to clarify the difference in the latter two devices. ECRF resonance layers for tokamaks and mirrors are shown in Figure 7.22. In tokamaks, the X-wave can access the cyclotron layer only from the inside of the torus, and in mirrors, the same is true only from the throat, i.e., inside of the mirror coils.

The geometry of stellarators is closer to that of tokamaks than mirrors, at least as far as the ECRF is concerned, for two reasons. First, the magnetic field lines are in approximately the same plane as the cyclotron resonance layer in tokamaks, while the field lines are nearly perpendicular to the cyclotron resonance layer in mirrors. In stellarators, the magnetic field lines are also approximately in the plane of the resonance layer, resembling tokamaks. Second, the plasma profiles in tokamaks are a function of the flux surface only, just like the stellarator model, while in mirrors, the plasma profiles are functions both of the flux surface and the axial coordinate. Hence in this regard, too, stellarators are closer to tokamaks.



- 1 — Cyclotron Resonance Layer
- 2 — Upper-Hybrid Resonance Layer
- 3 — Right Cut-Off Layer

Figure 7.22 ECRF Resonance Layers in Tokamaks and Mirrors

Typical wave vector profiles from the Heliotron E result, one for $\frac{k_{\perp}}{k_{\parallel}} \gg 1$, and the other for $\frac{k_{\perp}}{k_{\parallel}} \approx 1$, are shown in Figure 7.23 to indicate the perpendicularly stratified nature of stellarators, i.e., change in k_{\perp} governs the change in the overall magnitude of k . The limit of $\frac{k_{\perp}}{k_{\parallel}} \ll 1$ is not presented since such a launching angle is uncommon for a magnetically confined toroidal plasma. In these plots, the minimum in the curve of k_m indicate the ascent of the ray up to the highest density point. It is seen that for both cases, the governing change appears in k_{\perp} , and k_{\parallel} is hardly affected. In fact, k_{\parallel} is nearly constant in central regions for both cases.

Advantages of stellarators over tokamaks can be summarized from discussions presented in previous sections. They are:

- (1) outside access of X-waves to the electron cyclotron layer is possible in a high shear, large aspect-ratio stellarator;
- (2) for a plasma of comparable size, better ray focus is obtained in the high field side launch of stellarators than in tokamaks since the radius of curvature of the flux surfaces on the stellarator high field side is larger than the minor radius itself.

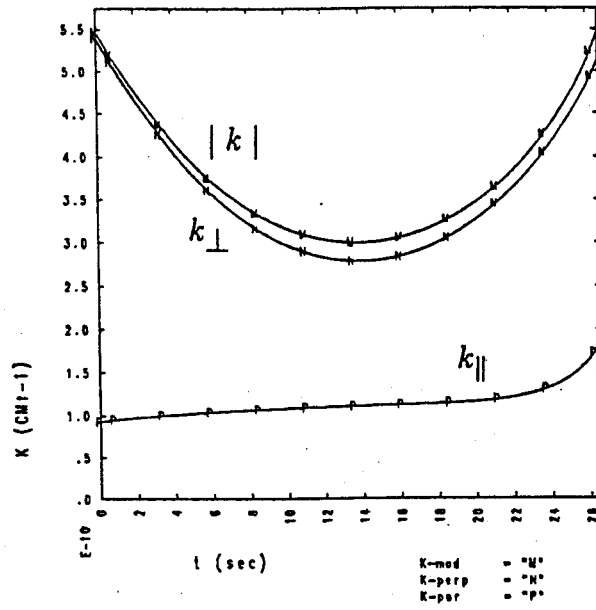
7.6 Guidelines Defined for ECRH in Stellarators

Having investigated ECRH in stellarators with respect to the launching position, launching angle, wave mode, and frequency; and having considered the effects of toroidicity; defining guidelines for experimental, or reactor ECRH in stellarators follow. Although in most(or all) of the present day experiments, high overall absorption is obtained on account of wall reflection and the particular launching position or the direction of the wave guide does not seem to matter significantly, maximization of the absorption on the first pass before any reflection from the walls is considered here.

It is evident from the discussion of accessibility in Chapter 3 that X-waves should be launched from the high field side in order for them to be accessible

$$k_{\perp} \gg k_{\parallel}$$

K-mod, K-perp, K-par vs. TIME



$$k_{\perp} \approx k_{\parallel}$$

K-mod, K-perp, K-par vs. TIME

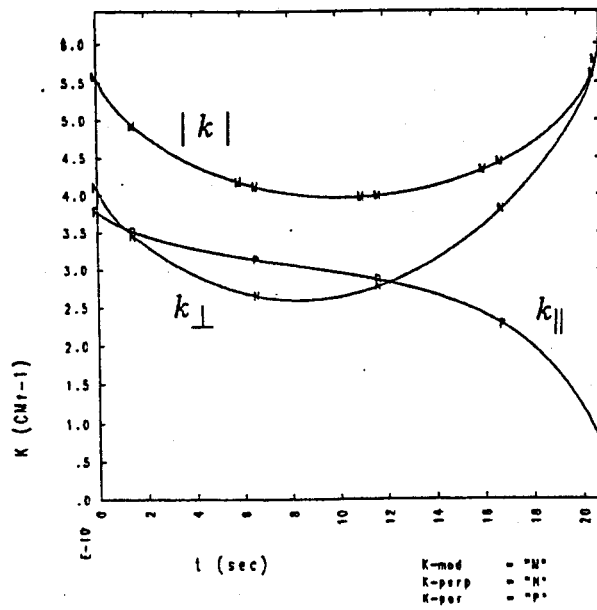


Figure 7.23 Plots of k vs. Time for O-waves in Heliotron E

to the cyclotron resonance. However, the superiority of high field side launch is also valid for O-waves since on the high field side, flux surfaces have larger radius of curvatures than on the low field side. This means that for perpendicular injection, the angle between the wave vector and the density gradient vector is small on the high field side, and the curvature of the wave trajectory is minimized there. The first observation therefore is that the high field side launch is preferred for both O- and X-waves.

A conclusion drawn from Figure 7.7(Absorption contours) is that an elliptical waveguide radiation pattern is preferred over a circular one if the FWHM cone half angle exceeds more than a few degrees. (This is based strictly on Heliotron E simulation results, but it should qualify as a general statement for similar size devices.) Such an elliptically radiating waveguide, oriented appropriately with respect to the plasma axis, will closely match the absorption profile resulting in efficient power deposition of the bulk of the transmitted power. Thus the second observation is that an elliptical waveguide radiation pattern is preferred over a circular one.

In considering the toroidal effects on the geometry, it was found that the magnetic field gradient scale length, which is an important factor governing the total absorption in the cyclotron layer, is affected by the toroidicity; and that the shape and position of the resonant surfaces are also affected. The first effect of the gradient scale length alteration is more prominent in low shear, small aspect-ratio devices, while high shear, large aspect-ratio devices are the least affected. The second effect of the position alteration is inversely proportional to the aspect-ratio, i.e., small aspect-ratio devices are affected the most. Examination of Figure 7.21(Quasi-toroidal effect) leads to the conclusion that launching the wave horizontally on the mid-plane is preferred over launching the wave vertically from the top or the bottom. The former launching geometry will avoid the gap in absorption profile that the latter will face. So the third observation is that launching the waves horizontally on the mid plane is preferred over launching the waves vertically from the top or the bottom.

In the preceding discussion, "wishes" regarding how to conduct ECRH has

been presented. They are:

- (1) high field side launch for accessibility and better focus of waves;
- (2) elliptical waveguide radiation pattern for more efficient power transfer;
- (3) mid-plane launch for higher absorption.

However, the question of accessibility, not of the resonance layer but of the launching position must be considered next. It must be noted that in a classical stellarator configuration, the helical coils are placed directly over the lowest and the highest field points, so that the desired launching position will conflict with the placement of the coil. A straight waveguide will not do. In fact, in the scale of today's experiments, it is probably very difficult to bend the waveguide and place it on the high field side, pointed towards the plasma. In a reactor scale device, the idea is not far fetched if the waveguide can be bent around the magnet. In addition, stellarators are not removed from tokamak type accessibility problems. Namely, the advantage and even the necessity of locating the waveguide on the inside of the torus. It should be relatively easy for large aspect-ratio devices with no ohmic heating, but should be just as difficult as for tokamaks for small aspect-ratio devices, with or without ohmic heating.

At this time, it is not clear whether a stellarator reactor will have a high shear, low shear, large aspect-ratio, or small aspect-ratio. From the point of view of ECRH, the following are desirable:

- (1) large l number and small shear stellarator in order to get high absorption in one pass even for moderate plasma parameters;
- (2) large shear stellarator in order to localize heat deposition;
- (3) large coil radius to plasma radius ratio for accessibility of the launching position.

Recommendations for stellarator ECRH as discussed above are presented graphically in Figures 7.24 and 7.25. Figure 7.24 shows the recommended waveguide radiation pattern; the particular figure shows a low field side launch, but the general shape of the radiation pattern should be the same for a machine regardless of the launching position. Figure 7.25, on the other hand, shows

how a wave guide should be positioned, here in a cross-sectional view. In this particular figure, a reactor scale device is considered and two waveguide assemblies, one from the inside and the other from the outside of the torus, are shown. The necessary condition for the outside, mid-plane launch is that the helical effect be strong compared to the toroidal effect so that there indeed is a high field region on the outside of the torus.

7.7 Summary

Various results of ray-tracing in stellarators were presented in this chapter. These works were done on the three models defined in Chapter 6, with particular emphasis on Heliotron E. For all three models, launching position and mode scan was carried out with the following results: higher absorption of O-waves launched from the high field side than the low field side; higher absorption of O-waves compared to the X-waves for the high field side launch; and total reflection of X-waves launched from the low field side.

Comparison of the different machines showed that a low shear geometry such as that of Wendelstein VII A results in high overall absorption while a high shear geometry such as that of Heliotron E results in localized absorption. Also, the advantage of large l number geometry is clear if high total absorption is desired.

The existing launching geometry of Heliotron E was investigated in detail, and power absorption contours were mapped as a function of the ray injection points (Figure 7.7). This result shows that the contours can be approximated by elongated ellipses, with the long axis oriented about half-way between the toroidal direction and the saddle point line.

Investigation was also carried out on the effect of changing the shape and the position of the resonance layers. It was found that detuning the frequency from the resonance frequency on axis reduces absorption.

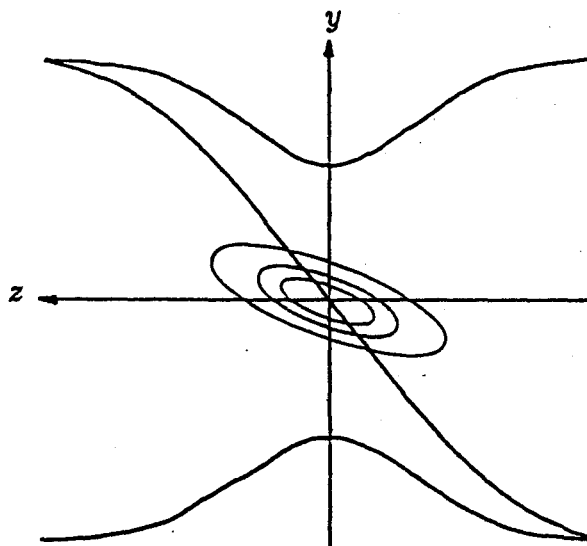


Figure 7.24 Recommended Waveguide Radiation Pattern

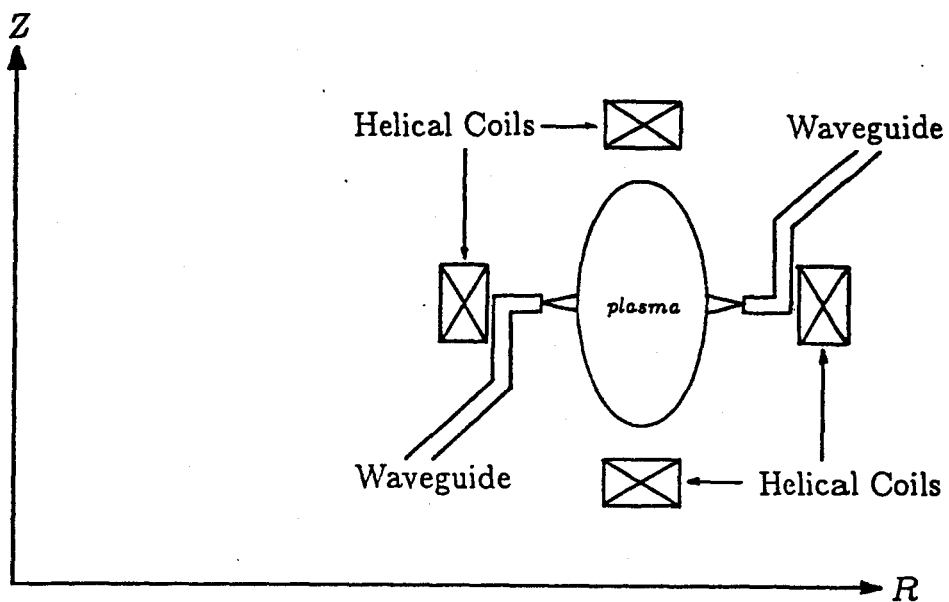


Figure 7.25 Recommended Launching Position

The helical magnetic geometry, as opposed to helical plasma profile in these machines contribute very little to the propagation characteristics, however, low shear in the central region does contribute to enhancing the central absorption.

How the resonance layers evolve with changing density was also looked at, and some qualitative discussions were given, but the actual ray tracing was not done for this case due to insufficient coverage of the upper-hybrid layer physics on the part of the computer code. As long as the upper-hybrid layer is not pushed out too fast, it will be responsible for the initial central heating at low temperatures and the cyclotron layer will take over afterwards.

Specific aspects of the results were discussed next. First, the effects of toroidicity were addressed. The simple analysis showed that the absorption will probably be reduced markedly in Wendelstein VII A due to the toroidal effect, while the effect was found to be small compared to the helical effect in Heliotron E. The effect of toroidicity on the shape and the position of the resonance layer is found to be similar to that of frequency detuning discussed earlier.

Having investigated the applicability of the simulation results to toroidal devices, an attempt was made to relate these results to the experimental results, especially in Heliotron E. However, it was quickly realized that the present state of the code is not sufficient to reproduce the experimental results, lacking in mode conversion at the upper-hybrid layer, and reflection and depolarization at the wall.

Next the results were compared with tokamak and mirror ECRH. It was found that the propagation characteristics in stellarators are like those of perpendicular stratification, similar to tokamaks. It was found that the rays propagating from the high field side in a stellarator are better focused compared to those in a tokamak of similar size, due to the radius of curvatures of flux surfaces which are larger for stellarator high field side than for tokamaks.

Finally, a consistent set of guidelines for ECRH in stellarators was formulated. As summarized in Figures 7.24 and 7.25, required conditions are an elliptical waveguide radiation pattern and a mid-plane, high field side launching position.

Desirable conditions for the stellarator itself are: a low shear, large l number geometry for high overall deposition; a high shear geometry for central deposition and X-wave access; and a large coil radius to plasma radius ratio for accessibility to the launching position.

Chapter 8

Summary and Conclusions

8.1 Summary and Conclusions

Since the details of the power producing fusion reactor is still an open question, it is important to accumulate database for the back-up devices such as stellarators. Stellarators, being current-free steady-state devices, will require a bulk heating scheme such as the ECRH, which was investigated in this thesis by numerical methods.

The set up of a numerical procedure involves two aspects; the modeling of the environment, and the modeling of the physical phenomenon to be investigated. To model the environment, i.e., a stellarator plasma, it was decided early on to consider the straight stellarator model, whose magnetic fields and flux surfaces are given by analytical expressions. In order to completely characterize the magnetic field geometry, expressions for calculating the rotational transform in the model was also derived. The confined plasma was given density and temperature profiles which are simple functions of the flux function. This straight stellarator model was found to model best the large aspect-ratio, short pitched devices with classical windings. The model cannot be applied to helical axis stellarators or modular stellarators.

As for the modeling of the physical phenomenon, ECRF propagation in plasmas and ray-tracing were discussed in detail. In the first part which dealt with ECRF, Appleton-Hartree dispersion relation was presented and resonances and cut-offs were derived from the relation. Classifications of waves by polarization(R and L), electric field orientation(O and X), and the magnitude of the phase velocity(F and S) were also given. CMA diagram was described to clarify these ideas as well as the question of accessibility.

Absorption of the wave energy in a finite temperature plasma was discussed next. The mechanism of cyclotron resonance of the O- and X-waves were explained, as well as the general expression for the damping formula used in the computer code. It was indicated here that the upper-hybrid physics at finite temperatures is complicated and is beyond the scope of this thesis.

In the discussion of ray-tracing, assumptions for the WKB approximation were presented first. They are: (1) small perturbation; (2) slowly changing medium; (3) slowly changing wavelength; and (4) weak damping. Further assumptions of an isotropic medium and plane waves make possible the wave propagation analysis using the ray-tracing technique. The technique is an initial value problem which solves Snell's law equations and the group velocity equations with respect to time, and obtain the position and the wave vector of the ray. These ray equations, written out in cylindrical coordinates in computable form, are Equations(4.19) through(4.24). Limits on the applicability of the technique are determined by whether or not the assumptions listed above are valid. Even if the assumptions are justified, numerical instabilities in the computing stage may preclude regions of small radius or plasma edge from the analysis. The inherent limit on the applicability to other classes of waves is set by the type of dispersion relation used.

Using the straight stellarator model, the cold plasma dispersion relation, the finite temperature damping formula, and the ray equations, a group of codes were developed to carry out the simulation. These codes are MAC(MACHine parameters code), HERA(HELical plasma RAY tracing code), and GROUT(GRaphics OUTput code), which all reside on the CRAY-I at

MFECC. MAC produces the machine parameters determined by the straight stellarator model, given a suitable input. HERA, which was developed in stages, does the ray-tracing and produces a text file. This text file is then processed by GROUT to produce graphics. Since ray-tracing is an initial value problem, it is important to be able to specify the initial conditions as flexibly as possible. HERA is equipped with routines to handle most situations.

To initiate the simulation, three models were determined using MAC. These models correspond to Heliotron E, Wendelstein VII A, and an $l = 3$ stellarator. The first two machines are $l = 2$ devices and are chosen because of their ECRH capability. The main difference between the two is the rate of shear which is high for Heliotron E and low for Wendelstein VII A. The $l = 3$ stellarator was chosen as the third machine to investigate the advantage of going to larger l numbers.

Various aspects of ECRH simulations were carried out for the three models, with a particular emphasis on Heliotron E. The launching position scan showed that high field side launch is favorable both for O- and X-waves. This is so for the O-wave since better focus is obtained from the high field side, and for the X-wave since the reflection at the right cut-off makes it inaccessible to the cyclotron resonance from the low field side. The simulation of Heliotron E launching geometry showed that an elliptical waveguide radiation pattern, with its long axis oriented about half-way between the toroidal axis and the saddle point line, is preferred over a circular one. By detuning the wave frequency, it was found that the total absorption decreased. A central gap in the absorption profile is created for the high field side launch if the frequency is decreased, while the gap is created for the low field side launch if the frequency is increased. The wave trajectory was not affected by the helical magnetic fields, although the small shear at the center due to the helical geometry contributed to higher central absorption. Inspection of the resonance layers as a function of density showed that at low densities (and low temperatures for start-up), the upper-hybrid layer, which contributes to low temperature heating, is close to the cyclotron layer (i.e., center), but gets pushed out with plasma formation.

Wendelstein VII A simulation results show high absorption rate due to the shearless geometry, while high absorption also resulted in $l = 3$ Stellarator due to the larger number of resonance layers.

Actual devices are affected by toroidal effects. It was found that the helical effect is dominant compared to the toroidal effect in Heliotron E so that the straight stellarator simulation is valid. In Wendelstein VII A, it was found that the toroidal effect is dominant and the difficulty exists in applying the simulation result to the actual machine. The effect of $\frac{1}{R}$ fall-off of the fields on the resonance layer shape and position were found to be similar to the effect due to frequency detuning, which had already been discussed.

Comparison of simulation results with experimental observation cannot be made directly at this stage of research since the important effects of wall reflection and depolarization, as well as the upper-hybrid mode conversion, are not taken into account in the computer code. Comparison of simulation results with tokamak or mirror ECRH showed that the geometry and stratification properties of the straight stellarator are much like those of tokamaks due to the fact that (1) the angle between the resonance layer and the field lines is small, and (2) density and temperature are function of the flux surface, in both stellarators and tokamaks. Also, typical profiles of k showed that change in overall magnitude of k is governed by the change in k_{\perp} for realistic angles of injection. Advantages of stellarator ECRH over tokamak ECRH are (1) access of X-waves launched from the outside to electron cyclotron resonance layer is possible in a high shear machine, and (2) better ray focus for high field side launch is possible in plasmas of comparable size. Disadvantage of the same is that helical coils prohibit straightforward access to the desired launching point.

From these results, a consistent set of guidelines were formulated for stellarator ECRH, with an aim to get as much power as possible absorbed in the first pass prior to wall reflection. The guidelines are:

- (1) elliptical radiation pattern for more efficient power transfer;
- (2) high field side launch for accessibility and better focus of waves;

(3) mid-plane launch for higher absorption.

Properties of a stellarator favorable to ECRH are:

- (1) high shear for localization of absorption and outside access of X-waves;
- (2) low shear and large l for high total absorption;
- (3) large coil radius to plasma radius ratio for accessibility to the launching position.

8.2 Recommendations for Future Investigation

Further work is suggested in the following areas.

- (1) Make the model more realistic.
- (2) Increase the capability of the model.
- (3) Investigate related topics.

In order to make the model more realistic, toroidicity should be taken into account, and the plasma parameter profiles should be given more flexibility. Finite temperature plasma dispersion relation including effects of relativistic mass increase of electrons should be used to trace the rays.

As for increasing the capability of the model, inclusion of the upper-hybrid layer physics is of the utmost importance. Wall reflection and depolarization should also be taken into account to accurately simulate experiments.

Within the bounds of the straight stellarator, related topics can be investigated. First is the consideration of other frequency regimes such as the lower-hybrid and ion cyclotron frequencies. A Fokker-Planck analysis may be done in which the ray-tracing result is used as the input to calculate the time evolution of an ECRH plasma.

Appendix A

Partial Derivatives of the Dispersion Relation

In this Appendix, expressions for the partial derivatives of the Appleton-Hartree dispersion relation are given in detail.

1 Dispersion Relation

$$F = SN_{\perp}^4 + (N_{\parallel}^2(S + P) - PS - RL)N_{\perp}^2 + (PN_{\parallel}^4 - 2PSN_{\parallel}^2 + PRL) = 0. \quad (\text{A.1})$$

Where,

$$N_{\parallel}^2 = \frac{k_{\parallel}^2 c^2}{\omega^2}; \quad (\text{A.2})$$

$$N_{\perp}^2 = \frac{k_{\perp}^2 c^2}{\omega^2}; \quad (\text{A.3})$$

$$R = 1 - \frac{\omega_{pe}^2}{\omega^2} \left(\frac{\omega}{\omega + \omega_{ce}} \right); \quad (\text{A.4})$$

$$L = 1 - \frac{\omega_{pe}^2}{\omega^2} \left(\frac{\omega}{\omega - \omega_{ce}} \right); \quad (\text{A.5})$$

$$S = \frac{1}{2}(R + L); \quad (\text{A.6})$$

$$P = 1 - \frac{\omega_{pe}^2}{\omega^2}; \quad (\text{A.7})$$

$$k_{\parallel} = \frac{\mathbf{k} \cdot \mathbf{B}}{|\mathbf{B}|}; \quad (\text{A.8})$$

$$k_{\perp} = (k^2 - k_{\parallel}^2)^{\frac{1}{2}}; \quad (\text{A.9})$$

$$\omega_{ce} = \frac{q_e B_0}{m_e}; \quad (\text{A.10})$$

$$\omega_{pe} = \left(\frac{n_e e^2}{m_e \epsilon_0} \right)^{\frac{1}{2}}. \quad (\text{A.11})$$

Define:

$$F_a \equiv SN_{\perp}^4; \quad (\text{A.12})$$

$$F_b \equiv (N_{\parallel}^2(S + P) - PS - RL)N_{\perp}^2; \quad (\text{A.13})$$

$$F_c \equiv PN_{\parallel}^4 - 2SPN_{\parallel}^2 + PRL. \quad (\text{A.14})$$

Then,

$$F = F_a + F_b + F_c. \quad (\text{A.15})$$

2 Derivative with respect to position

Let ξ denote r , θ , or z . Then,

$$\frac{\partial F}{\partial \xi} = \frac{\partial F_a}{\partial \xi} + \frac{\partial F_b}{\partial \xi} + \frac{\partial F_c}{\partial \xi}. \quad (\text{A.16})$$

Where:

$$\frac{\partial F_a}{\partial \xi} = \frac{\partial S}{\partial \xi} N_{\perp}^4 + 2SN_{\perp}^2 \frac{\partial N_{\perp}^2}{\partial \xi}; \quad (\text{A.17})$$

$$\begin{aligned} \frac{\partial F_b}{\partial \xi} = & \left(\frac{\partial N_{\parallel}^2}{\partial \xi} (S + P) + N_{\parallel}^2 \left(\frac{\partial S}{\partial \xi} + \frac{\partial P}{\partial \xi} \right) \right. \\ & \left. - \frac{\partial P}{\partial \xi} S - P \frac{\partial S}{\partial \xi} - \frac{\partial R}{\partial \xi} L - R \frac{\partial L}{\partial \xi} \right) N_{\perp}^2 \\ & + (N_{\parallel}^2 (S + P) - PS - RL) \frac{\partial N_{\perp}^2}{\partial \xi}; \end{aligned} \quad (\text{A.18})$$

$$\begin{aligned} \frac{\partial F_c}{\partial \xi} = & \frac{\partial P}{\partial \xi} N_{\parallel}^4 + 2PN_{\parallel}^2 \frac{\partial N_{\parallel}^2}{\partial \xi} - 2 \frac{\partial P}{\partial \xi} SN_{\parallel}^2 - 2P \frac{\partial S}{\partial \xi} N_{\parallel}^2 \\ & - 2PS \frac{\partial N_{\parallel}^2}{\partial \xi} + \frac{\partial P}{\partial \xi} RL + P \frac{\partial R}{\partial \xi} L + PR \frac{\partial L}{\partial \xi}; \end{aligned} \quad (\text{A.19})$$

$$\frac{\partial N_{\parallel}^2}{\partial \xi} = 2N_{\parallel}^2 \sum_{i=r,\theta,z} \frac{k_i}{k_{\parallel}} \left(\frac{1}{B} \frac{\partial B_i}{\partial \xi} - \frac{B_i}{B^2} \frac{\partial B}{\partial \xi} \right); \quad (\text{A.20})$$

$$\frac{\partial N_{\perp}^2}{\partial \xi} = - \frac{\partial N_{\parallel}^2}{\partial \xi}; \quad (\text{A.21})$$

$$\frac{\partial R}{\partial \xi} = (R - 1) \left(\frac{1}{n} \frac{\partial n}{\partial \xi} + \frac{\omega_{ce}}{B(\omega - \omega_{ce})} \frac{\partial B}{\partial \xi} \right); \quad (\text{A.22})$$

$$\frac{\partial L}{\partial \xi} = (L - 1) \left(\frac{1}{n} \frac{\partial n}{\partial \xi} - \frac{\omega_{ce}}{B(\omega + \omega_{ce})} \frac{\partial B}{\partial \xi} \right); \quad (\text{A.23})$$

$$\frac{\partial S}{\partial \xi} = \frac{1}{2} \left(\frac{\partial R}{\partial \xi} + \frac{\partial L}{\partial \xi} \right); \quad (\text{A.24})$$

$$\frac{\partial P}{\partial \xi} = (P - 1) \frac{1}{n} \frac{\partial n}{\partial \xi}. \quad (\text{A.25})$$

3 Derivative with respect to ω

$$\frac{\partial F}{\partial \omega} = \frac{\partial F_a}{\partial \omega} + \frac{\partial F_b}{\partial \omega} + \frac{\partial F_c}{\partial \omega}. \quad (\text{A.26})$$

Where:

$$\frac{\partial F_a}{\partial \omega} = \frac{\partial S}{\partial \omega} N_{\perp}^4 + 2SN_{\perp}^2 \frac{\partial N_{\perp}^2}{\partial \omega}; \quad (\text{A.27})$$

$$\begin{aligned} \frac{\partial F_b}{\partial \omega} = & \left(\frac{\partial N_{\parallel}^2}{\partial \omega} (S + P) + N_{\parallel}^2 \left(\frac{\partial S}{\partial \omega} + \frac{\partial P}{\partial \omega} \right) \right. \\ & \left. - \frac{\partial P}{\partial \omega} S - P \frac{\partial S}{\partial \omega} - \frac{\partial R}{\partial \omega} L - R \frac{\partial L}{\partial \omega} \right) N_{\perp}^2 \\ & + (N_{\parallel}^2 (S + P) - PS - RL) \frac{\partial N_{\perp}^2}{\partial \omega}; \end{aligned} \quad (\text{A.28})$$

$$\begin{aligned} \frac{\partial F_c}{\partial \omega} = & \frac{\partial P}{\partial \omega} N_{\parallel}^4 + 2PN_{\parallel}^2 \frac{\partial N_{\parallel}^2}{\partial \omega} - 2 \frac{\partial P}{\partial \omega} SN_{\parallel}^2 - 2P \frac{\partial S}{\partial \omega} N_{\parallel}^2 \\ & - 2PS \frac{\partial N_{\parallel}^2}{\partial \omega} + \frac{\partial P}{\partial \omega} RL + P \frac{\partial R}{\partial \omega} L + PR \frac{\partial L}{\partial \omega}; \end{aligned} \quad (\text{A.29})$$

$$\frac{\partial N_{\parallel}^2}{\partial \omega} = -2 \frac{N_{\parallel}^2}{\omega}; \quad (\text{A.30})$$

$$\frac{\partial N_{\perp}^2}{\partial \omega} = -2 \frac{N_{\perp}^2}{\omega}; \quad (\text{A.31})$$

$$\frac{\partial R}{\partial \omega} = (1 - R)^2 \left(\frac{2\omega - \omega_{ce}}{\omega_{pe}} \right); \quad (\text{A.32})$$

$$\frac{\partial L}{\partial \omega} = (1 - L)^2 \left(\frac{2\omega + \omega_{ce}}{\omega_{pe}} \right); \quad (\text{A.33})$$

$$\frac{\partial S}{\partial \omega} = \frac{1}{2} \left(\frac{\partial R}{\partial \omega} + \frac{\partial L}{\partial \omega} \right); \quad (\text{A.34})$$

$$\frac{\partial P}{\partial \omega} = \frac{2}{\omega} (1 - P). \quad (\text{A.35})$$

4 Derivative with respect to k_{\parallel}

$$\frac{\partial F}{\partial k_{\parallel}} = \frac{\partial N_{\parallel}^2}{\partial k_{\parallel}} (S + P) N_{\perp}^2 + 2PN_{\parallel}^2 \frac{\partial N_{\parallel}^2}{\partial k_{\parallel}} - 2PS \frac{\partial N_{\parallel}^2}{\partial k_{\parallel}}. \quad (\text{A.36})$$

Where,

$$\frac{\partial N_{\parallel}^2}{\partial k_{\parallel}} = 2 \frac{N_{\parallel}^2}{k_{\parallel}}. \quad (\text{A.37})$$

5 Derivative with respect to k_{\perp}

$$\frac{\partial F}{\partial k_{\perp}} = 2SN_{\perp}^2 \frac{\partial N_{\perp}^2}{\partial k_{\perp}} + (N_{\parallel}^2(S + P) - PS - RL) \frac{\partial N_{\perp}^2}{\partial k_{\perp}}. \quad (\text{A.38})$$

Where,

$$\frac{\partial N_{\perp}^2}{\partial k_{\perp}} = 2 \frac{N_{\perp}^2}{k_{\perp}}. \quad (\text{A.39})$$

References

- [1] Bishop, A.S., *Project Sherwood; the U. S. Program in Controlled Fusion*, Addison-Wesley Co., Reading, MA (1958).
- [2] Joint US-EURATOM Steering Committee on Stellarators, *Stellarators - Status and Future Directions*, Joint US-EURATOM Report, IPP2/254 (1981)
- [3] Sheffield, J., et.al., "Introduction to ATF-1 at the ATF-1 Proposal Review," Document distributed at Princeton Plasma Physics Laboratory on Oct. 27, 1982.
- [4] Miller, R.L., and Krakowski, R.A., "The Modular Stellarator Fusion Reactor Concept," LA-8978-MS, August, 1981.
- [5] *Magnetic Fusion Energy and Computers*, DOE/ER-0159, January, 1983.
- [6] Miyamoto, K., *Plasma Physics for Nuclear Fusion*, MIT Press, Cambridge, MA (1980).
- [7] Potok, R.E., Lidsky, L.M., and Politzer, P.A., "Particle Confinement and Diffusion in Torsatrons," PFC/RR-80-15, August, 1980.
- [8] Miyamoto, K., "Review Paper - Recent Stellarator Research," Nucl. Fusion 18(1978)243.
- [9] Roemer, P., Private Discussion, at MIT on April 11, 1983.
- [10] Fidone, I., Granata, G., Ramponi, G., and Meyer, R.L., "Wave Absorption Near the Electron Cyclotron Frequency," Phys. Fluids, 21(1978)645.
- [11] Stix, T.H., *The Theory of Plasma Waves*, McGraw-Hill, New York (1962).
- [12] Eldridge, O., Namkung, W., and England, A.C., "Electron Cyclotron Heating in Tokamaks," ORNL/TM-6052, (1980).
- [13] Schuss, J.J., and Hosea, J.C., "Mode Conversion and Harmonic Generation at the Upper Hybrid Layer in Toroidal Plasmas," Phys. Fluids, 18 (1975) 727.
- [14] Antonsen, T.M., and Porkolab, M., "Electron Cyclotron Resonance Heating of High Temperature Plasmas," from Physics of Plasmas Close to Thermonuclear Conditions. Proceedings of the Course held in Varenna, Italy (1979).
- [15] Chen, F.F., *Introduction to Plasma Physics*, Plenum Press, New York(1977).

- [16] Litvak, A.G., Permitin, G.V., Suvorov, E.V., and Frajman, A.A., "Electron-Cyclotron Heating of Plasma in Toroidal Systems," *Nucl. Fusion*, 17 (1977) 659.
- [17] Batchelor, D.B., "Status of the Theoretical Study of Microwave Heating in EBT," ORNL/TM-6320 (1978).
- [18] Fried, B.D., and Conte, S.D., *The Plasma Dispersion Function*, Academic Press, New York(1961).
- [19] Bernstein, I.B., "Geometric Optics in Space- and Time-Varying Plasmas," *Phys. Fluids*, 18 (1975) 320.
- [20] Maekawa, T., Tanaka, S., Terumichi, Y., and Hamada, Y., "Wave Trajectory and Electron-Cyclotron Heating in Toroidal Plasmas," *Phys. Rev. Lett.* 40 (1978) 1379.
- [21] Kulp, J.L., Jr., "Toroidal Effects in Lower Hybrid Heating of a Tokamak Plasma," Ph.D. Thesis, Dept. of Electrical Eng., M.I.T. (1978).
- [22] Bonoli, P.T., and Ott, E., "Toroidal and Scattering Effects on Lower-Hybrid Wave Propagation," *Phys. Fluids*, 25 (1982) 359.
- [23] McVey, B.D., "A Ray Tracing Analysis of Fast Wave Heating of Tokamaks," Ph.D. Thesis, Dept. of Electrical Eng., Univ. of Wisconsin-Madison (1978).
- [24] Batchelor, D.B., Goldfinger, R.C., and Weitzner, H., "Ray Tracing Near the Electron Cyclotron Frequency with Application to EBT," *IEEE Trans. on Plasma Science*, Vol. PS-8, p78, June 1980.
- [25] Boris, J., and Winsor, N., "Extrapolated Numerical Integration in Theory and Practice," PPPL, MATT-652 (1970).
- [26] Johnson, L.W., and Riess, R.D., *Numerical Analysis*, Addison-Wesley, Reading, MA(1977).
- [27] Beyer, W.H., ed., "CRC Standard Mathematical Tables," 26th ed., CRC Press, Boca Raton, Fla. (1981).
- [28] Callen, J.D., "Absolute and Convective Microinstabilities of a Magnetized Plasma," Ph.D. Thesis, Dept. of Nuclear Eng., MIT(1968).
- [29] Motojima, O., Private Discussion, at Kyoto Plasma Physics Laboratory on January 6, 1983.
- [30] Plasma Physics Laboratory, Kyoto University, *Annual Review*, PPLK-2, Plasma Physics Laboratory, Kyoto University, Gokasho, Uji, Kyoto, July, 1981.
- [31] Uo, K., Nakasuga, M., and Hakatani, K., *Heliotron Magnetic Surfaces*, PPLK-3, June 1982.
- [32] *World Survey of Major Activities in Controlled Fusion Research*, Special Supplement 1982 to *Nucl. Fusion* by IAEA, Vienna, 1982.
- [33] W VII A Team, "Ohmic Heating in the W VII A Stellarator," *Plasma Physics and Controlled Nuclear Fusion Research 1976*, IAEA-CN-35/D2, Vol. 2, p81, 1977.

- [34] W VII A Team, "Energy and Particle Confinement in the Ohmically Heated W VII-A Stellarator," Plasma Physics and Controlled Nuclear Fusion Research 1978, IAEA-CN-37/H-2, Vol. 2, p265, 1979.
- [35] W VII Team, "Stellarator Wendelstein W VII, Information presented at the 8th symposium on fusion technology, the Netherlands," IPP 2/224, June 1974.
- [36] Batchelor, D.B., and Goldfinger, R.C., "A Theoretical Study of Electron-Cyclotron Heating in Elmo Bumpy Torus," ORNL/TM-6992 (1979).
- [37] Ohkubo, K., Kawahata, K., Matsuoka, K., Noda, N., and Sakurai, K., "Pre-ionization and Heating of Stellarator Plasma at Electron Cyclotron Frequency in JIPPT-II," Nucl. Fusion, 21(1981)1320.
- [38] Atkinson, D.W., Bradley, J.E., Dellis, A.N., Johnson, P.C., Lees, D.J., et. al., "ECRH and Neutral-Injection Experiments in the Cleo Stellarator," Plasma Physics and Controlled Nuclear Fusion Research 1980, IAEA-CN-38/H-1-1, Vol. 1, p153, 1981.
- [39] Ohkubo, K., Kawahata, K., Noda, N., Ogawa, I., Kako, E., et. al., "Electron Cyclotron Heating of Stellarator Plasma with Ordinary and Extraordinary Modes in JIPPT-II," Nucl. Fusion, 22(1982)1085.
- [40] Uo, K., Iiyoshi, A., Obiki, T., Motojima, O., Morimoto, S., et. al., Results presented at the Plasma Physics and Controlled Nuclear Fusion Research Conference, Baltimore, U.S.A., Paper IAEA-CN-41/ L-3(1982).